THREE –DIMENSIONAL EARTHQUAKE RESPONSE OF SLOPES

CANDIDATO: RELATORE:

Gianmarco Ferrari   Chiar.mo Prof. **Guido Gottardi**

CORRELATORE:

Ing. **Amir M. Kaynia**

SUMMARY

II

IV

Abstract

L'obiettivo della presente ricerca è volto a determinare quale possa essere la vera importanza di considerare la tridimensionalità nella risposta dinamica dei pendii e monitorare gli effetti delle condizioni al contorno utilizzate.

La tesi è stata svolta utilizzando il software FLAC^{3D}, un programma tridimensionale di analisi alle differenze finite, non lineare, per la computazione numerica ingegneristica e geomeccanica. E' stato scelto questo software perché esso consente di utilizzare le condizioni al contorno: *"free-field boundary condition"*, strumento molto utile e ben funzionante nel campo delle analisi dinamiche. Nell'analisi numerica della risposta sismica, le condizioni al contorno del modello devono tener conto del moto di *"free-field"* che esisterebbe in assenza di strutture nel terreno. In alcuni casi può essere sufficiente utilizzare condizioni al contorno elementari; queste però devono essere poste a distanza sufficiente per minimizzare la riflessione delle onde sismiche in modo da poter comunque raggiungere le condizioni di *"free-field"*.

Tuttavia, quando lo smorzamento del materiale è basso, la distanza a cui si dovrebbero posizionare le condizioni al contorno aumenta di molto e questo porterebbe ad un modello con dimensioni non pratiche da gestire.

Per questo motivo risulta opportuno utilizzare una procedura alternativa, sviluppata anche per FLAC^{3D}, che imponga il moto di *"free-field"* in modo tale che i margini del modello possano mantenere le loro proprietà non-riflettenti. Questa proprietà è proprio quella che utilizzano le *"free-field buondary condition"*.

Nella prima parte della tesi, l'attenzione si è pertanto focalizzata sull'uso di queste condizioni al contorno.

Per studiare le potenzialità di questo strumento è stato eseguito un confronto fra simulazioni dinamiche con FLAC^{3D} ed alcuni risultati analitici. Inoltre sono state condotte altre analisi per stimare l'influenza sul modello di queste condizioni al contorno.

Dopodiché, per studiare il problema principale dell'effetto della tridimensionalità sulla risposta dinamica dei pendii, si è pensato di adottare il modello costitutivo "SANICLAY". "SANICLAY" è un modello costitutivo basato sul modello "Cam clay modificato", con l'aggiunta di due meccanismi che tengono conto dell'anisotropia e del softening del materiale.

Prima di applicare il modello "SANICLAY" ad una complessa geometria tridimensionale sono state condotte alcune simulazioni numeriche per testare le sue potenzialità e la sua stabilità. Dopo una serie di analisi di sensitività su alcuni parametri si è visto che il modello costitutivo "SANICLAY", implementato per FLAC^{3D} pochi anni fa, non risulta sufficientemente stabile per tutte le condizioni; per questo si è deciso di continuare il lavoro adottando il modello costitutivo "Mohr-Coulomb".

L'ultima parte della tesi è volta ad analizzare l'effetto della tridimensionalità nella risposta dinamica dei pendi. A tal fine è stato creato un modello tridimensionale avente due differenti pendii giacenti su due delle tre direzioni principali del sistema di riferimento. Su questa geometria è stata eseguita un'estesa analisi di sensibilità riguardante alcuni parametri, come la frequenza dell'onda sismica, l'accelerazione di picco e gli angoli dei due pendii.

Osservando i risultati dell'analisi parametrica, sopratutto focalizzandosi sugli spostamenti, si è scoperto che il modello costruito lavora bene, perchè, come previsto, aumentando il valore di picco dell'accelerazione dell'onda di input oppure aumentando la pendenza dei pendii si ottengono spostamenti maggiori. Considerando l'analisi di sensitività effettuata sulle frequenze dell'onda di input gli spostamenti maggiori si sono verificati per una frequenza di 2 Hz. Questo può essere spiegato dal fatto che il valore della frequenza è prossimo alla frequenza propria del modello di terreno.

Alla fine, i risultati di alcuni casi significativi di queste simulazioni numeriche sono stati confrontati con i risultati ottenuti attraverso l'utilizzo di modelli bidimensionale per evidenziare e quantificare gli effetti della tridimensionalità. Dai risultati delle simulazioni numeriche è stato possibile concludere che il modello tridimensionale fornisce i valori maggiori in termini di spostamenti e deformazioni. La presenza del pendio secondario produce una condizione maggiormente critica rispetto ad un semplice

modello bidimensionale avente le stesse dimensioni. Il modello bidimensionale ovviamente non riesce a catturare queste caratteristiche. Queste osservazioni e questi risultati, indicano che gli effetti della tridimensionalità sono molto importanti. In questi casi, una semplice analisi bidimensionale potrebbe sottostimare gli effetti dellùinput dinamico.

I risultati di questo studio possono essere usati per avere un'idea del grado di non cautelatività dei risultati bidimensionali. Inoltre, sviluppi per il futuro potrebbero riguardare il modello "SANICLAY" e lo sviluppo di un nuovo script per renderlo più facilmente applicabile a tutti i casi necessari, e per renderlo stabile. Riguardo al problema della tridimensionalità invece, sarebbe interessante vedere la risposta sismica dei pendi adottando diversi input sismici, cambiando la direzione dell'onda sismica o utilizzando un accelerogramma realistico.

Abstract

Introduction

The main goal of this work is to study the importance of considering the three-dimensionality in the dynamic response of slopes and effect of boundary conditions in the analyses.

The research is done by using of the software FLAC^{3D}, a three-dimensional explicit non linear finite-difference program for engineering mechanics computation. This software it has been chosen because of the possibility to adopt the *free-field boundary condition*, which is a very useful and good powerful and effective tool for dynamic analysis of earthquake response.

Indeed in the numerical analysis of the seismic response, the boundary conditions at the sides of the model must account for the free-field motion that would exist in the absence of the structure. In some cases, elementary lateral boundaries, may be sufficient but should be placed at sufficient distances to minimize wave reflections and achieve free-field conditions. When the material damping is low, the required distance may lead to an impractical model, so an alternative procedure, developed also for FLAC^{3D}, is to "enforce" the free-field motion in such a way that boundaries retain their non-reflecting proprieties.

In the first part of the thesis, the attention has been focus on how to use this *free-field boundary condition* and its potentiality. To study these issues a comparison between analytical results and some numerical simulations is done in this way is possible to check the influence of these boundary conditions.

Next, the idea was to use SANICLAY constitutive model to study the main problem of the three dimensionality. SANICLAY is a constitutive model based on the well-known isotropic modified Cam Clay model with two additional mechanism to account for anisotropy and destructuration. Before applying this model to a three-dimensional geometry some simulations are made to test its potential and its stability. But as it will be describe in *Chapter 4*, this model, implemented in FLAC^{3D} few years ago, is not

quite stable for all conditions; so it was decided to continue the work adopting the Mohr Coulomb model.

The last part consisted to analyze the effect of the three dimensionality in the dynamic response of slopes. A three-dimensional geometry is created with two different slopes: one in *x*-direction and the other in the *y*-direction. On this geometry it is performed an extensive sensitivity analysis on parameters like: earthquake frequency, peak acceleration, and the angles of the two slopes. At the end the results of some significant cases of the three-dimensional simulations are compared with the results obtained with the corresponding two-dimensional model, to quantify the effect of the three-dimensionality.

Chapter 1 – Theory and Background

1.1 Background

Earthquake engineering deals with the effects of earthquake on people and their environment and with methods of reducing those effects. It is a very young discipline, many of its most important developments having occurred in the past 30 to 40 years. Earthquake engineering is a very board field, drawing on aspects of geology, seismology, geotechnical engineering, structural engineering, risk analysis, and other technical fields. Its practice also requires consideration of social, economic, and political factors. Most earthquake engineers have entered the field from structural engineering or geotechnical engineering backgrounds, a fact that is reflected in the practice of earthquake engineering.

The study of earthquakes dates back many centuries. Written records of earthquakes in China date as far back as 3000 years. Japanese records and records from eastern Mediterranean region go back nearly 1600 years. In the United States the historical record of earthquake is much shorter, about 350 years. On the seismically active west coast of the United States, earthquake records go back only about 200 years. Compared with the millions of years over which earthquakes have been occurring, humankind's experience with earthquakes is very brief.

Today, hundreds of millions of people throughout the world live with a significant risk to their lives and property from earthquakes. Billions of dollars of public infrastructure are continuously at risk of earthquake damage. The health of many local, regional, and even national economies are also at risk from earthquakes. Earthquakes are a global phenomenon and global problem.

Earthquakes have occurred for millions of years and will continue in the future as they have in the past. It is impossible to prevent earthquakes from occurring, but it is possible to mitigate the effects of strong earthquake shaking: to reduce loss of life, injuries, and damage. *(Kramer, 1996).*

1.1.1 Seismic Hazards

A number of naturally occurring events, such as earthquakes, hurricanes, tornados, and floods, are capable of causing death, injuries, and property damage. These natural hazards cause tremendous damage around the world each year. Hazard associated with earthquakes are commonly referred to as seismic hazards. The practice of earthquake engineering involves the identification and mitigation of seismic hazards. The most important seismic hazards are described in the following sections. *(Kramer, 1996).*

1.1.1.1   Ground Shaking

When an earthquake occurs, seismic waves radiate away from the source and travel rapidly through the earth's crust. When these waves reach the ground surface, they produce shaking that may last from seconds to minutes. The strength and duration of shaking at a particular site depends on the size and location of the earthquake and on the characteristics of the site. At site near the source of a large earthquake, ground shaking can cause tremendous damage. In fact, ground shaking can be considered to be the most important of all seismic hazards because all the other hazards are caused by ground shaking. Where ground shaking levels are low, these other seismic hazards may be low or nonexistent. Strong ground shaking, however, can produce extensive damage from a variety of seismic hazards.

Although seismic waves travel through rock over the overwhelming majority of their trip from the source of an earthquake to the ground surface, the final portion of that trip is often through soil, and the characteristics of the soil can greatly influence the nature of shaking at the ground surface. Soil deposit tend to act as "filters" to seismic waves by attenuating motion at certain frequencies and amplifying it at others. Since soil conditions often vary dramatically over short distances, levels of ground shaking can vary significantly within a small area. One of the most important aspects of geotechnical earthquake engineering practice involves evaluation of the effects of local soil conditions on strong ground motion. *(Kramer, 1996).*

1.1.1.2   Structural Hazards

Without doubt the most dramatic and memorable earthquake damage are those of structural collapse. Structural damage is the leading cause of death and economic loss

in many earthquakes. However, structures need not collapse to cause death and damage. Falling objects such as brick facings and parapets on the outside of a structure or heavy pictures and shelves within a structure have caused casualties in many earthquakes. Inferior facilities such as piping, lighting, and storage system can also be damaged during earthquakes. Over the years, considerable advances have been made in earthquake-resistant design of structures, and seismic design requirements in building codes have steadily improved. As earthquake-resistant design has moved from an emphasis on structural strength to emphasis on both strength and ductility, the need for accurate predictions of ground motions has increased. *(Kramer, 1996).*

1.1.1.3   Liquefaction

Some of the most spectacular examples of earthquake damage have occurred when soil deposit have lost their strength and appeared to flow as fluids. In this phenomenon, termed liquefaction, the strength of the soil is reduced, often drastically, to the point where it is unable to support structures or remain stable. Because it only occurs in saturated soil, liquefaction is most commonly observed near rivers, bays, and other bodies of water. The term liquefaction actually encompasses several related phenomena. Flow failures, for examples, can occur when the strength of the soil drops below the level needed to maintain stability under static conditions. Flow failures are therefore driven by static gravitational forces and can produce very large movements.

Liquefaction is a complicated phenomenon, but research has progressed to the point where an integrated framework of understanding can be developed. *(Kramer, 1996).*

1.1.1.4   Landslide

Strong earthquakes often cause landslide. Although the majority of such landslides are small, earthquakes have also caused very large slides. In a number of unfortunate cases, earthquake-induced landslides have buried entire towns and villages. More commonly, earthquake-induced landslides cause damage by destroying buildings, or disrupting bridges and other constructed facilities. Many earthquake-induced landslides result from liquefaction phenomena, but many others simply represent the failures of slopes that were marginally stable under static conditions. *(Kramer, 1996).*

1.2   Seismic slope stability

Landslides occur on a regular basis throughout the world as part of the ongoing evolution of landscape. Many landslides occur in natural slopes, but slides also occur in man-made slopes from time to time. At any point in time, then, slopes exist in states ranging from very stable marginally stable. When an earthquake occurs, the effects of earthquake-induced ground shaking is often sufficient to cause failure of slopes that were marginally to moderately stable before the earthquake. The resulting damage can range from insignificant to catastrophic depending on the geometric and material characteristics of the slope.

Earthquake-induced landslides, which have been documented from as early as 1789 B.C. (Li, 1990), have caused tremendous amounts of damage throughout history. In many earthquakes, landslides have been responsible for as much or more damage than all others seismic hazards combined. Evaluation of seismic slope stability is one of the most important activities of the geotechnical earthquake engineer. *(Kramer, 1996).*

1.2.1 Types of earthquake-induced landslides

Many factors, including geologic and hydrologic conditions, topography, climate, weathering, and land use, influence the stability of slopes and the characteristics of landslides. A number of procedures for classification of landslides have been proposed; that of Varnes (1978) is perhaps most widely used in the United States. Similar principles and terminology can be used to classify earthquake-induced landslides on the basis of material type (soil or rock), character of movement (disrupted or coherent), and other attributes, such as velocity, depth, and water content. Earthquake-induced landslides can be divided into three main categories: disrupted slides and falls, coherent slides, and lateral spreads and flows.

Disrupted slides and falls include rock falls, rock slides, rock avalanches, soil falls, disrupted soil slides, and soil avalanches. The earth materials involved in such failures are shared, broken, and disturbed into a near random order. These types of failures, usually found in steep terrain, can produce extremely rapid movements and devastating damage; rock avalanches and rock falls have historically been among the leading causes of death from earthquake-induced landslides.

Coherent slides, such as rock and soil slumps, rock and soil block slides, and slow earth flows, generally consist of a few coherent blocks that translate or rotate on somewhat deeper failure surfaces in moderate steeply sloping terrain. Most coherent slides occur are lower velocities than disrupted slides and falls.

Lateral spreads and flows generally involve liquefiable soils, although sensitive clays can produce landslides with very similar characteristics. Due to the low residual strength of these materials, sliding can occur on remarkably flat slopes and produce very high velocities.

The different types of earthquake-induced landslides occur with different frequencies. Rock falls, disrupted soil slides, and rock slides appear to be the most common types of landslides observed in historical earthquakes. Subaqueous landslides, slow earth flows, rock block slides, and rock avalanches are least common, although the difficulty of observing subaqueous slides may contribute to their apparent rarity. *(Kramer, 1996).*

1.2.2 Earthquake-induced landslide activity

For preliminary stability evaluations, knowledge of the conditions under which earthquake-induced landslides have occurred in past earthquakes is useful. It is logical to expect that the extent of earthquake-induced landslide activity should increase with increasing earthquake magnitude and that there could be a minimum magnitude below which earthquake-induced landsliding would rarely occur. It is equally to expect that the extent of earthquake-induced landslide activity should decrease with increasing source-to-site distance and that there could be a distance beyond which landslides would not to be expected in earthquakes of a given size. *(Kramer, 1996).*

1.2.3 Seismic slope stability analysis

The database against which seismic slope stability analyses can be calibrated is much smaller. Analysis of the seismic stability of slopes is further complicated by the need to consider the effects of dynamic stresses induced by earthquake shaking, and the effects of those stresses on the strength and stress-strain behavior of the slope materials.

Seismic slope instabilities may be grouped into two categories on the basis of which of these effects is predominant in a given slope. In inertial instabilities, the shear strength

of the soil remains relatively constant, but slope deformations are produced by temporary exceedances of the strength by dynamic earthquake stresses. Weakening instabilities are those in which the earthquake serves to weaken the soil sufficiently that it cannot remain stable under earthquake-induced stresses. Flow liquefaction and cyclic mobility are the most common causes of weakening instability. A number of analytical techniques, based on both limit equilibrium and stress-deformation analyses, are available for both categories of seismic instability. *(Kramer, 1996).*

1.2.3.1 Analysis of inertial instability

Earthquake motions can induce significant horizontal and vertical dynamic stresses in slopes. These stresses produce dynamic normal and shear stresses along potential failure surfaces within a slope. When superimposed upon the previously existing static shear stresses, the dynamic shear stresses may exceed the available shear strength of soil and produce inertial instability of the slope. A number of techniques for the analysis of inertial instability have been proposed. These techniques differ primarily in the accuracy with which the earthquake motion and the dynamic response of the slope are represented. *(Kramer, 1996).*

1.2.3.2 Pseudostatic Analysis

Pseudostatic analysis, produces a factor of safety against seismic slope failure in much the same way that static limit equilibrium analyses produce factor of safety against static slope failure. All the others approach attempt to evaluate permanent slope displacements produced by earthquake shaking.

Beginning in the 1920s, the seismic stability of earth structures has been analyzed by a pseudostatic approach in which the effects of an earthquake are representes by constant horizontal and/or vertical accelerations. The first explicit application of the pseudostatic approach to the analysis of seismic slope stability has been attributed to Terzaghi (1950). In their most common form, pseudostatic analyses represent the effects of earthquake shaking by pseudostatic accelerations that produce inertial forces, F_h and F_v, which act through the centroid of failure mass (Figure 1.1).
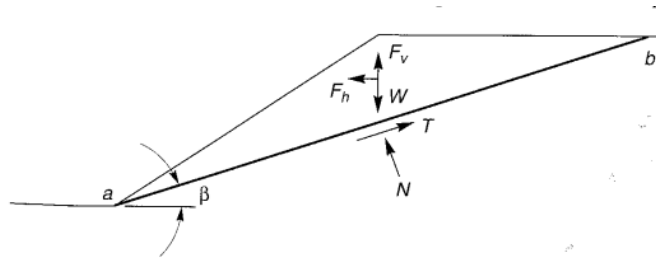
Figure 1.1 - *Forces acting on triangular wedge of soil above planar failure surface in pseudostatic slope stability analysis.*

The magnitudes of pseudostatic forces are:

$$F_h = \frac{a_h W}{g} = k_h W$$

$$F_v = \frac{a_v W}{g} = k_v W$$

where a_h and a_v are horizontal and vertical pseudostatic accelerations, k_h and k_v are dimensionless horizontal and vertical pseudostatic coefficients, and W is the weight of the failure mass. The magnitudes of the pseudostatic accelerations should be related to the severity of the anticipated ground motion; selection of pseudostatic accelerations for design is, as discussed in the next section, not simple matter. Resolving the forces on the potential failure mass in a direction parallel to the failure surface,

$$FS = \frac{resisting\ force}{driving\ force} = \frac{cl_{ab} + [(W - F_v)cos\beta]tan\varphi}{(W - F_v)sin\beta + F_h cos\beta}$$

where *c* and *φ* are the Mohr-Coulomb strength parameters that describe the shear strength on the failure plane and l_{ab} is the length of the failure plane. The horizontal pseudostatic force clearly decreases the factor of safety it reduces the resisting force (for φ > 0) and increases the driving force. The vertical pseudostatic force typically has less influence on the factor of safety - since it reduces both the driving force and resisting force - as a result, the effects of vertical accelerations are frequently neglected in pseudostatic analyses. The pseudostatic approach can be used to evaluate pseudostatic factors of safety for planar, circular, and noncircular failure surfaces. *(Kramer, 1996).*

1.2.3.3   Limitations of the Pseudostatic Approach

Representation of the complex, transient, dynamic effects of earthquake shaking by a single constant unidirectional pseudostatic acceleration is obviously quite crude. Even in its infancy, the limitations of the pseudostatic approach were clearly recognized. Terzaghi (1950) stated that "the concept it conveys of earthquake effects on slopes is very inaccurate, to say the least", and that a slope could be unstable even if the computed pseudostatic factor of safety was greater than 1. Detailed analyses of historical and recent earthquake-induced landslides have illustrated significant shortcomings of the pseudostatic approach. Experience has clearly shown, for example, that pseudostatic analyses can be unreliable for soils that build up large pore pressures or show more than about 15% degradation of strength due to earthquake shaking. A pseudostatic analyses produced factors of safety well above 1 for a number of dams that later failed during earthquakes. These cases illustrate the inability of the pseudostatic method to reliably evaluate the stability of slopes susceptible to weakening instability. Nevertheless, the pseudostatic approach can provide at least crude index of relative, if not absolute, stability. *(Kramer, 1996).*

1.2.3.4   Discussion

The pseudostatic approach has a number of attractive features. The analysis is relatively simple and straightforward; indeed, its similarity to the static limit equilibrium analysis routinely conducted by geotechnical engineers makes its computations easy to understand and perform. It produces a scalar index of stability that is analogous to that produced by static stability analyses. It must always be recognized, however, that the accuracy of the pseudostatic approach is governed by the accuracy with which the simple pseudostatic inertial forces represent the complex dynamic inertial forces that actually exist in earthquake. Difficulty in the assignment of appropriate pseudostatic coefficients and in interpretation of pseudostatic factors of safety, coupled with the development of more realistic methods of analysis, have reduced the use of the pseudostatic approach for seismic slope stability analyses. Methods based on evaluation of permanent slope deformation are being used increasingly for seismic slope stability analysis. *(Kramer, 1996).*

1.3   Review of 3D vs. 2D analyses

Justo and Saura, Byrne et al., Stark and Eid, Jeremic, among many others, have studied the importance of considering the 3D effects in the analysis of slopes. Duncan cites over 20 studies (since 1960s) concluding that in the factor-of-safety approach, with a few exceptions, two-dimensional analysis yields conservative results compared to three-dimensional analysis, i.e. $F_{2D} < F_{3D}$ provided that F_{2D} is calculated for the most critical 2D section.

Since $F_{2D} < F_{3D}$, Leshchinsky and Huang and Duncan and Stark emphasize that in order to obtain post-failure in situ shear strength of soil by back-analysis of slope failures, 3D analysis should be avoided so that shear strength (to be used in 2D analysis) is not overestimated.

Arellano and Stark present several curves showing the ratio of 3D to 2D factor of safety for different width/height ratios and slope angles, with translational failure mechanism. These curves show that for a 3H:1V slope, for example, the 3D factor of safety is about 40% larger than the 2D factor of safety if the width/height ratio is about 2. In this type of failure mechanism, which usually occurs in flatter slopes, the mobilized shear strength along back scarp and sides of the slides mass are significantly different from those along the base.

In deformation analysis approach, Lefebvre et al. found that 2D analysis can significantly overestimate movements of a dam in a V-shaped steep-wall valley because the effects of cross-valley arching are ignored in 2D analysis. Comparing the results of 2D and 3D analysis of the transverse section of the dam showed that if the valley wall slopes were 1:1 or steeper, plane strain results would be significantly inaccurate. 2D/3D ratios of principal stresses, maximum shear stress, and displacements were also presented. For example, average 2D/3D ratio of horizontal displacements for 1:1 wall was 2.68, whereas that for 6:1 wall was 1.05.

Some other studies, such as also compare the results of 3D and 2D finite element analyses for dams (simulating reservoir filling, water rise, etc.) and generally indicate that deformation in 3D models are significantly smaller than in 2D models, for

width/height ratios of about 2-3. From these studies, it is also possible to note that beyond a certain distance from the abutments, there is no significant variation in the predicted crest displacement. This distance is normally about 2.5-3 times the height. (*Azizian, A., Popescu, R., 2005*)

Prevost et al. performed 2D and 3D total stress, dynamic FE analysis of Santa Felicia earth dam using a non-linear multi-surface plasticity model and compared the measured and computed earthquake responses. Their analysis showed that the first 10 frequencies of the 3D model all fall within the first two frequencies of the 2D model, indicating that more intermediate modal configurations are generated, despite the fat that the dam is a relatively long dam and 3D effects should not be significant. The study demonstrates the importance of 3D effects being more pronounced for strong shaking, in terms od crest acceleration and permanent deformations. In case of strong shaking, the 3D horizontal crest acceleration response is significantly lower than the 2D one due to significant contributions from higher modes of vibration. The two-dimensional idealization is normally based on the following considerations:

1. Site material idealization: in most cases, it is assumed that soil layering is perpendicular to the plane of interest and a cross section represents all sections. If non-homogeneity or anisotropy of the slope material is important, then performing a 2D analysis is not appropriate. (*Azizian, A., Popescu, R., 2005*)
2. Site geometry idealization: in numerical or analytical approaches toward many geotechnical problems, three main geometric idealizations are used to simplify and speed-up the analysis significantly: plane strain, plane stress, and axi-symmetry. Almost all two-dimensional slope stability analyses use plane strain assumption, in which the value of the strain component perpendicular to the plane of interest is zero. Analysis time as well as necessary computational resources will decrease significantly, especially in a seismic step-by-step time-domain analysis. However, the plane strain assumption is valid if one dimension is very large in comparison with the other two. It also requires all of the following: no curvature or corners exist in geometry of slope; the slope deformation is not constrained significantly by a near lateral boundary (such as a dam in a narrow rock-walled valley); no curvature exists in the shape of failure

surface in the direction perpendicular to the plane of interest. (*Azizian, A., Popescu, R., 2005*)

3. Loading idealization: design recommendations usually suggest that from three components of earthquake acceleration, only the larger horizontal acceleration would suffice for analysis purpose. Vertical and smaller horizontal components of acceleration are then ignored. In the analysis of slopes, the horizontal acceleration is usually applied to the cross-section of the slope in its plane, that is, no instability due to transverse (out-of-plane) excitation is taken into account. (*Azizian, A., Popescu, R., 2005*)

1.4   Constitutive model

In this part will be presented the constitutive model used during the work. The models is the SANICLAY model, based on the more known Modified Cam-Clay model, so first of all a short presentation of the Modified Cam-Clay model is given.

1.4.1 Modified Cam-Clay model

The modified Cam-Clay model is an incremental hardening/softening elastoplastic model. Its features include a particular form of nonlinear elasticity and a hardening/softening behaviour governed by volumetric plastic strain. The failure envelopes are self-similar in shape and correspond to ellipsoids of rotation about the mean stress axis in the principal stress space. Then shear flow rule is associated; no resistance to tensile mean stress is offered in this model.

1.4.1.2   Incremental Elastic Law

The generalized stress components involved in the model definition are the mean effective pressure, p, and deviatoric stress, q, defined as

$$p = -\frac{1}{3}\sigma_{ii}$$

$$q = \sqrt{3J_2}$$

where the Einstein summation convention applies and J_2 is the second invariant of the effective deviatoric-stress tensor $[s]$. The incremental strain variables associated with p

and q are the volumetric strain increment $\Delta\epsilon_p$ and shear strain increment $\Delta\epsilon_q$, and we have

$$\Delta\epsilon_p = -\Delta\epsilon_{ii}$$

$$\Delta\epsilon_q = \frac{2}{3}\sqrt{3\Delta J_2'}$$

where $\Delta J_2'$ stands for the second invariant of the incremental deviatoric-strain tensor $\Delta[e]$. In the FLAC^{3D} plastic flow formulation, the assumption is made that both plastic and elastic principal strain-increment vectors are coaxial with the current principal stress vector. The generalized strain increments are then decomposed into elastic and plastic parts so that

$$\Delta\epsilon_p = \Delta\epsilon_p^e + \Delta\epsilon_p^p$$

$$\Delta\epsilon_q = \Delta\epsilon_q^e + \Delta\epsilon_q^p$$

The evolution parameter is the specific volume, v, defined as

$$v = \frac{V}{V_s}$$

where V_s, is the volume of solid particles, assumed incompressible, contained in a volume, V, of soil. The incremental relation between volumetric strain, ϵ_p, and specific volume has the form

$$\Delta\epsilon_p = -\frac{\Delta v}{v}$$

And the specific volume, v^N, for the step may be calculated as

$$v^N = v(1 - \Delta\epsilon_p)$$

The incremental expression of Hooke's law in terms of generalized stress and strain is as follows:

$$\Delta p = K\Delta\epsilon_p^e$$

$$\Delta q = 3G\Delta\epsilon_q^e$$

where $\Delta q = \sqrt{3\Delta J_2}$, and ΔJ_2 stands for the second invariant of the incremental deviatoric-stress tensor. In the Cam-clay model, the tangential bulk modulus, K, in the volumetric relation $\Delta p = K\Delta\epsilon_p^e$ is update to reflect a nonlinear law derived experimentally from isotropic compression tests. The results of a typical isotropic compression tests are presented in the semi-logarithmic plot in Figure 1.2.
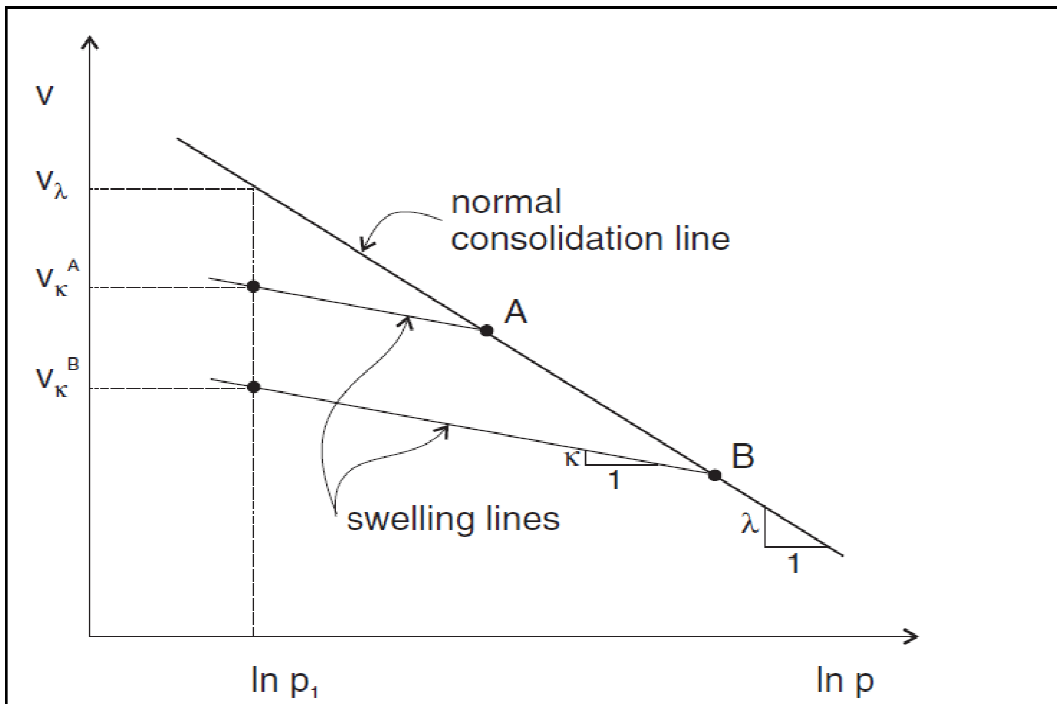
Figure 1.2 - *Normal consolidation line and unloading-reloading (swelling) line for an isotropic compression test. (FLAC^{3D} Manual).*

As the normal consolidation pressure, p, increases, the specific volume, v, of the material decreases. The point representing the state of the material moves along the normal consolidation line defined by the equation

$$v = v_\lambda - \lambda \ln\frac{p}{p_1}$$

where λ and v_λ are two material parameters, and p_1 is a reference pressure (v_λ is the value of the specific volume at the reference pressure). λ is used by Wood (1990) to define the slope of the normal consolidation line. It should not be confused with the

plastic (volumetric) multiplier used in the plasticity flow rule. An unloading-reloading excursion, from point A or B on the figure, will move the point along an elastic swelling line of slope κ, back to the normal consolidation line where the path will resume. The equation of the swelling lines has the form

$$v = v_k - \kappa \ln \frac{p}{p_1}$$

where κ is a material constant, and the value of v_κ for a particular line depends on the location of the point on the normal consolidation line from which unloading was performed.

The recoverable change in specific volume, Δv_e, may be expressed in incremental form after differentiation of the equation

$$\Delta v_e = -\kappa \frac{\Delta p}{p}$$

After division of both members by v, and using equation: $\Delta \epsilon_p = -\frac{\Delta v}{v}$, we may write

$$\Delta p = \frac{vp}{\kappa} \Delta \epsilon_p^e$$

In the Cam-clay model, it is assumed that any change in mean pressure is accompanied by elastic change in volume according to the above expression. Comparison with the equation: $\Delta p = K \Delta \epsilon_p^e$, hence, suggests the following expression for the tangent bulk modulus of the Cam-clay material:

$$K = \frac{vp}{\kappa}$$

Under more general loading conditions, the state of a particular point in the medium might be represented by a point, such as A, located below the normal consolidation line in the (v, lnp) plane as shown in Figure 1.3. By virtue of the law adopted in: $v = v_\kappa - k \ln \frac{p}{p_1}$, an elastic path from that point proceeds along the swelling line through A.
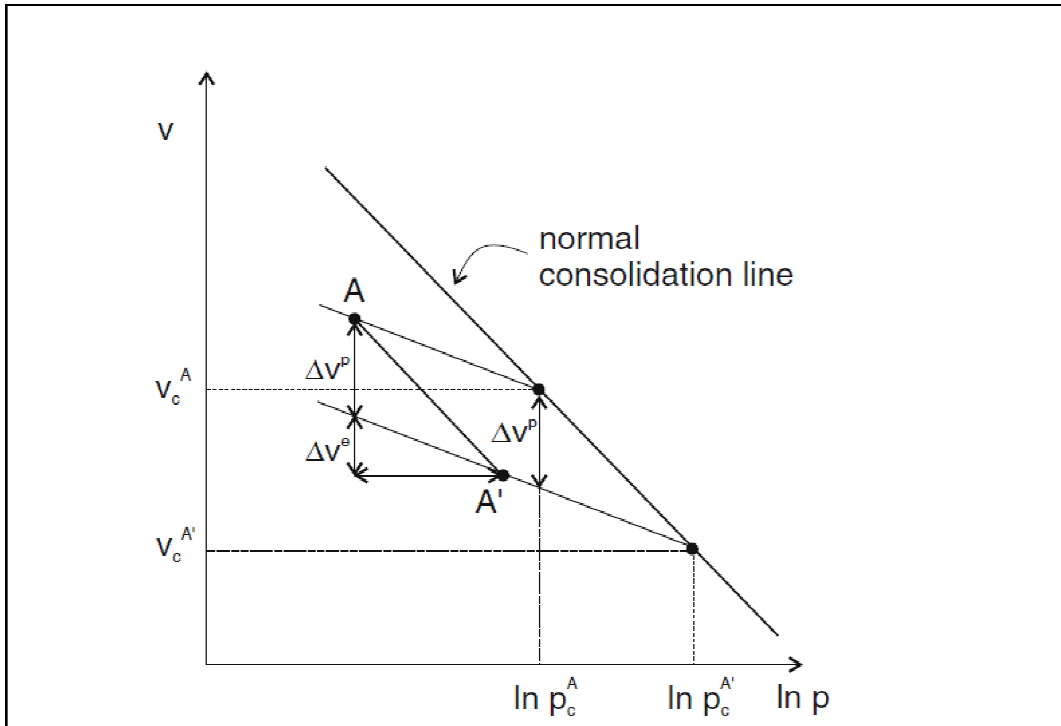
Figure 1.3 - *Plastic volume change corresponding to an incremental consolidation*
pressure change (FLAC^{3D} Manual).

The specific volume and mean pressure at the intersection of swelling line and normal consolidation line are referred to as (normal) consolidation (specific) volume and (normal) consolidation pressure (v_c^A and p_c^A, in the case of point A). Consider an incremental change in stress bringing the point from state A to state A'. At A' there corresponds a consolidation volume, $v_c^{A'}$, and consolidation pressure, $p_c^{A'}$. The increment of plastic volume change, Δv^p, is measured on the figure by the vertical distance between lines (associated with points A and A') and we may write, using incremental notation,

$$\Delta v^p = -(\lambda - \kappa)\frac{\Delta p_c}{p_c}$$

After division of the left and right member by v, we obtain, comparing with equation: $\Delta \epsilon_p = -\frac{\Delta v}{v}$:

$$\Delta \epsilon_p^p = \frac{\lambda - \kappa}{v}\frac{\Delta p_c}{p_c}$$

Hence, whereas elastic volume changes take place whenever the mean pressure changes, plastic volume changes occur only when the consolidation pressure changes.

1.4.1.2   Yield and potential functions

The yield function corresponding to a particular value p_c of the consolidation pressure has the form

$$f(q, p) = q^2 + M^2 p(p - p_c)$$

where M is a material constant. The yield condition $f = 0$ is represented by an ellipse with horizontal axis, p_c, and vertical axis, Mp_c, in the (q, p)-plane, as shown in Figure 1.4.
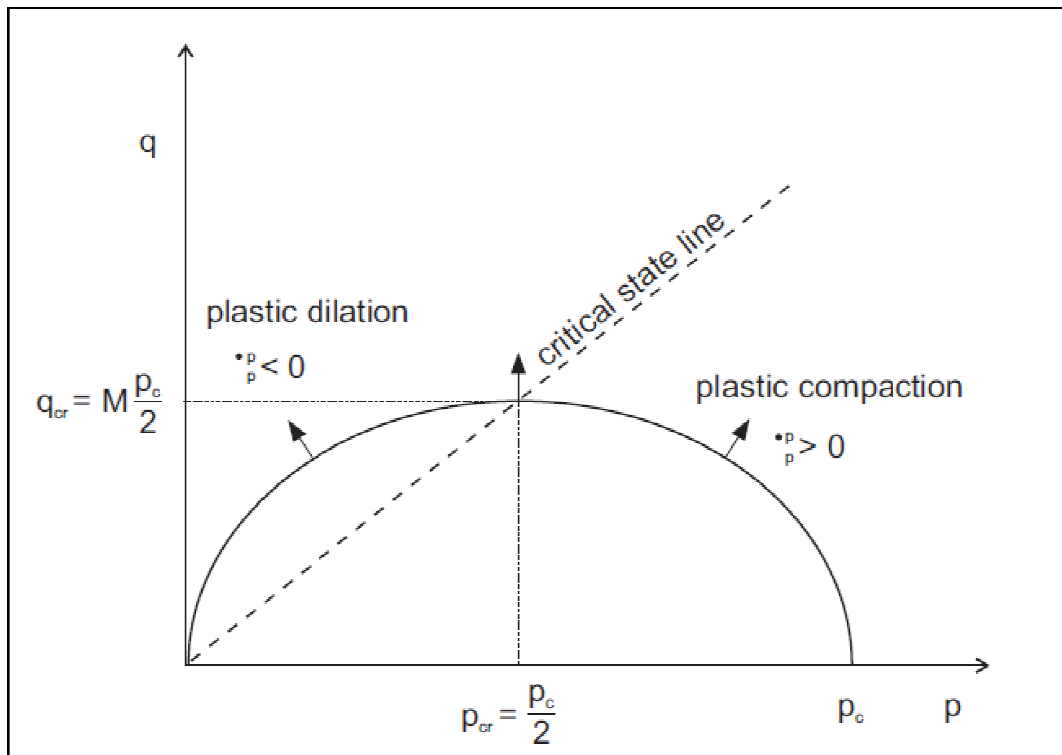
***Figure 1.4** - Cam-clay failure criterion in FLAC³ᴰ (FLAC³ᴰ Manual).*

Note that the ellipse passes through the origin; hence, the material in this model is not able to support an all-around tensile stress. The failure criterion is represented in the principal stress space by an ellipsoid of rotation about the mean stress axis (any section through the yield surface at constant mean effective stress, p, is a circle). The potential function, g, corresponds to an associated flow rule and we have

$$g = q^2 + M^2 p(p - p_c)$$

1.4.1.3   Hardening/Softening rule

The size of the yield curve is dependent on that value of the consolidation pressure, p_c. This pressure is a function of the plastic volume change and varies with the specific volume. The consolidation pressure is update for the step, using the formula

$$p_c^N = p_c \left(1 + \Delta\epsilon_p^p \frac{v}{\lambda - \kappa}\right)$$

where $\Delta\epsilon_p^p$ is the plastic volumetric strain increment for the step, v is the current specific volume and λ and κ are material parameters.

1.4.2 SANICLAY model

SANICLAY is a simple anisotropic clay plasticity model that builds on a modification of an earlier model with an associated flow rule, in order to include simulations of softening response under undrained compression following K_0 consolidation. Non-associativity is introduced by adopting a yield surface. Besides, the isotropic hardening of the yield surface evolves according to a combined distortional and rotational hardening rule, simulating the evolving anisotropy. The SANICLAY is shown to provide successful simulation of both undrained and drained rate-independent behaviour of normally consolidated sensitive clays, and to a satisfactory degree of accuracy of overconsolidated clays. The model requires merely three constants more than those of the modified Cam-clay model, all of which are easily calibrated from well-established laboratory tests.

Dafalias proposed what can be thought to be the simplest possible energetic extension of the modified Cam clay (MCC) model from isotropic to anisotropic response, introducing in the rate of plastic work expression a contribution coupling the volumetric and deviatoric plastic strain rates. The resulting plastic potential surface in the triaxial p-q space, which for associative plasticity serves also as yield surface, is rotated and distorted ellipse. The amount of rotation and distortion is controlled by an evolving variable α, which is a scalar-valued in triaxial and tensor-valued in multiaxial stress space. The proposition by Dafalias, about this new hardening model, has these two

distinct characteristics. The yield surface has been derived from an energetic expression for the rate of plastic work. Second, the so derived yield surface maintains the peak q stress on it always at the critical stress-ratio M for any degree of rotation and induced anisotropy. The M acquires different values M_c and M_e in compression and extension. The shape of the surface, in conjunction with the adopted rotational hardening law, induces a critical state line (CSL) in the void ratio-mean effective stress space, whose location depends on the degree of anisotropy, and in general is different in triaxial compression and extension.

A model for soft clays should be able to also simulate the softening response than is often measured during undrained compression shearing following anisotropic consolidation at $OCR = 1$. From a constitutive point of view, this undrained softening response can be addressed by special forms of the rotational hardening law or by a non-associative flow rule. Focusing on the latter approach for reason of simplicity and stability of the response, Dafalias et al. introduced a yield surface of the same general form as the original plastic potential, but with a different rotational variable α, and a different peak stress ratio than M.

1.4.2.1   Mathematical Formulation of the model

The constitutive model is constructed by extending the modified Cam-clay model, which has a simple and elegant formulation with clear physical interpretation. The present formulation takes advantage of the simple framework of MCC, and with perhaps the simplest possible approach, adds the very important features of anisotropy and destructuration. Each one of these important constitutive features can be deactivated, if so desired by the user, simply by selecting appropriate values for certain model constants. In this way, the developed model can be simplified back to the modified Cam-clay model.

In this section, σ and ε are generic symbols for the stress and strain tensor and their components. All stress components are considered effective, and as usual in geomechanics, both stress and strain quantities are assumed positive in compression. The stress tensor σ can be analyzed in a hydrostatic $p = (tr\sigma)/3$ and a deviatoric components $\boldsymbol{s} = \sigma - p\boldsymbol{I}$, where tr denotes the trace and $\boldsymbol{I}$ is the identity tensor.

Similarly, the strain tensor ε can be decomposed in a volumetric $\varepsilon_v = tr\varepsilon$ and a deviatoric component $\boldsymbol{e} = \varepsilon - \varepsilon_v(\boldsymbol{I}/3)$. Within the range of small deformations and rotations, the kinematical assumption of the additive decomposition of total strain rate into elastic and plastic part is assumed, i.e., $\dot{\varepsilon} = \dot{\varepsilon^e} + \dot{\varepsilon^p}$. The elastic strain rate is given by

$$\varepsilon^e = \frac{\dot{\varepsilon_v^e}}{3}\boldsymbol{I} + \dot{\boldsymbol{e}^e} = \frac{\dot{p}}{3K}\boldsymbol{I} + \frac{\dot{\boldsymbol{s}}}{2G}$$

where the elastic bulk and shear moduli K and G are obtained from

$$K = \frac{p(1+e)}{k} \qquad\qquad G = \frac{3K(1-2\nu)}{2(1+\nu)}$$

where e is the current void ratio; and k and ν are the slope of rebound line in e-lnp and the Poisson's ratio, respectively.

For simplicity, an associated flow rule has been employed, giving a single expression $f = 0$ for the yield surface and the plastic potential. The plastic strain rate is given by

$$\dot{\varepsilon^p} = \langle L \rangle \frac{\partial f}{\partial \sigma}$$

where L is the loading index. The expression provided for the plastic potential, which is the same for the yield surface here, owing to application of associative plasticity, is obtained from an assumption for the plastic work dissipation given in Dafalias (1986), in the form of

$$f = \frac{3}{2}(\boldsymbol{s} - p\alpha) : (\boldsymbol{s} - p\alpha) - \left(M^2 - \frac{3}{2}\alpha : \alpha\right)p(p_0 - p) = 0$$

where the symbol : implies the inner product of two tensor (the trace of their product); the anisotropic variable α is a dimensionless deviatoric tensor and p_0 is a scalar variable. The scalar M is the critical stress ratio and can be interpolated between its values M_c in compression and $M_e = mM_c$ in extension as a function of a Lode angle θ and by means of the proposition of Argyris et al. (1974) as

$$M = \Theta(\theta, m)M_c = \frac{2m}{(1+m)-(1-m)\cos 3\theta}M_c$$

$$\cos 3\theta = \sqrt{6}tr\mathbf{n}^3; \qquad \mathbf{n} = \frac{\mathbf{r}-\alpha}{[(\mathbf{r}-\alpha):(\mathbf{r}-\alpha)]^{1/2}}$$

with $\mathbf{r} = \mathbf{s}/p$ the deviatoric stress ratio tensor.
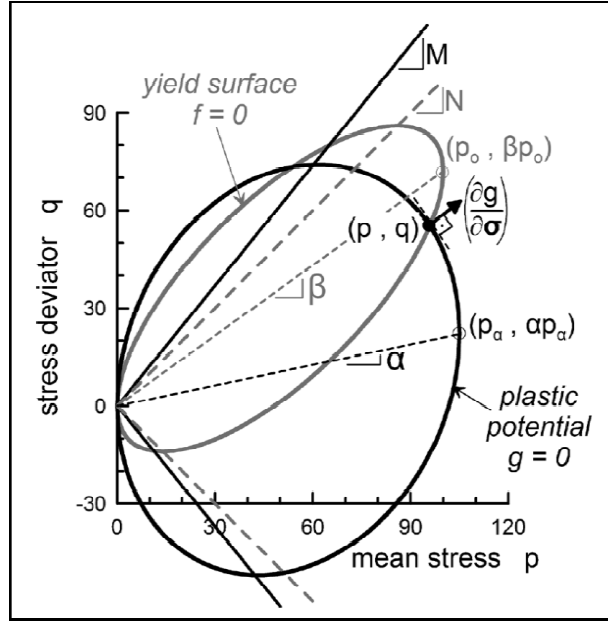
Figure 1.5 - *Model surfaces in triaxial stress space.*

An illustration of the model is shown in Figure 1.5, which is in the triaxial p-q space. The isotropic hardening of the internal variable p_0 is based on the classical evolution law of critical state soil mechanics in conjunction with the specialization of equation $\dot{\varepsilon}^p = \langle L \rangle \frac{\partial f}{\partial \sigma}$ for the volumetric plastic strain rate and yields

$$\dot{p}_0 = \langle L \rangle \left(\frac{1+e}{\lambda-k}\right) p_0 tr\left(\frac{\partial f}{\partial \sigma}\right) = \langle L \rangle \bar{p}_0 \qquad (1)$$

The kinematic hardening rule for the internal variable α is based on the distance of back stress ratio α from its bounding *image* α^b, which in turn is defined by an attractor term $\mathbf{r}/x$ as (Dafalias et al. 2006; Taiebat et al. 2010)

$$\dot{\alpha} = \langle L \rangle \left(\frac{1+e}{\lambda-k}\right) C \left(\frac{p}{p_0}\right)^2 \left|tr\left(\frac{\partial f}{\partial \sigma}\right)\right| \left[\frac{3}{2}(\mathbf{r}-x\alpha):(\mathbf{r}-x\alpha)\right]^{1/2} \times (\alpha^b - \alpha) = \langle L \rangle \bar{\alpha} \qquad (2)$$

$$\alpha^b = \sqrt{\frac{2}{3}} M_e \mathbf{n}_x; \qquad\qquad \mathbf{n}_x = \frac{\mathbf{r} - x\alpha}{[(\mathbf{r} - x\alpha):(\mathbf{r} - x\alpha)]^{1/2}}$$

where C and x are two model constants and the expression for $\bar{\alpha}$ is evident from the last two members of the equation (2). The constant C controls the evolution of anisotropy in the model, and the constant x in the attractor term provides a flexibility to the model for proper estimation of the value of K_0. To include an isotropic destructuration mechanism in the model the internal variable p_0 is set equal to $S_i p_{0d}$, where $S_i \geq 1$ is the isotropic structuration factor and p_{0d} is the destructured value of p_0 (or the value of p_0 at $S_i = 1$). With this new definition of p_0, equation (1) should now be replaced by the following equation, where $p_0 = S_i p_{0d}$ yields

$$\dot{p}_0 = S_i \dot{p}_{0d} + \dot{S}_i p_{0d} = \langle L \rangle (S_i \bar{p}_{0d} + \bar{S}_i p_{0d}) = \langle L \rangle \bar{p}_0 \qquad (3)$$

where the analytical expression of $\bar{p}_0$ is evident for the last two members of the equation (3) Here $\bar{p}_{0d}$ and $\bar{S}_i$ are obtained from

$$\dot{p}_{0d} = \langle L \rangle \left(\frac{1+e}{\lambda-k}\right) p_{0d} \, tr\left(\frac{\partial f}{\partial \sigma}\right) = \langle L \rangle \bar{p}_{0d} \qquad (4\ a)$$

$$\dot{S}_i = -\langle L \rangle k_i \left(\frac{1+e}{\lambda-k}\right)(S_i - 1)\bar{\varepsilon}_d^p = \langle L \rangle \bar{S}_i \qquad (4\ b)$$

with $\bar{p}_{0d}$ and $\bar{S}_i$ following from the last two members of equation (4 a) and (4 b), respectively, and where κ_i is a material constant. The degradation of S_i has been taken into account means of $\dot{\varepsilon}_d^p = \langle L \rangle \bar{\varepsilon}_d^p$, which is the rate of an auxiliary internal variable called the destructuration plastic strain rate and defined as

$$\dot{\varepsilon}_d^p = \langle L \rangle \bar{\varepsilon}_d^p = \sqrt{(1-A)\dot{\varepsilon}_d^{p2} + A\left(\frac{2}{3}\dot{\mathbf{e}}^p : \dot{\mathbf{e}}^p\right)} \qquad (5)$$

The parameter A is a material constant distributing the effect of volumetric and deviatoric plastic strain rates to the value of $\dot{\varepsilon}_d^p$. The foregoing destructuration mechanism described by equations (3)-(5) is a classical approach of isotropic destructuration. In Taiebat et al. (2010), in addition to the present isotropic destructuration mechanism that is in effect an isotropic-softening constitutive feature, an additional frictional destructuration mechanism was introduced that addressed the

possible collapse of the critical state stress ratio M in the foregoing destructuration plastic strain rate of equation (5). This mechanism is omitted in the present work for simplicity and because the isotropic destructuration is by far the more important of the two. In other words, many of the aspects of destructuration response in clays can be sufficiently addressed only by the isotropic destructuration mechanism for many practical purposes.

Moreover, in Taiebat et al. (2010), the full destructuration model also had additional features, such as a plastic potential surface different than the yield surface with a different rotational variable, and simplified version were studied in regard to simulations of data and the relative effect of the two aforementioned destructuration mechanisms was evaluated. To avoid any misunderstanding, it should be emphasized that the omission of the frictional destructuration implies only that the M remains intact, whereas the deviatoric (shear) strain rate is clearly influential in regard to the isotropic destructuration since it enters the definition of the destructuration plastic strain rate of equation (5), where A is different from zero with a typical default value of $A = 0,5$.

Observe that by setting $C = 0$ and starting with $\alpha = 0$, the anisotropy feature of the model can be deactivate by setting $\kappa_i = 0$ or simply by starting with $S_i = 1$. To fully reduce the model to the modified Cam-clay model, in addition to the previous choices, one should also remove the Lode angle dependency by setting $m = 1$.

1.4.2.2   Calibration of constants

SANICLAY requires the calibration of eight constants (Table 1.1). Only the last three (N, x, C) are new in regards to the constants required for the application of the modified Cam clay model.

Constants	Description of its rule
M_c	Value of stress ratio $\eta = \frac{q}{p}$ at critical state in compression
M_e	Value of stress ratio $\eta = \frac{q}{p}$ at critical state in extension
λ	Compressibility of normally consolidated NC clay
κ	Compressibility of overconsolidated OC clay
ν	Elastic Poisson's ratio

N	Shape of yield surface
x	Saturation limit of anisotropy (under path with $\eta = \frac{q}{p} = constant$)
C	Rate of evolution of anisotropy

Table 1.1- Constants of SANICLAY model.

The calibration of these constants requires data from well-established laboratory tests:

- One-dimensional (K_0) or preferably isotropic consolidation tests with at least one unload-reload cycle using an oedometer or a triaxial device (for constants κ, λ).;

- Lateral stress measurements during one-dimensional (K_0) compression and swelling reaching stresses (for constants x, ν);

- Undrained triaxial compression (CK_0UC) and extension (CK_0UE) tests on normally K_0-consolidated clay (for constants M_c and Me, N, C).

Figure 1.6 presents the response of clay during one-dimensional (CK_0) and isotropic (CI) compression and swelling, with lateral stress measurement. Given the latter, the stress variation is presented in the e-logp space of the figure.
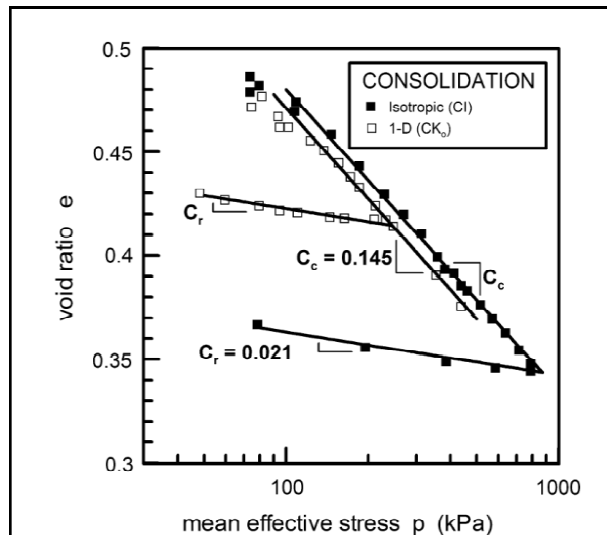
Figure 1.6 - Calibration of constants k and λ, via C_r and C_c.

The C_c and C_r slopes that are measured in Figure 3.5 are related to λ and κ as: $\lambda = \dfrac{C_c}{ln10}$

$$\text{and } \kappa = \frac{C_r}{ln10}.$$

Notice that a unique value of $M = M_c = M_e$ is not advised for use, since it seriously overstimates the clay strength in extension. Hence, when only a CK_0UC test is available, then $M_{e,min} \leq M_e < M_c$ should hold, where $M_{e,min}$ is the M_c corresponding to $\varphi_e = \varphi_c$.

Figure 1.7 focuses on the K_0-unloading stress path of a clay; this path presented with a dashed grey line in this figure is the average curve that fits the initial data points of the K0-consolidated undrained triaxial compression ($CK0UC$) and extension (CK_0UE) tests.
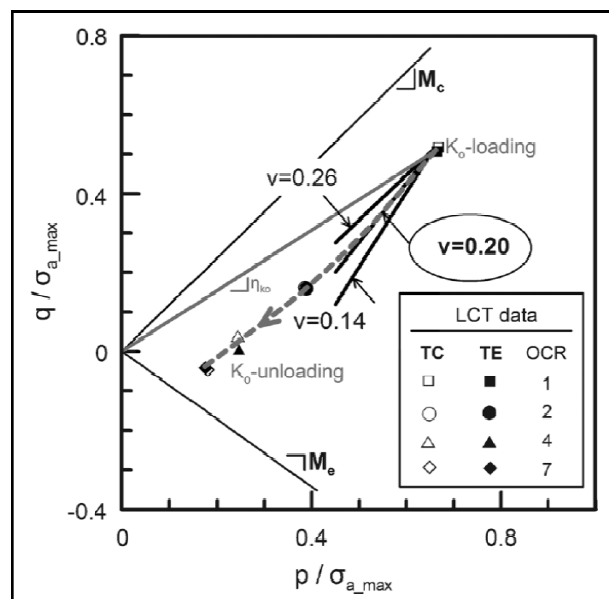
***Figure 1.7** - Calibration of constant v.*

As an approximation, the initial part of this path is proposed for use in the calibration of the Elastic Poisson's ratio v of the clay.

For x and N, the use of closed-form analytical relations is proposed, which makes their calibration easy and straightforward. For the estimation of constant x, the case of a drained path with $\eta = \eta_\kappa = constant$ is considered. Practically speaking, all

consolidation paths starting from slurry have this characteristic. After considerable algebra, a closed-form relation for x is:

$$\alpha_k = \frac{\eta_k}{x} = \frac{B\varepsilon\eta_k{}^3 + \eta_k^2 + \left[2\left(1-\frac{k}{\lambda}\right) - BM_c^2\right]\varepsilon\eta_k - M_c^2}{2\varepsilon\left(1-\frac{k}{\lambda}\right)}, \qquad B = -\frac{2(1+\nu)k}{9(1-2\nu)\lambda}$$

Different paths with $\eta_k = constant$ correspond to different ε values, which are not always a priori known. Of all possible such paths, the most frequently run is the K_0-loading path, for which $\varepsilon = 3/2$ and $\eta_k = \eta_{k0} = \frac{3(1-K_0)}{1+2K_0}$, where K_0 is the measured value of the earth coefficient at rest. In the absence of K_0 measurements, the K0 can be estimated from well-known empirical relations, such as the $K_0 = 1 - sin\varphi$ for NC clays. Anyway, having obtained the K0 value, one may estimate the value of constant x using equation: $\alpha_k = \frac{\eta_k}{x} = \frac{B\varepsilon\eta_k{}^3 + \eta_k^2 + \left[2\left(1-\frac{k}{\lambda}\right) - BM_c^2\right]\varepsilon\eta_k - M_c^2}{2\varepsilon\left(1-\frac{k}{\lambda}\right)}$. In general, for given values of k, λ, M_c and ν (the MCC model constants), constant x is an increasing function ok K_0, unlike the MCC model, which is known for overestimating the K_0 value.

Similarly for the estimation of constant N the case of an undrained shearing stress at his considered. Given the available tests for calibration of the model constants it is the CK0UC test on normally consolidates clay that is suitable for the purpose at hand. In this case, the initial $\eta_{in} = \beta = \eta_{k0} = \frac{3(1-K_0)}{1+2K_0}$ and $p_{in} = p_{k0}$, while $\eta_f = M_c$. When these two pair of (p, η) are inserted in the aforementioned equation of the undrained stress path one has:

$$\frac{p_f}{p_{k0}} = \left(\frac{N^2 - \eta_{k0}^2}{N^2 - 2\eta_{k0}M_c + M_c^2}\right)^{1-\left(\frac{k}{\lambda}\right)}$$

Hence, one merely needs to solve the equation for N, given data of a CK_0UC test on normally consolidated clay.

Finally the calibration of constant C requires the execution of trial runs, having all other constants calibrated in advance. Constant C quantifies the rate of rotation and distortion of the yield surface and the plastic potential surface. Hence, test appropriate for its calibration are those that induce significant surface rotation, test for which the η_{in} is far

from η_f of the effective stress path, and possibly the opposite sign. Practically a CK$_0$UE test on normally consolidated clay is very suitable for the purpose at hand. Hence, Figure 1.8 presents the CK$_0$UE test data on normally consolidated clay, along with a series of trial runs fir C = 6, 11, 16, 21 and 26. Observe that the higher the value of C the larger the predicted undrained strength in triaxial extension.
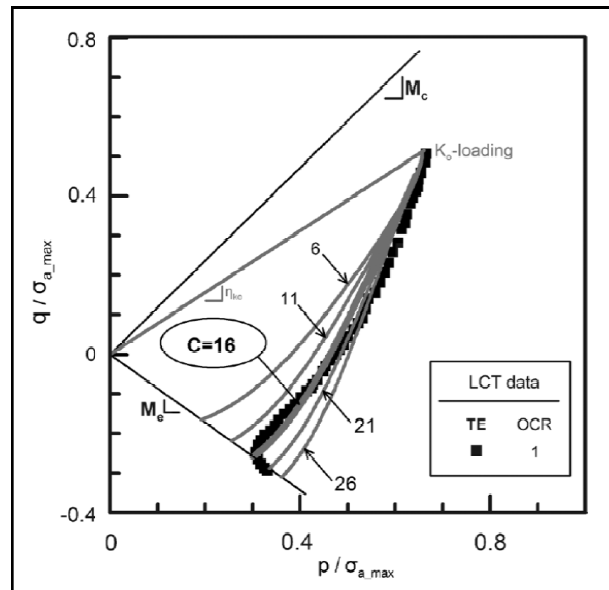
***Figure 1.8** - Calibration of constant C.*

Experience has shown that constant C usually varies between 3 and 20 for various clays. In cases when the C takes large values (e.g. C>8) the adopted N should be slightly increased compared to the value from equation

$$\frac{p_f}{p_{k0}} = \left(\frac{N^2 - \eta_{k0}^2}{N^2 - 2\eta_{k0}M_c + M_c^2} \right)^{1-\left(\frac{k}{\lambda}\right)}$$

because the basic assumption of a non-rotating yield surface is no longer valid.

Chapter 2 - Effect of boundary conditions

The first part of this study deals with the principles of the program FLAC^{3D} and how it works. The objective is to be able to use basic commands with mastery in order to create models, analyze their dynamic behaviour and to understand the differences in the responses by applying different boundary conditions.

FLAC^{3D} is a three-dimensional explicit finite-difference program for engineering mechanics computation. The program extends the analysis capability of FLAC (*2D*) into three dimensions, simulating the behaviour of three-dimensional structures built of soil, rock or other materials that undergo plastic flow when their yield limits are reached. Materials are represented by polyhedral elements within a three-dimensional grid that is adjusted by the user to fit the shape of the object to be modelled. Each element behaves according to a prescribed linear or nonlinear stress/strain law in response to applied forces or boundary restraints. The explicit, *Lagrangian*, calculation scheme and the mixed-discretization zoning technique used in FLAC^{3D} ensure the plastic collapse and flow are modelled very accurately. FLAC^{3D} offers an ideal analysis tool for solution of three-dimensional problems in geotechnical engineering. (*FLAC^{3D} Manual*)

2.1   Model construction

2.1.1 Create the geometry and assign material models

Figure 2.1 shows the initial model used for the analyses.
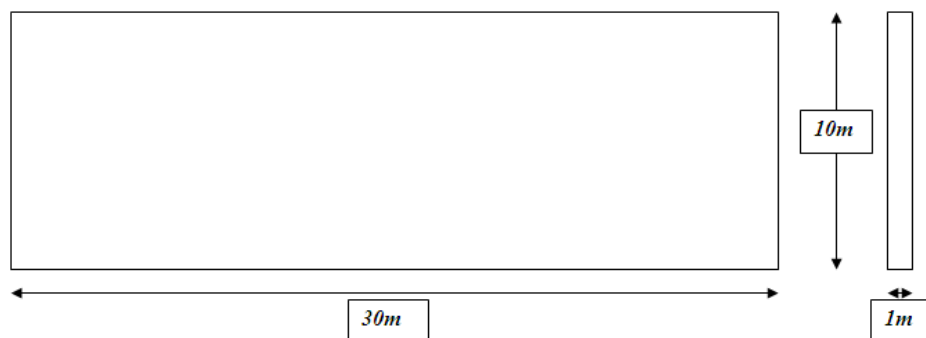
Figure 2.1 – Geometry of the model.

The following are the material parameters used in the analyses:

Model: Elastic

Properties: Bulk   modulus   (K) $= 2 \cdot 10^6 \ kPa$

Shear   modulus   (G) $= 0{,}3 \cdot 10^5 \ kPa$

Density   (ρ) $= 2 \cdot 10^3 \ \frac{kg}{m^3}$

2.1.2   Finite difference Mesh

Numerical perturbation of the propagating wave can occur in a dynamic analysis as a function of the modelling conditions. Both the frequency content of the input wave and the waves peed characteristics of the system will affect the numerical accuracy of wave transmission. Kuhlemeyer and Lysmer (*1973*) have shown that, for accurate representation of wave transmission through a model, the spatial element size, *Δl*, must be smaller than approximately one-tenth to one-eighth of the wavelength associated with the highest frequency of the input wave:

$$\Delta l \leq \frac{\lambda}{10} \div \frac{\lambda}{8}$$

where λ is the wavelength associated with the highest frequency component that contains appreciable energy. (*FLAC^{3D} Manual*)

For the model in *Fig.2.1*:

$$\Delta l \leq \frac{\lambda}{10}$$

$$\lambda = \frac{v_s}{f_{max}}$$

$$v_s = \sqrt{\frac{G}{\rho}} = \sqrt{\frac{30000}{2}} = \sqrt{15000} = 122{,}5 \ \frac{m}{s}$$

$$f_1 = \frac{v_s}{4 \cdot H} = \frac{122{,}5}{4 \cdot 10} = 3{,}06 \ Hz \quad 1^{st} \ natural \ frequency$$

Consider the following case:

$$f_{max} = 4Hz$$

$$\lambda = \frac{v_s}{f_{max}} = \frac{122,5}{4} = 30,6 \, m$$

$$\Delta l \leq \frac{\lambda}{10} \leq \frac{30,6}{10} = 3,0 \, m$$

Whereby in *x*-direction (*30m*) there must be at least 10 elements, in *y*-direction (*1m*) at least 1 element and in the *z*-direction (*10m*) 4 elements.

The mesh of the model consists of 15 elements in *x*-direction,   1   element   in   *y*-direction and 5 elements in *z*-direction.

Figure 2.2 shows the model and mesh created in this example.
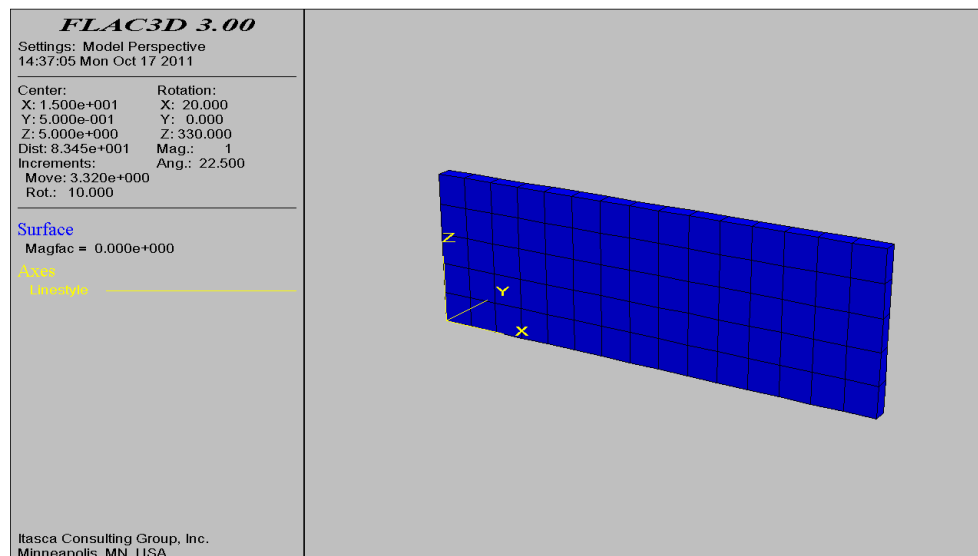
Figure 2.2 - *Geometry and mesh.*

2.1.3   Boundary conditions

To investigate the performances of different boundary conditions, the model is constrained in different ways in the dynamic analysis; three different types of boundary conditions are considered:

- *Simple roller*
- *Free field boundary conditions.* This kind of boundary is implemented in FLAC^{3D} and it "enforce" the free-field motion in such a way that boundaries retain their non-reflecting properties.
- *Simple roller with rigid-link.* Similar to the first case, but a rigid link is applied between two points lying at the same height on the two side boundaries

2.1.4 Dynamic input

The dynamic input is applied at the bottom of the model in the form of an acceleration in *x*-direction.

The dynamic input has the following expression:

$$a(t) = \sin(\omega t)$$
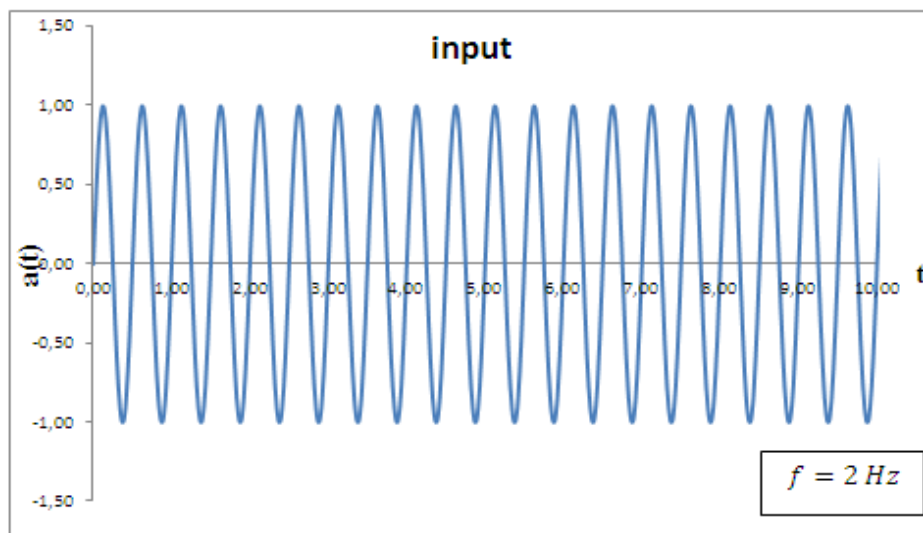
***Figure 2.3** - Graphic of the input wave.*

The input is inserted into the program by creating a table and recalling it during the analysis.

2.2 Comparison between different boundaries conditions

2.2.1   Simple roller
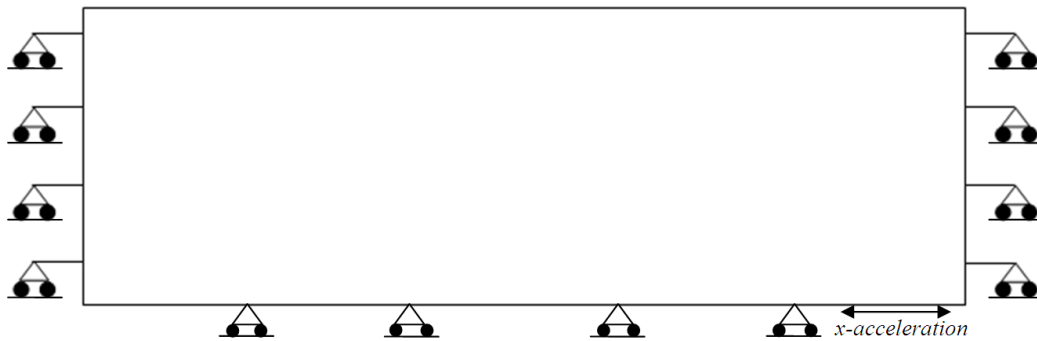
***Figure 2.4** – Model with simple roller boundary conditions.*

This type of constrain, applied on the two sides of the model, permit only the displacement in *x*-direction while *z*-displacements and *y*-displacements are blocked. The bottom of the model is fixed in *x* and *y* directions, only the *x*-displacements are free in order to apply the x-acceleration (*Fig.2.5*).
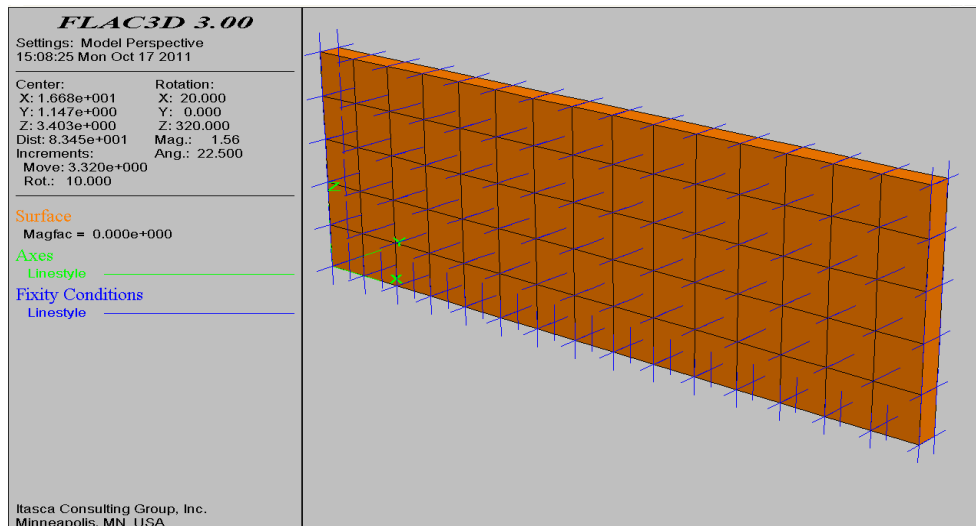
***Figure 2.5 -** Boundary Conditions*

There are some commands in this script related to damping. This will be discussed later. The results of the analysis are reported into a graphics *x-acceleration/dynamic time*

(*Fig.2.7*) where *x*-acceleration is referred to point *A*, in the middle of the top of the model (*Fig.2.6*).
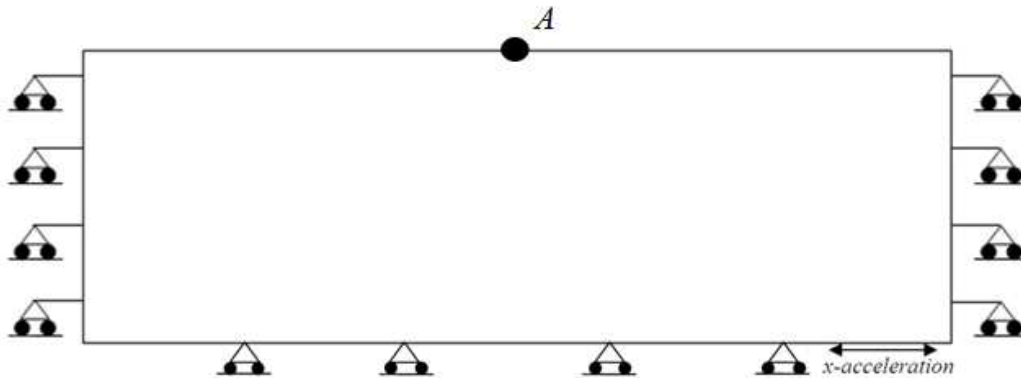
Figure 2.6 - *Position of the check point where the acceleration is measured.*
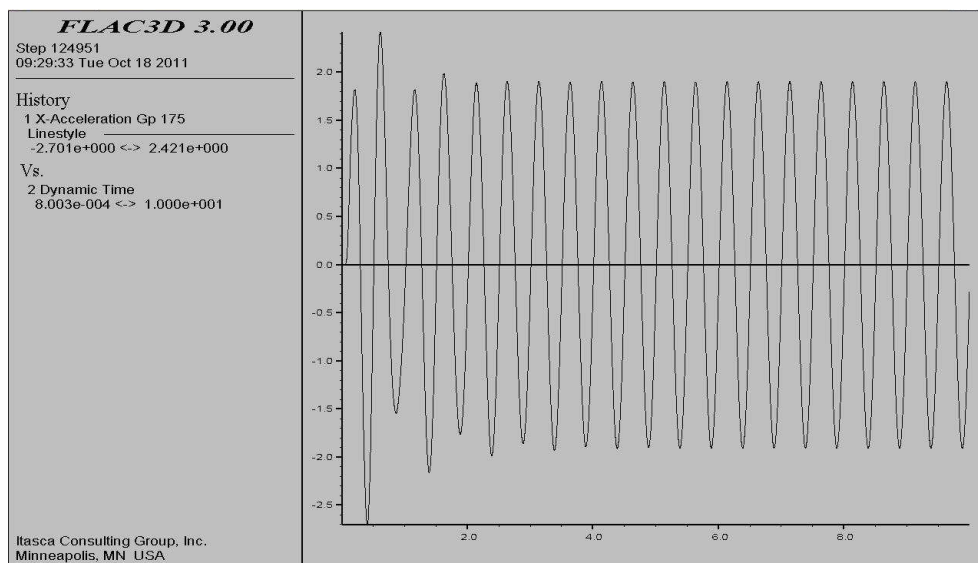
Figure 2.7 - *Results of the analysis with simple roller boundary conditions (graphics: x-acceleration vs dynamic time).*

2.2.2　　　Free-field boundary conditions

Numerical analysis of the seismic response of surface structures such as dams, slopes, walls, etc. requires the discretization of a region of material adjacent to the foundation. The seismic input is normally represented by plane waves propagating upward through the underlying material. The boundary conditions at the sides of the model must account

for the free-field motion that would exist in the absence of the structure. In some cases, elementary lateral boundaries, such as roller boundary, may be sufficient. These boundaries should be placed at sufficient distances to minimize wave reflections and achieve free-field conditions. For soils with high material damping, this condition can be obtained with relatively small distance and the results of the analysis are not influenced by the presence of the boundaries. However, when the material damping is low, the required distance may lead to an impractical model. An alternative procedure, developed also for FLAC[3D], is to "enforce" the free-field motion in such a way that boundaries retain their non-reflecting proprieties. FLAC[3D] involves the execution of free-field calculations in parallel with the main-grid analysis. The lateral boundaries of the main grid are coupled to the free-field grid by viscous dashpots to simulate a quiet boundary (*Fig. 2.8*), and the unbalanced forces from the free-field grid are applied to the main-grid boundary. Both conditions are expressed in the following equations, which apply to the free-field boundary along one side boundary plane with its normal in the direction of the *x-axis*.
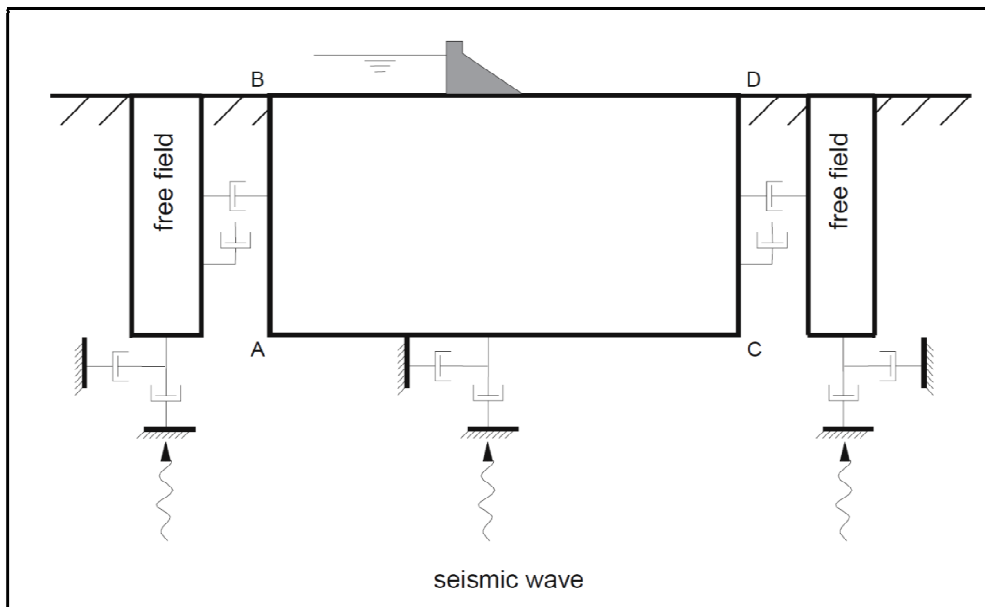
Figure2.8 - Model for seismic analysis of surface structures and free-field mesh

$$F_x = -\rho C_p \left(v_x^m - v_x^{ff} \right) A + F_x^{ff}$$

$$F_y = -\rho C_s \left(v_y^m - v_y^{ff} \right) A + F_y^{ff}$$

$$F_z = -\rho C_s \left(v_z^m - v_z^{ff} \right) A + F_z^{ff}$$

where:

ρ = density of material along vertical model boundary;

C_p = p-wave speed at the side boundary;

C_s = s-wave speed at the side boundary;

A = area of influence of free-field gridpoint;

v_x^m = x-velocity of gridpoint in main grid at side boundary;

v_y^m = y-velocity of gridpoint in main grid at side boundary;

v_z^m = z-velocity of gridpoint in main grid at side boundary;

v_x^{ff} = x-velocity of gridpoint in side free field;

v_y^{ff} = y-velocity of gridpoint in side free field;

v_z^{ff} = z-velocity of gridpoint in side free field;

F_x = free-field gridpoint force with contributions from the σ_{xx}^{ff} stresses of the free-field zones around the gridpoint;

F_y = free-field gridpoint force with contributions from the σ_{xy}^{ff} stresses of the free-field zones around the gridpoint;

F_z = free-field gridpoint force with contributions from the σ_{xz}^{ff} stresses of the free-field zones around the gridpoint;

In this way, plane waves propagating upward are not distorted at the boundary because the free-field grid supplies conditions that are identical to those in an infinite model. If the main grid is uniform, and there is no surface structure, the lateral dashpots are not exercised because the free-field grid executes the same motion as the main grid. However, if the main-grid motion differs from that of the free field, then the dashpots

act to absorb energy in a similar manner to quiet boundaries. In order to apply the free-field boundary in FLAC[3D], the model must be oriented such that the base is horizontal and its normal is in the direction of the z-axis, and the sides are vertical and their normal are in the direction of either the *x-* or *y-axis*. If the direction of propagation of the incident seismic waves is not vertical, then the coordinate axes can be rotated such that the *z*-axis coincides with the direction of propagation. In this case, gravity will act at an angle to the *z*-axis, and horizontal free surface will be inclined with respect to the model boundaries. The free-field model consists of four plane free-field grids, on the side boundaries of the model and four column free-field grids at the corners (*Fig.2.9*). (*FLAC[3D] Manual*)
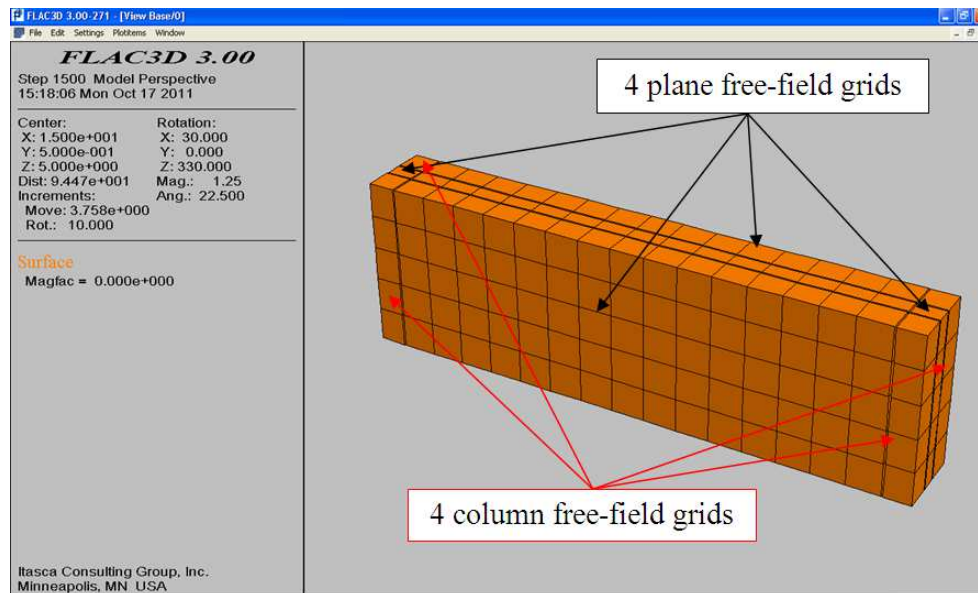
Figure 2.9 - Free Field boundary conditions

The plane grids are generated to match the main-grid zone on the side boundaries, so that there is a one-to-one correspondence between gridpoints in the free field and the main grid. The four corner free-field columns act as free-field boundaries for the plane free-field grids. The plane free-field grids are two-dimensional calculations that assume infinite extension in the direction normal to the plane. The column free-field grids are one-dimensional calculations that assume infinite extension in both horizontal directions. Both the plane and column grids consist of standard FLAC[3D] zones, which have gridpoints constrained in such a way to achieve the infinite extension assumption.

The model should be in static equilibrium before the free-field boundary is applied. The free-field condition is applied to lateral boundary gridpoints. All zone data in the model zones adjacent to the free field are copied to the free-field region. Free-field stresses are assigned the average stress of the neighbouring grid zone. The dynamic boundary conditions are automatically transferred to the free field when the free field is applied. Any model or nonlinear behaviour may exist in the free field, as well as fluid coupling and flow within the free field. The free field supports both small- and large-strain calculation modes (*FLAC³ᴰ manuals*).

The results of the analysis are reported into a graphics *x-acceleration/dynamic time* (*Fig.2.10*) where *x*-acceleration is referred to point *A* (*Fig.2.6*).
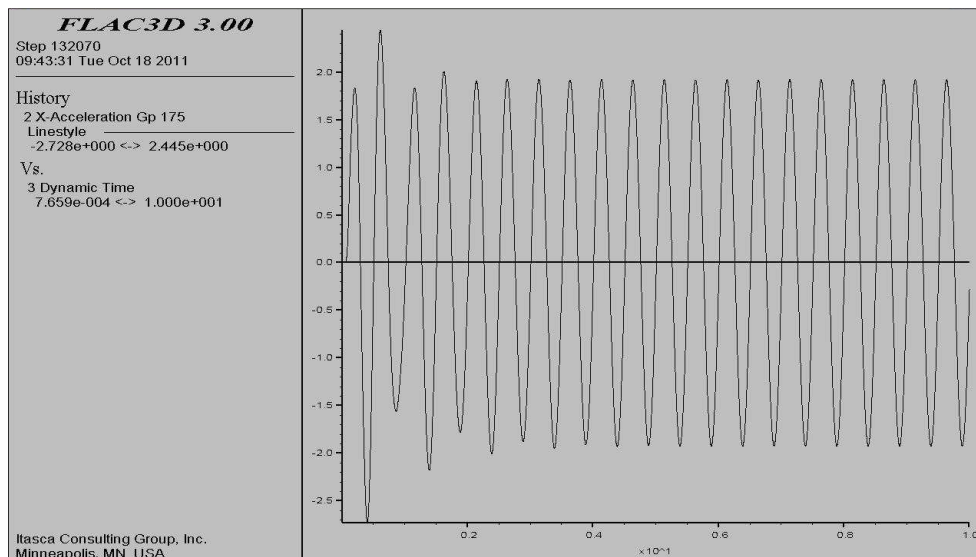
Figure 2.10 - results of the analysis with free field boundary conditions (graphics: x-acceleration vs dynamic time).

2.2.3   Simple roller boundary conditions with rigid link
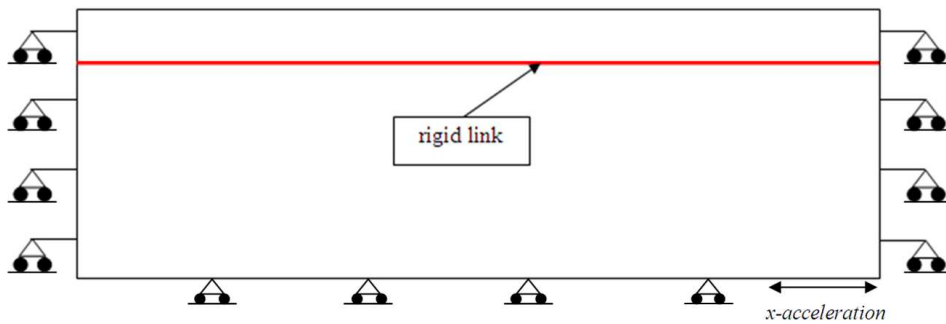
Figure 2.11 *– Model with simple roller boundary conditions and a rigid link between two points on the sides of the model.*

The boundary conditions are similar to the first case: simple rollers applied on the two sides of the model that permit only *x*-displacements (*Fig.2.13*). Furthermore, a rigid link (*Fig.2.12*) is applied between two points lying at the same height on the two side boundaries. The rigid link is model like a cable element with a large value of the product $E \cdot A$ (*E: Young's modulus*, *A: section area*). The link enforces the two points to have the same horizontal displacements like a free-field condition.
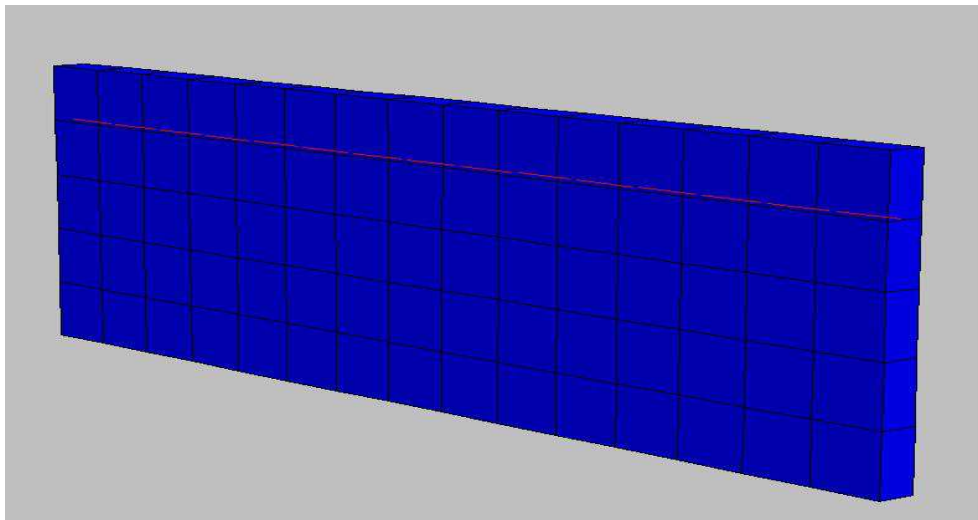
Figure 2.12 - *Geometry of the model with the rigid link*
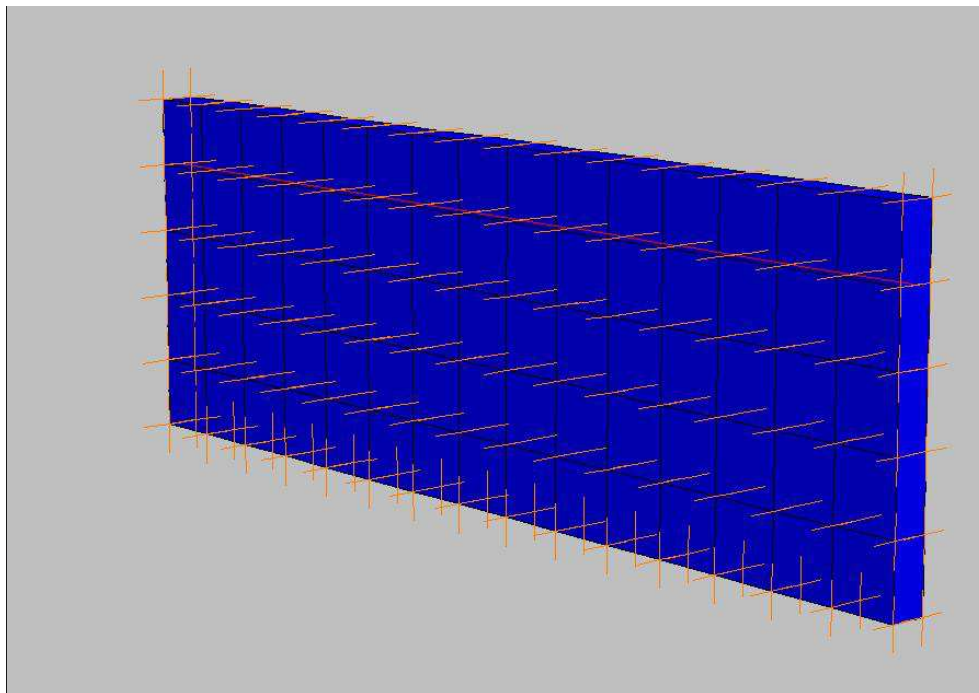
Figure 2.13 - *Boundary conditions*

The results are showing *Figure.2.14*.
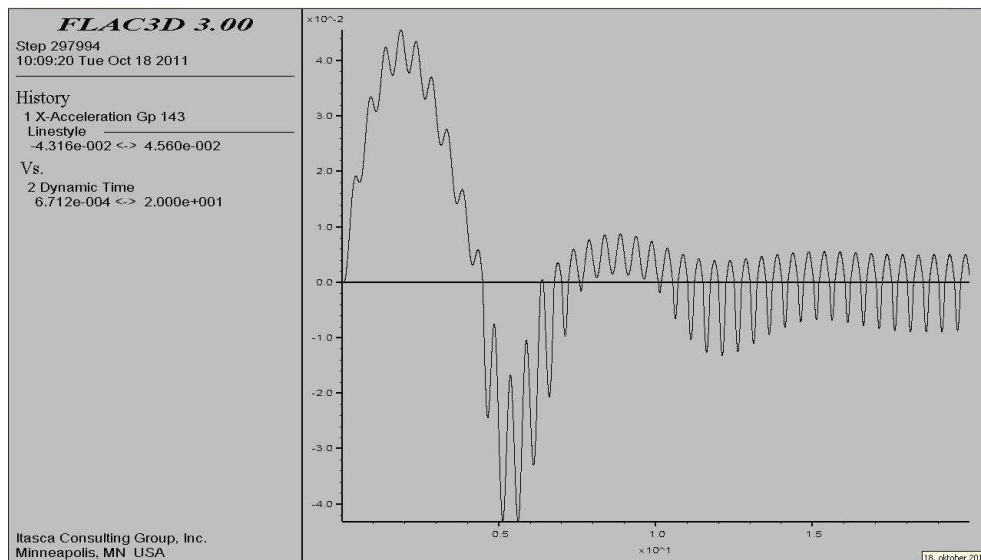
Figure 2.14 - *results of the analysis with simple roller on the sides and a rigid link between two points (graphics: x-acceleration vs dynamic time).*

2.2.4   Summary

For an easy comparison, the time histories of point *A* (*Fig.2.6*) are showing in *Figures 2.15, 2.16* and *2.17*.
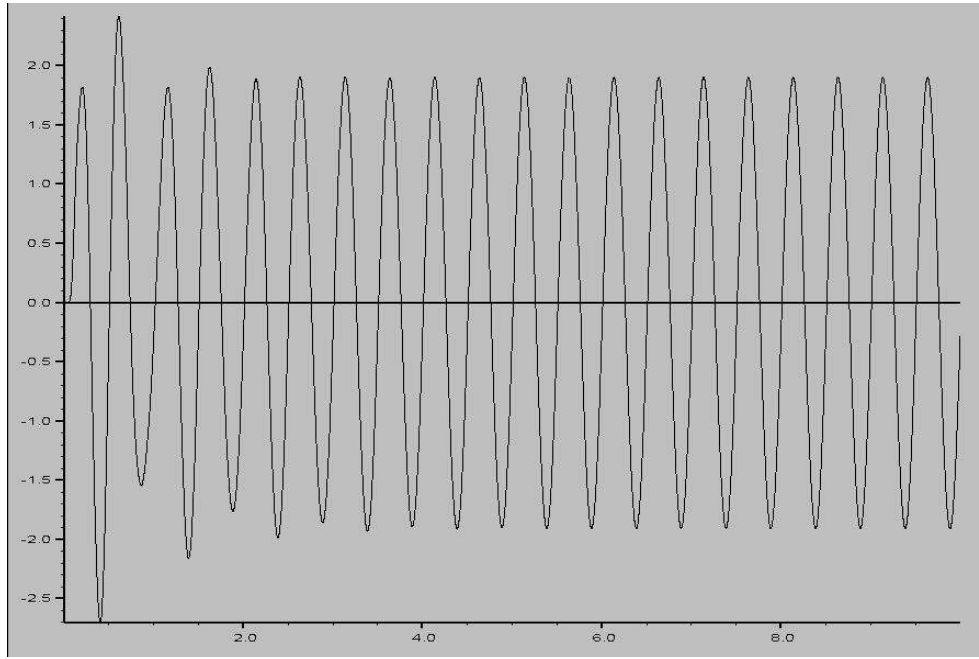
Figure 2.15 - *Results of simple roller boundary conditions.*
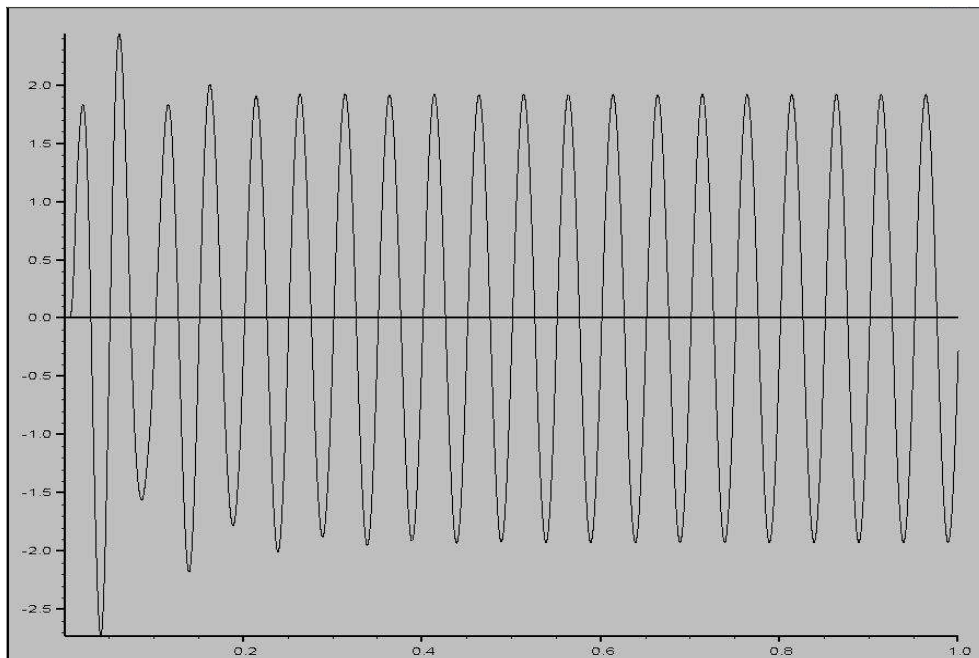
Figure 2.16 - *Results of free field boundary condiutions.*
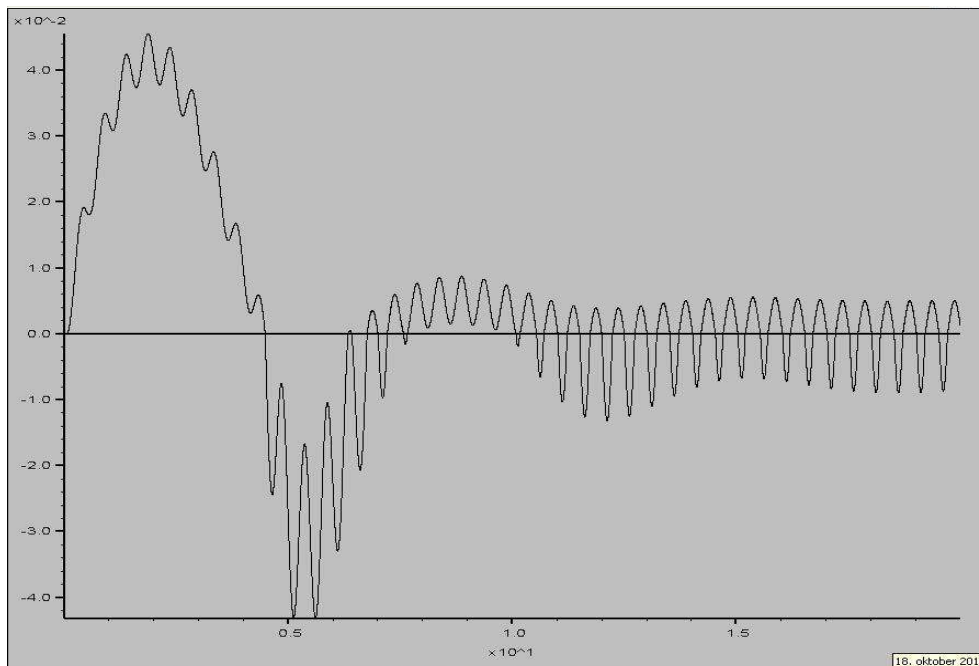
Figure 2.17 - *Results of simple roller on the sides and rigid link.*

From the results it appears that *simple roller boundary conditions* give the same answer of *free field boundary conditions*, while in the case of *simple roller boundary conditions with rigid link* one gets a gives a different result which is not correct. No attempt has been made to do a more detailed investigation on this model. It should also be noted that for this regular mesh and uniform model, it was expected that the result of roller boundary be the right one. This will not be the case in more general, non-homogeneous models.

2.3   Ground response analysis: comparison between analytical solution and FLAC³ᴰ solution

2.3.1 Introduction

One of the most important and most commonly encountered problems in geotechnical earthquake engineering is the evaluation of ground response. Ground response analyses are used to predict ground surface motions for development of design response spectra, to evaluate dynamic stresses and strain for evaluation of liquefaction hazards, and to determine the earthquake-induced forces that can lead to instability of earth-retaining structures. Under ideal conditions, a complete ground response analysis would model the rupture mechanism at the source of an earthquake, the propagation of stress waves through the earth to the top of bedrock beneath a particular site, and would then determine how the ground surface motion is influenced by the soils that lie above the bedrock. In reality, the mechanism of fault rupture is so complicated and the number of energy transmission between the source and the site so uncertain that this approach is not practical for common engineering applications. The problem of ground response analysis then becomes one of determining the response of the soil deposit to the motion of the bedrock immediately beneath it. Despite the fact that seismic waves may travel through tens of kilometres of rock and often less than 100m of soil, the soil plays a very important role in determining the characteristics of the ground surface motion. (*Kramer, 1996*)

2.3.2   One-dimensional ground response analysis

When a fault ruptures below the earth's surface, body waves travel away from the source in all directions. As they reach boundaries between different geologic materials, they are reflected and refracted. Since the wave propagation velocities of shallower materials are generally lower than the materials beneath them, inclined rays that strike horizontal layer boundaries are usually refracted to a more vertical direction. By the time the rays reach the ground surface, multiple refractions have often bent them to a nearly vertical direction (*Fig.2.18*).
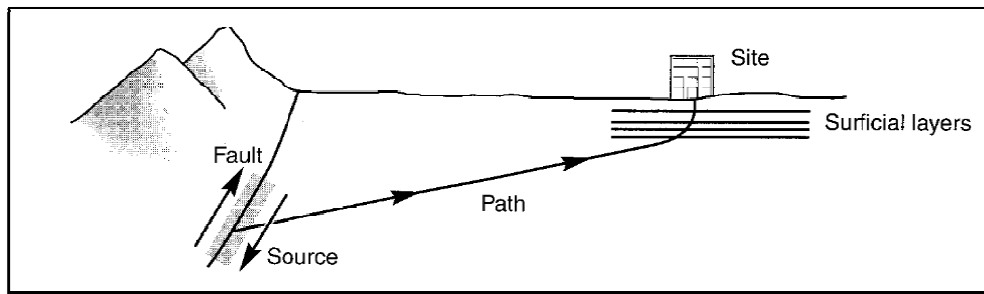
Figure 2.18 - *Refraction process that produces nearly vertical wave propagation near the ground surface (Kramer, 1996).*

One-dimensional ground response analyses are based on the assumption that all boundaries are horizontal and that the response of a soil deposit is predominantly caused by SH-waves propagating vertically from the underlying bedrock. For one-dimensional ground response analysis, the soil and bedrock surface are assumed to extend infinitely in the horizontal direction.

An important class of techniques for ground response analysis is also based on the use of transfer functions. For the ground response problem, transfer functions can be used to express various response parameters, such as displacement, velocity, acceleration, shear stress, and shear strain, to an input motion parameter such as bedrock acceleration. Because it relies on the principle of supposition, this approach is limited to the analysis of linear system. Non linear behavior can be approximated, however, using an iterative procedure with equivalent linear soil proprieties. Although the calculation of the transfer function involves manipulation of complex numbers, the approach itself is quite simple. A known time history of bedrock (input) motion is represented as a Fourier series. Each term in the Fourier series of the bedrock (input) motion is then multiplied by the transfer function to produce the Fourier series of the ground surface (output) motion. The ground surface (output) motion can then be expressed in the time domain using the inverse FFT (Fast Fourier transform). Thus the transfer function determines how each frequency in the bedrock (input) motion is amplified, or deamplified, by the soil deposit. The key to the linear approach is the evaluation of transfer function. (Kramer, 1996)

a) *Uniform undamped soil on rigid rock*

First, consider a uniform layer of isotropic, linear elastic soil overlying rigid bedrock (*Fig.2.19*).
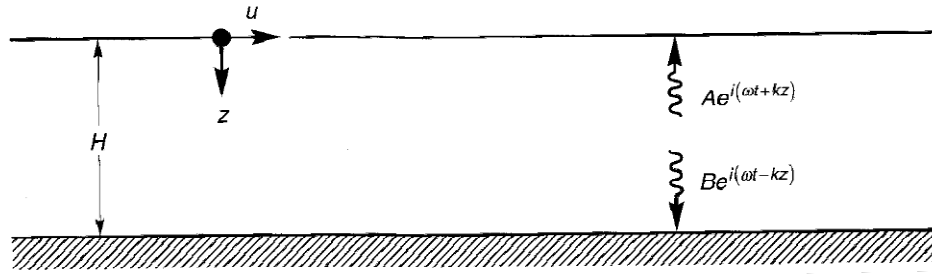
Figure 2.19 - *Linear elastic soil deposit of thickness H underlain by rigid bedrock.*
(Kramer, 1996)

Harmonic horizontal motion of the bedrock will produce vertically propagating shear waves in the overlying soil. The resulting horizontal displacement can be expressed:

$$u(z,t) = Ae^{i(\omega t + kz)} + Be^{i(\omega t - kz)} \quad (1.1)$$

Where ω is the circular frequency of ground shaking, k the wave number $\left(k = \frac{\omega}{v_s}\right)$ and A and B the amplitudes of waves travelling in the $-z$ (upward) and $+z$ (downward) directions, respectively. At the free surface $(z = 0)$, the shear stress, and consequently the shear strain, must vanish; that is:

$$\tau(0,t) = G\gamma(0,t) = G\frac{\partial u(0,t)}{\partial z} = 0 \quad (1.2)$$

Substituting (*1.1*) into (*1.2*) and differentiating yields

$$G \cdot i \cdot k \cdot \left(Ae^{ik(0)} - Be^{ik(0)}\right)e^{i\omega t} = G \cdot i \cdot k \cdot (A - B)e^{i\omega t} = 0 \quad (1.3)$$

Which is satisfied (nontrivially) when $A = B$. The displacement can then be expressed as:

$$u(z,t) = 2A\frac{e^{ikz} + e^{-ikz}}{2}e^{i\omega t} = 2A\cos kz\, e^{i\omega t} \quad (1.4)$$

Which describes a standing wave of amplitude $(2A \cos kz)$. The standing wave is produced by the constructive interference of the upward and downward travelling waves and has a fixed shape with respect to depth. Equation (1.4) can be used to define a transfer function that describes the ratio of displacement amplitudes at any two points in the soil layer. Choosing these two points to be the top and the bottom of the soil layer gives the transfer function

$$F_1(\omega) = \frac{u_{max}(0,t)}{u_{max}(H,t)} = \frac{2Ae^{i\omega t}}{2A \cos kH e^{i\omega t}} = \frac{1}{\cos kH} = \frac{1}{\cos\left(\frac{\omega H}{v_s}\right)} \qquad (1.5)$$

The modulus of the transfer function is the amplification function

$$|F_1(\omega)| = \sqrt{\{Re[F_1(\omega)]\}^2 + \{Im[F_1(\omega)]\}^2} = \frac{1}{\left|\cos\left(\frac{\omega H}{v_s}\right)\right|} \qquad (1.6)$$

Which indicates that the surface displacement is always at least as large as the bedrock displacement (since the denominator can never be greater than *1*) and, at certain frequencies, is much larger. Thus $|F_1(\omega)|$ is the ratio of the free surface motion amplitude to the bedrock motion amplitude. As $\left(\frac{\omega H}{v_s}\right)$ approaches $\left(\frac{\pi}{2} + n\pi\right)$, the denominator of equation (*1.6*) approaches zero, which implies that amplification, or resonance, will occur (*Fig.2.20*). Even this very simple model illustrates that the response of a soil deposit is highly dependent upon the frequency of the base motion, and that the frequencies at which strong amplification occurs depend on the geometry (thickness) and material properties (s-wave velocity) of the soil layer.(*Kramer, 1996*)
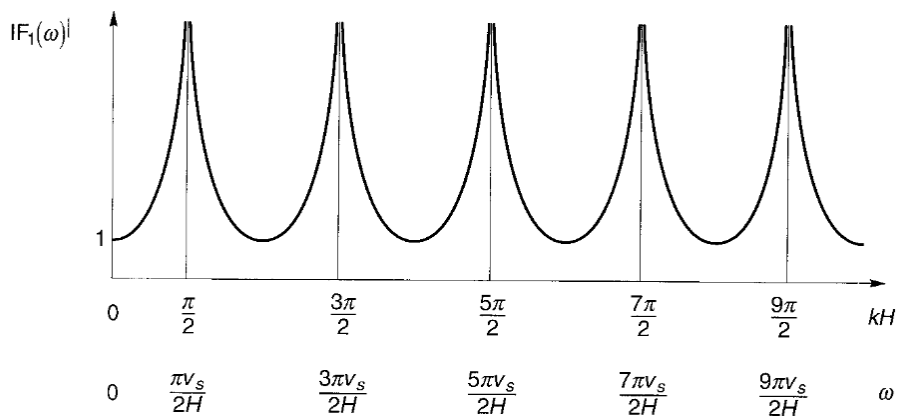
Figure 2.20 - *Influence of frequency on steady-state response of undamped linear elastic layer. (Kramer, 1996)*

b) Uniform, damped soil on rigid rock

Obviously, the type of unbounded amplification predicted by the previous analysis cannot physically occur. The previous analysis assumed no dissipation of energy, or damping, in the soil. Since damping is present in all materials, more realistic results can be obtained by repeating the analysis with damping. Assuming the soil to have the shearing characteristics of a *Kelvin-Voigt* solid, the wave equation can be written as

$$\rho \frac{\partial^2 u}{\partial t^2} = G \frac{\partial^2 u}{\partial z^2} + \eta \frac{\partial^3 u}{\partial z^2 \partial t} \qquad (1.7)$$

The solution to this wave equation is of the form

$$u(z,t) = A e^{i(\omega t + k^* z)} + B e^{i(\omega t - k^* z)}$$

where k^* is a complex wave number with real part k_1 and imaginary part k_2. Repeating the previous algebraic manipulation with the complex wave number, the transfer function for the case of damped soil over rigid rock can be expressed as

$$F_2(\omega) = \frac{1}{\cos k^* H} = \frac{1}{\cos\left(\frac{\omega H}{v_s^*}\right)} \qquad (1.8)$$

Since the frequency-independent complex shear modulus is given by $G^* = G(1 + i2\xi)$, the complex shear wave velocity can be expressed as

$$v_s^* = \sqrt{\frac{G^*}{\rho}} = \sqrt{\frac{G(1+2i\xi)}{\rho}} \approx \sqrt{\frac{G}{\rho}}(1 + i\xi) = v_s(1 + i\xi) \qquad (1.9)$$

for small ξ. Then the complex wave number can be written, again for small ξ, as

$$k^* = \frac{\omega}{v_s^*} = \frac{\omega}{v_s(1+i\xi)} \approx \frac{\omega}{v_s}(1 - i\xi) = k(1 - i\xi) \qquad (1.10)$$

And finally, the transfer function, as

$$F_2(\omega) = \frac{1}{\cos k(1-i\xi)H} = \frac{1}{\cos\left[\frac{\omega H}{v_s}(1+i\xi)\right]} \qquad (1.11)$$

Using the identity $|\cos(x + iy)| = \sqrt{\cos^2 x + \sinh^2 y}$, the amplification function can be expressed as

$$|F_2(\omega)| \approx \frac{1}{\sqrt{\cos^2 kH + (\xi kH)^2}} = \frac{1}{\sqrt{\cos^2\left(\frac{\omega H}{v_s}\right) + \left[\xi\left(\frac{\omega H}{v_s}\right)\right]^2}} \qquad (1.13)$$

For small damping ratios, equation (*1.13*) indicates that amplification by a damped soil layer also varies with frequency. The amplification will reach a local maximum whenever $kH \approx \left(\frac{\pi}{2} + n\pi\right)$ but will never reach a value of infinity since (for $\xi > 0$) the denominator will always be greater than zero. The frequencies that correspond to the local maxim are the natural frequencies of the soil deposit. The variation of amplification factor with frequency is shown for different levels of damping in figure (*Fig 2.21*). This amplification factor is also equal to the ratio of the free surface motion amplitude to the bedrock motion amplitude. *Figure (Fig 2.21)* shows that damping affects the response at high frequencies more than at lower frequencies.
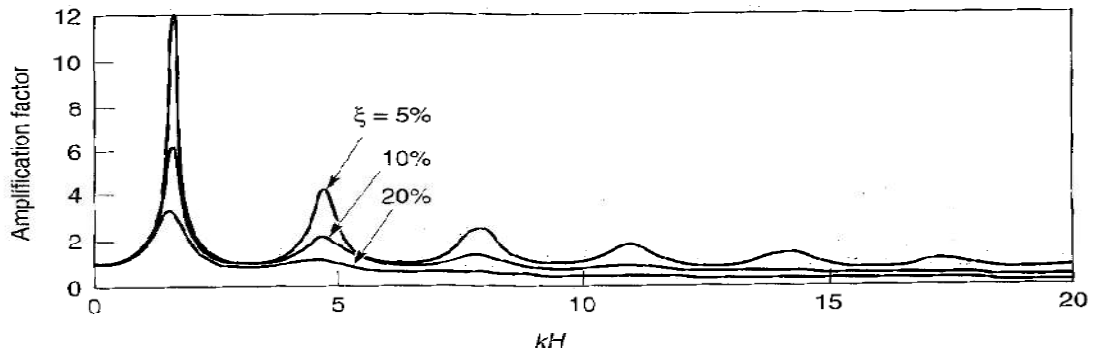
Figure 2.21 - *influence of frequency on steady-state response of damped, linear elastic layer.(Kramer, 1996)*

The (*n*th) natural frequency of the soil deposit is given by

$$\omega_n \approx \frac{v_s}{H}\left(\frac{\pi}{2} + n\pi\right) \qquad\qquad n = 0,1,2,\dots,\infty \qquad (1.14)$$

Since the peak amplification factor decreases with increasing natural frequency, the greatest amplification factor will occur approximately at the lowest natural frequency, also known as the fundamental frequency

$$\omega_0 = \frac{\pi v_s}{2H} \qquad (1.15)$$

The period of vibration corresponding to the fundamental frequency is called the characteristic site period,

$$T_s = \frac{2\pi}{\omega_0} = \frac{4H}{v_s}$$

The characteristic site period, which depends only on the thickness and shear wave velocity of the soil, provides a very useful indication of the period of vibration at which the most significant amplification can be expected. At each natural frequency, a standing wave develops in the soil. Normalized deformed shapes, or mode shapes, for the first three natural frequencies are shown in figure (*Fig.2.22*).
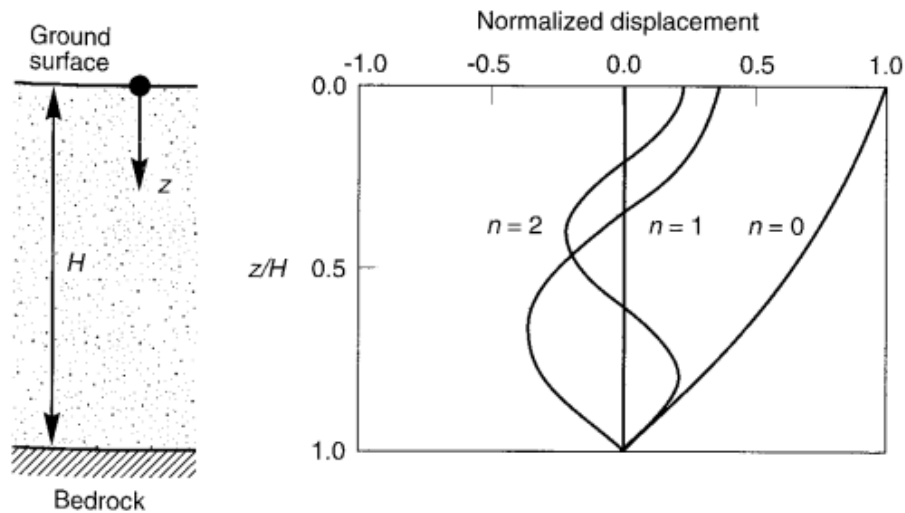
Figure 2.22 - *Displacement patterns for standing waves at fundamental (n=0), second (n=1) and third (n=2) natural frequencies for a soil layer with ξ=5%. Displacements are normalized by maximum displacement at the fundamental frequency.(Kramer, 1996)*

Note that the soil displacements are in phase at all depths in the fundamental mode, but not in the higher modes.

2.3.3 Rayleigh damping

Rayleigh damping was originally used in the analysis of structures and elastic continua to damp the natural oscillation modes of the system. The equations, therefore, are expressed in matrix form. A damping matrix, C, is used, with components proportional to the mass (M) and stiffness (K) matrices:

$$C = \alpha M + \beta K$$

where:

$\boldsymbol{\alpha}$ is the mass-proportional damping constant;

$\boldsymbol{\beta}$ is the stiffness-proportional damping constant.

For a multiple degrees-of-freedom system, the critical damping ratio, ξ_i, at any angular frequency of the system, ω_i, can be found from (*Bathe and Wilson 1976*)

$$\alpha + \beta \omega_i^2 = 2\omega_i \xi_i$$

or

$$\xi_i = \frac{1}{2}\left(\frac{\alpha}{\omega_i} + \beta \omega_i\right)$$

The critical damping ratio ξ_i, is also known as the fraction of critical damping for mode i with angular frequency ω_i. The variation of the normalized critical damping ratio with angular frequency, ω_i, is shown in figure (*Fig.2.23*).
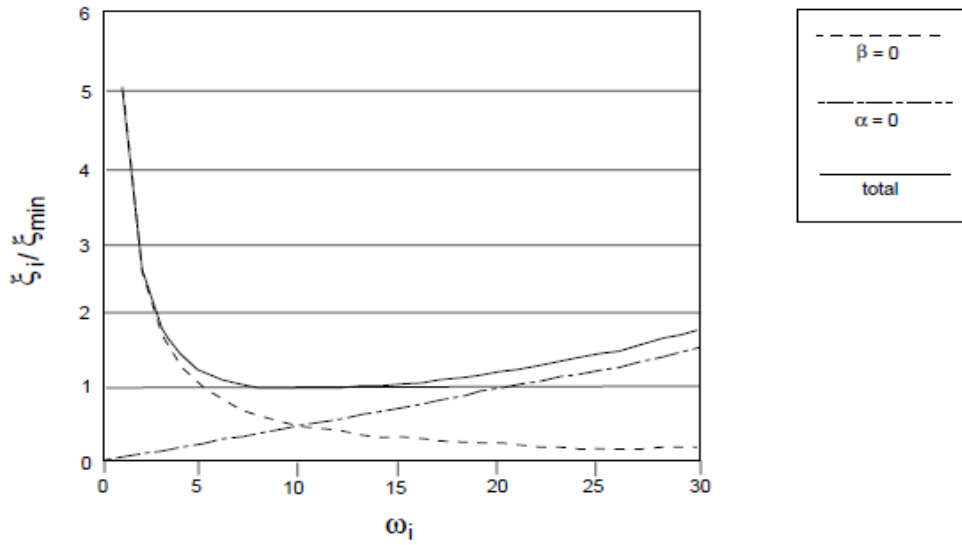
Fig 2.23 - *Variation of normalized critical damping ratio with angular frequency.*
(FLAC³ᴰ Manual)

Three curves are given: mass and stiffness components only; and the sum of both components. As shown, mass-proportional damping is dominant at lower angular-frequency ranges, while stiffness-proportional damping dominates at higher angular frequencies. The curve representing the sum of both components reaches a minimum at:

$$\xi_{min} = (\alpha\beta)^{\frac{1}{2}}$$

$$\omega_{min} = \left(\frac{\alpha}{\beta}\right)^{\frac{1}{2}}$$

or:

$$\alpha = \xi_{min}\,\omega_{min}$$

$$\beta = \frac{\xi_{min}}{\omega_{min}}$$

The centre frequency is then defined as

$$f_{min} = \frac{\omega_{min}}{2\pi}$$

It may be noted that at frequency ω_{min} (or f_{min}) and only at that frequency, mass damping and stiffness damping each supply half of the total damping force. Rayleigh damping is specified in FLAC[3D] with the parameters f_{min} in *Hertz* and ξ_{min}. (*FLAC[3D] Manual*).

2.3.4 Comparison between analytical solution and FLAC[3D] solution

Considering the analytical solution of *uniform, damped soil on rigid rock*, it is investing to check FLAC[3D] results and compare the two solutions that is, the analytical one and FLAC[3D]. The geometry of the model (*Fig 2.24*) for FLAC[3D] analysis is the same that described in the first part of the chapter.
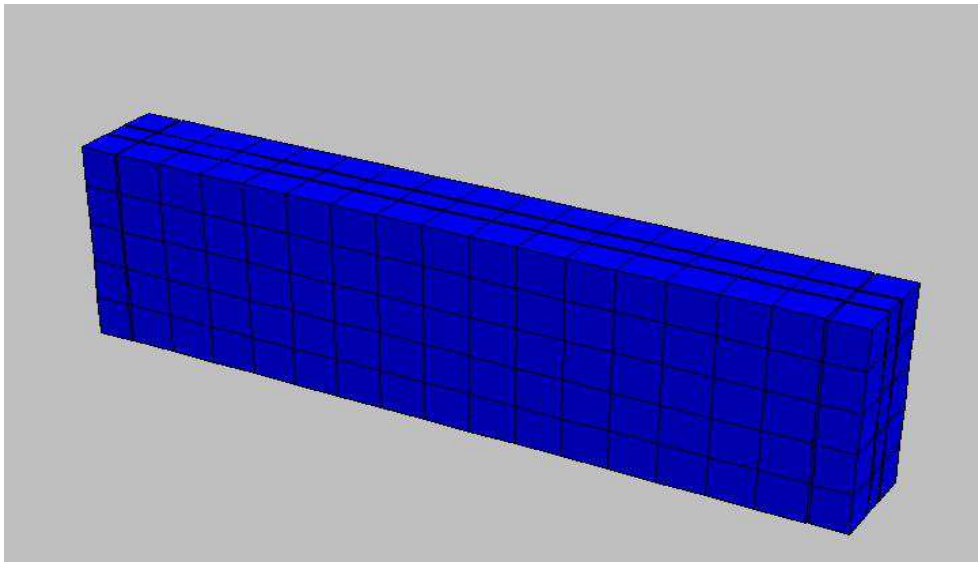
Figure 2.24 *- Geometry of the model with free field boundary conditions.*

The material properties are:

Model: Elastic

Properties: Bulk   modulus   (K) $= 2 \cdot 10^6 \; kPa$

                    Shear   modulus   (G) $= 0{,}4 \cdot 10^5 \; kPa$

                    Density   (ρ) $= 2 \cdot 10^3 \; \frac{kg}{m^3}$

The boundary condition adopted is free field boundary conditions, and Rayleigh damping is chosen.

2.3.4.1   FLAC³ᴰ solution

The input for Rayleigh damping in FLAC³ᴰ are:

$$\xi_{min} = 0,05$$

$$f_{min} = 7,07 \text{ Hz}$$

In this case f_{min} is taken with the same value of the average between the first and second natural frequencies of the system:

$$\omega_n = \frac{v_s}{H}\left(\frac{\pi}{2} + n\pi\right)$$

$$v_s = \sqrt{\frac{G}{\rho}} = \sqrt{\frac{40000}{2}} = \sqrt{20000} = 141,42 \ \frac{m}{s}$$

$$\omega_1 = \frac{v_s}{H}\left(\frac{\pi}{2}\right) = \frac{141,42}{10}\frac{\pi}{2} = 22,21 \ \frac{rad}{s}$$

$$\omega_2 = \frac{v_s}{H}\left(\frac{\pi}{2} + \pi\right) = \frac{141,42}{10}\left(\frac{\pi}{2} + \pi\right) = 66,63 \ \frac{rad}{s}$$

$$f_1 = \frac{\omega_1}{2\pi} = \frac{22,21}{2\pi} = 3,53 \ Hz$$

$$f_2 = \frac{\omega_2}{2\pi} = \frac{66,63}{2\pi} = 10,60 \ Hz$$

$$f_{min} = \frac{f_1 + f_2}{2} = \frac{3,53 + 10,60}{2} = 7,07 Hz$$

$$\omega_{min} = 2\pi f_{min} = 2 \cdot \pi \cdot 7,07 = 44,42 \ \frac{rad}{s}$$

The analysis was repeated for a number of frequencies from 0,5 *Hz* to 12,5 *Hz* and some results are showing in *Figure 2.25* to *2.28*.
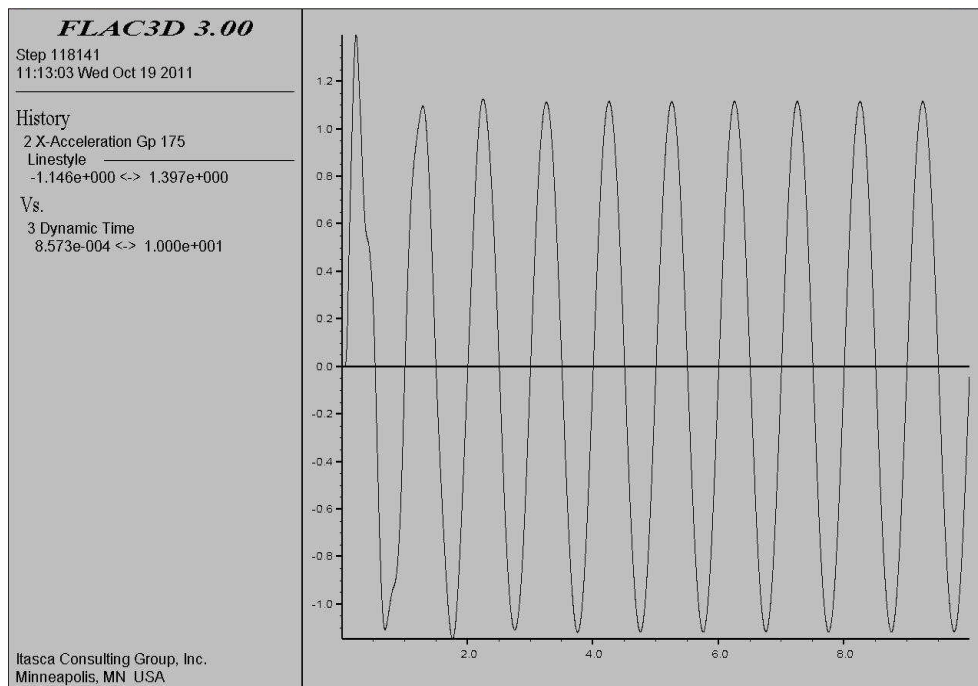
Figure 2.25 - *Graphic x-acceleration/dynamic time. The frequency of the input wave is*

1,0 Hz.
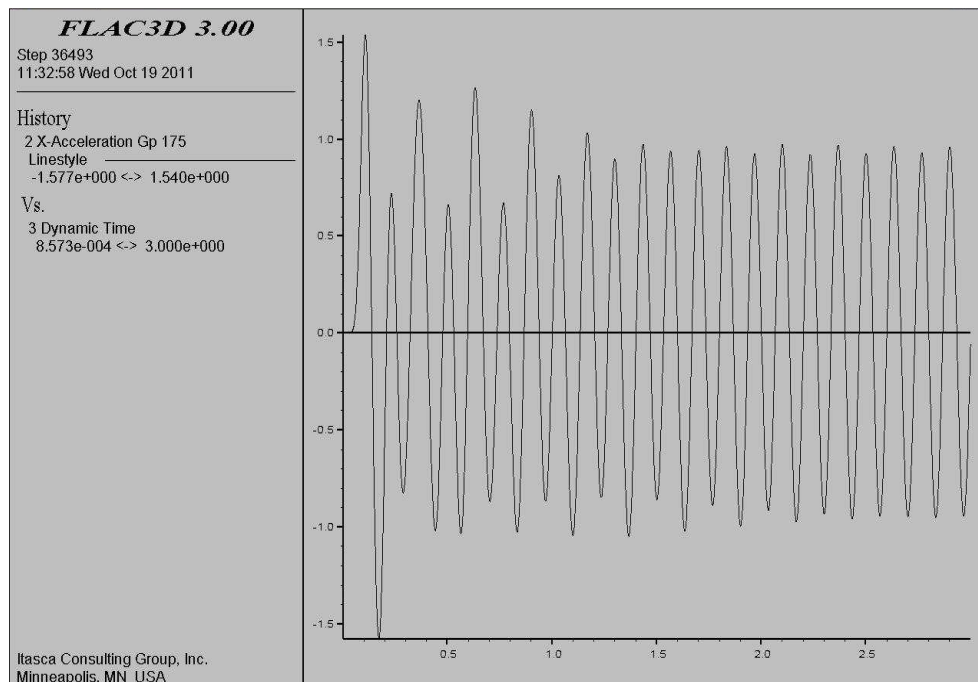
Figure 2.26 - *Graphic x-acceleration/dynamic time. The frequency of the input wave is*

7,5 Hz.
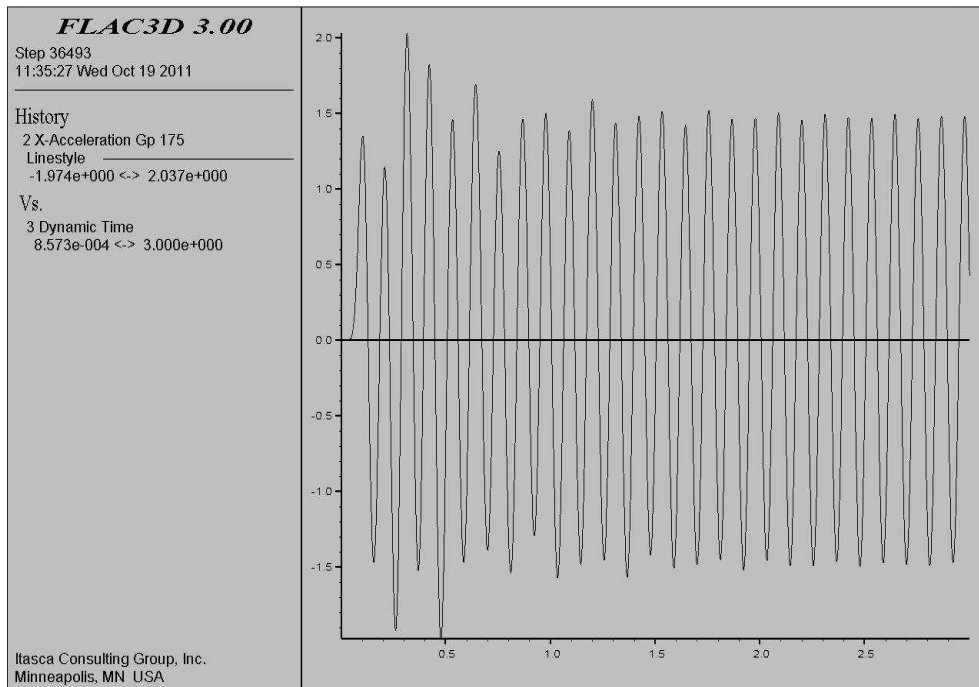
Figure 2.27 - *Graphic x-acceleration/dynamic time. The frequency of the input wave is 9,0 Hz.*
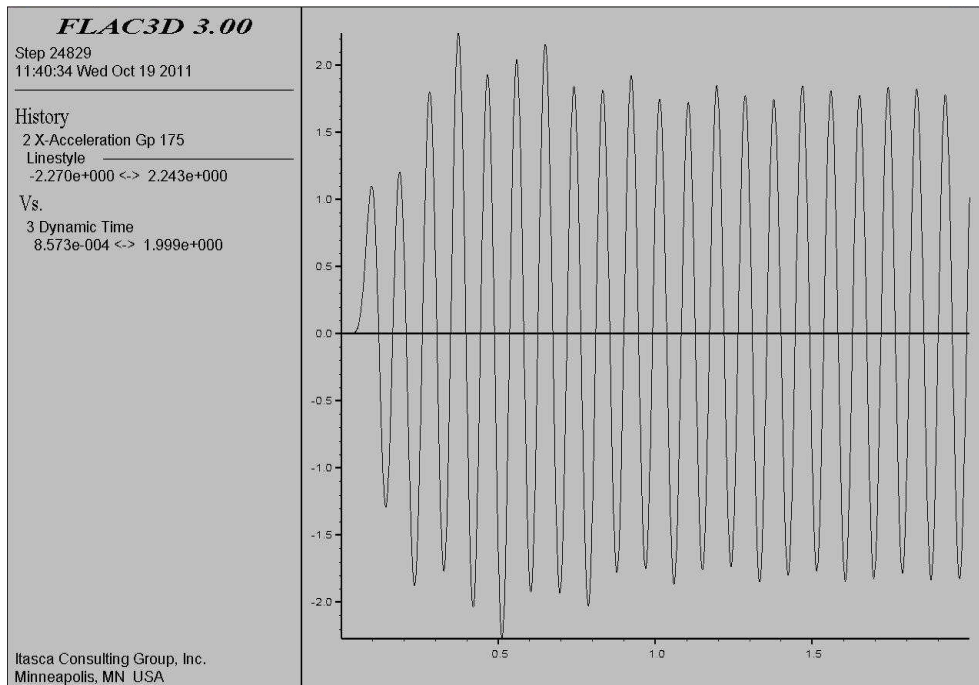
Figure 2.28 - *Graphic x-acceleration/dynamic time. The frequency of the input wave is 11,0 Hz.*

For each frequency the last part of the response, which represents the steady-state response, is used and the maximum value of *x*-acceleration is taken (*Fig.2.29*). Then these values are plotted in a graph as a function of frequency (*fig.2.30*).
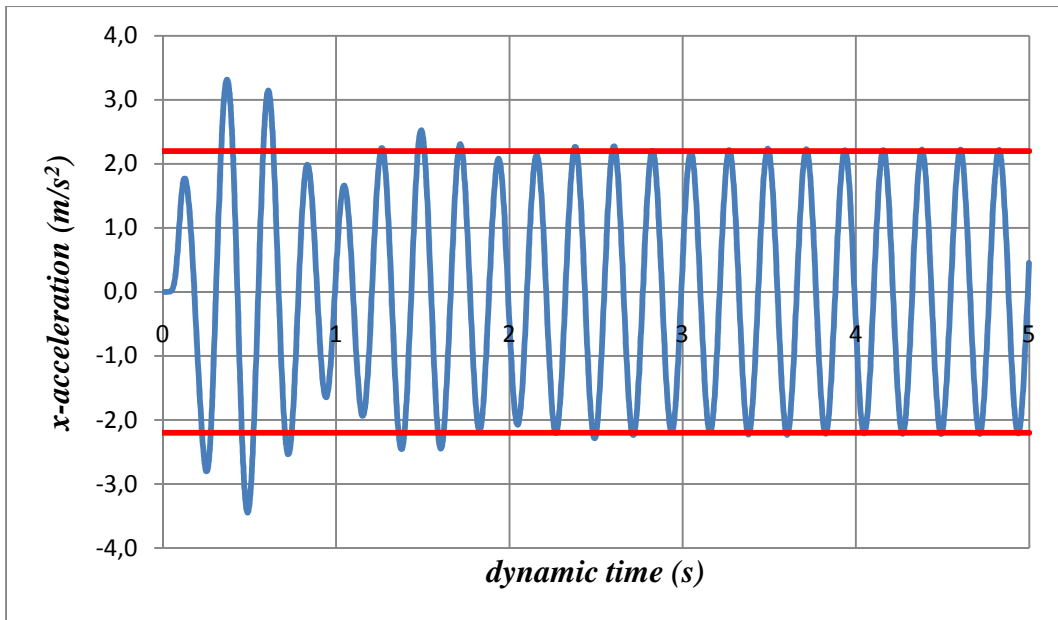
Figure 2.29 *– Value of x-acceleration considered.*
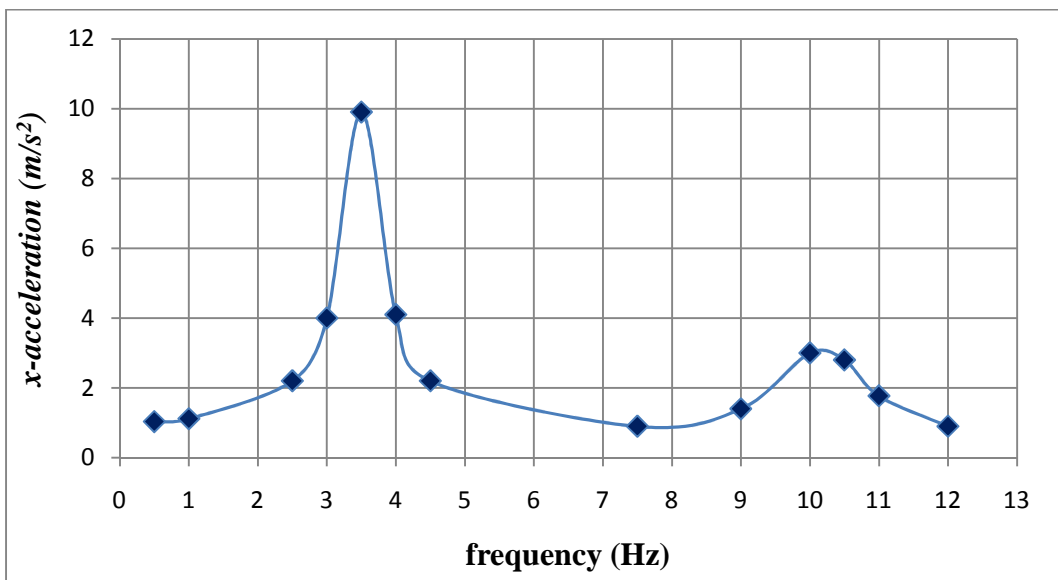
Figure 2.30 *- FLAC^{3D} solutions.*

2.3.4.2   Analytical solution

From the input value for the Rayleigh damping the two parameters α and β are calculated as:

$$\alpha = \xi_{min}\,\omega_{min} = 0{,}05 \cdot 44{,}42 = 2{,}22$$

$$\beta = \frac{\xi_{min}}{\omega_{min}} = \frac{0{,}05}{44{,}42} = 0{,}001$$

The critical damping ratio ξ_i for each frequency is:

$$\xi_i = \frac{1}{2}\left(\frac{\alpha}{\omega_i} + \beta\omega_i\right)$$

For each frequency, the damping ratio is computed according to the above equation and plotted in *Figure 2.31*.
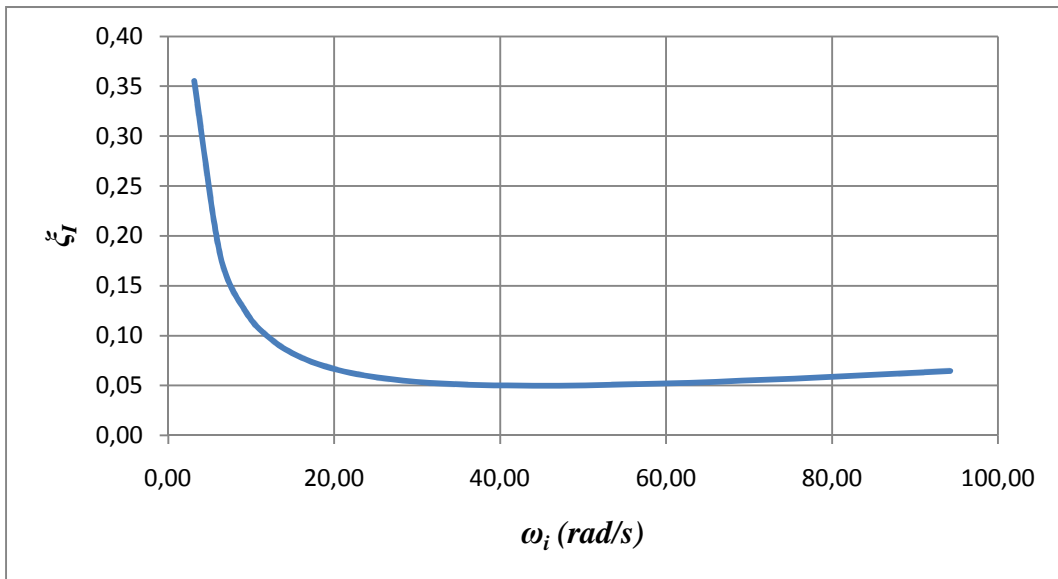
Figure 2.31 *- Graphic of damping ratio in function of angular frequency.*

The amplification function is:

$$|F(\omega_i)| = \frac{1}{\sqrt{\cos^2\left(\frac{\omega_i H}{v_s}\right) + \left[\xi_i\left(\frac{\omega_i H}{v_s}\right)\right]^2}}$$

The values of amplification function are calculated for every frequency with the corresponding damping and are plotted in *Figure 2.32*.
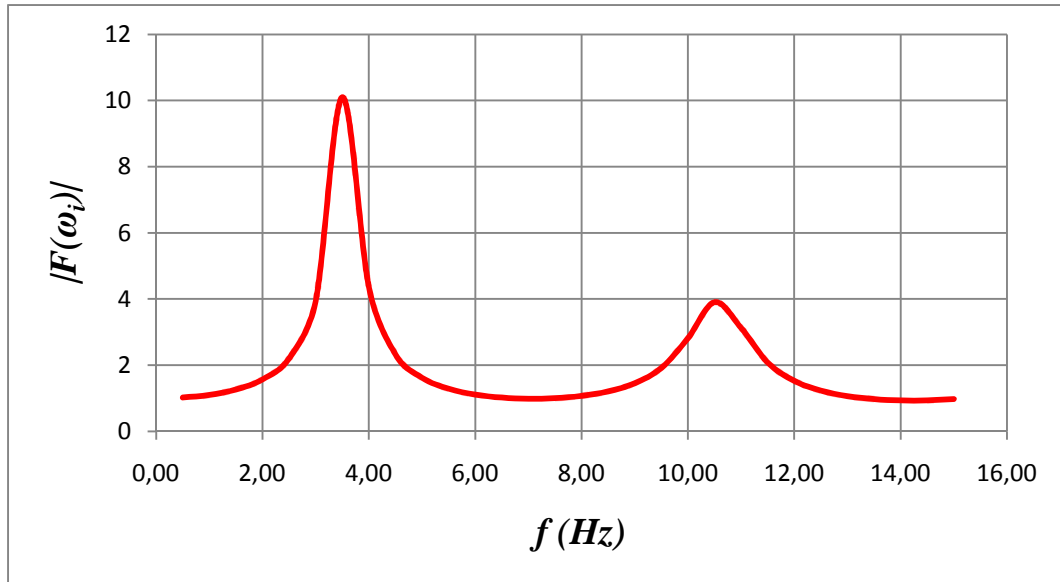
Figure 2.32 – Graphic of analytical solution

2.3.4.3 Comparison between the two solutions

The results of FLAC[3D] are compared in *Figure 2.33* with the analytical solution.
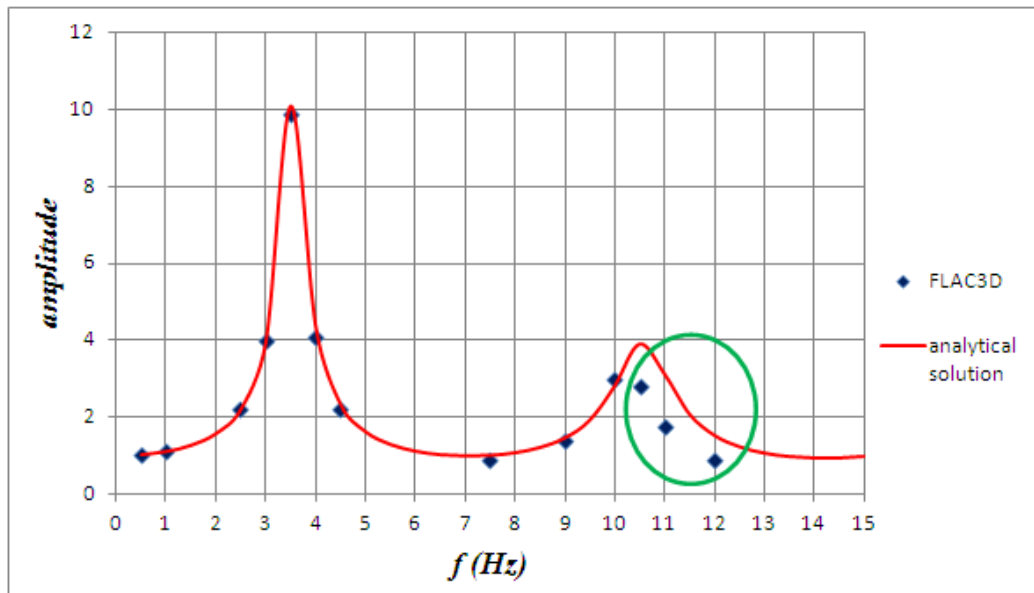
Figure 2.33 – Comparison between FLAC[3D] solution and analytical solution.

It was considered that part of the discrepancies at high frequencies was due to the mesh size. Therefore, a new model (*Fig 2.34*), with the same geometry and the same material properties but with a more fine mesh, is adopted. The results are plotted together with previous results in *Figure 2.35*.
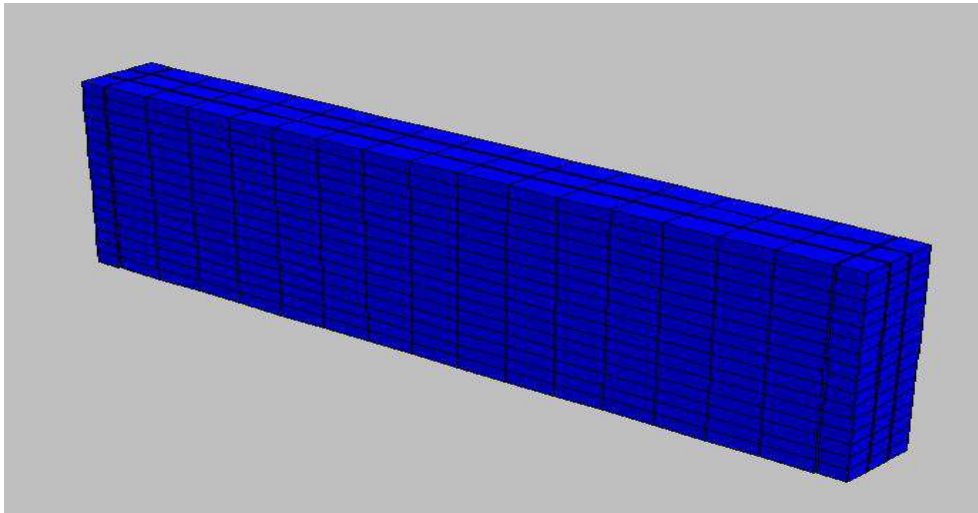
Figure 2.34 - *Geometry of the model*
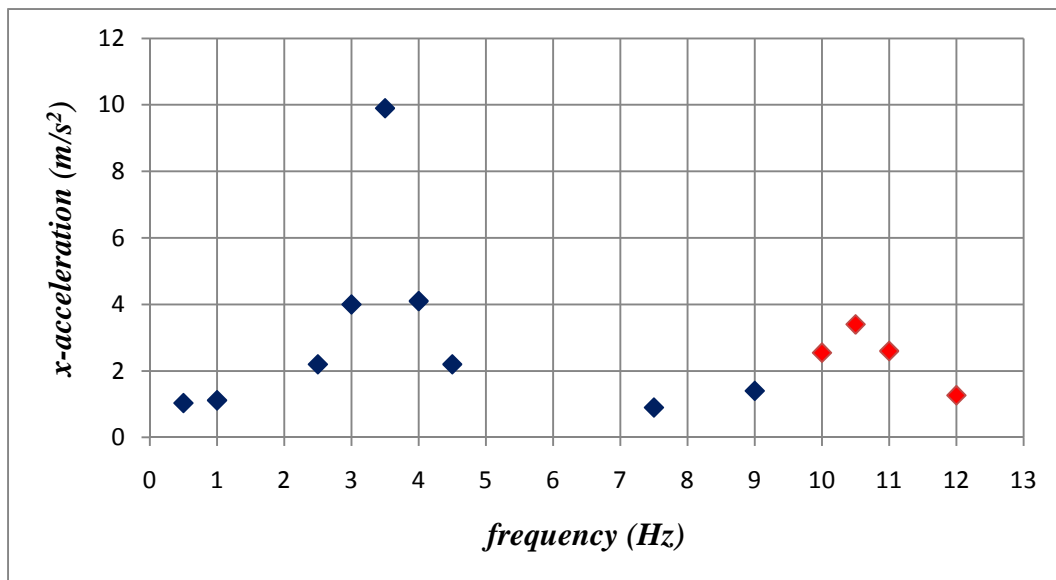
Figure 2.35 - *FLAC³ᴰ results. In red the values of the results obtained with the new mesh.*
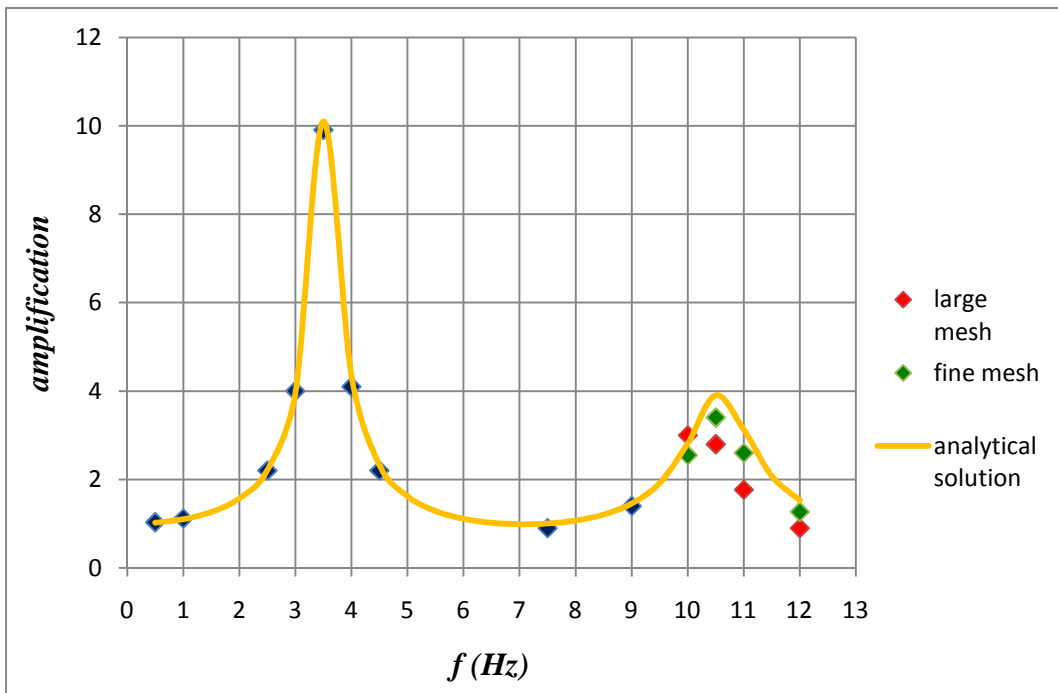
Figure 2.36 - *Comparison between analytical solution and FLAC³ᴰ solution in the two cases: with large mesh and with fine mesh.*
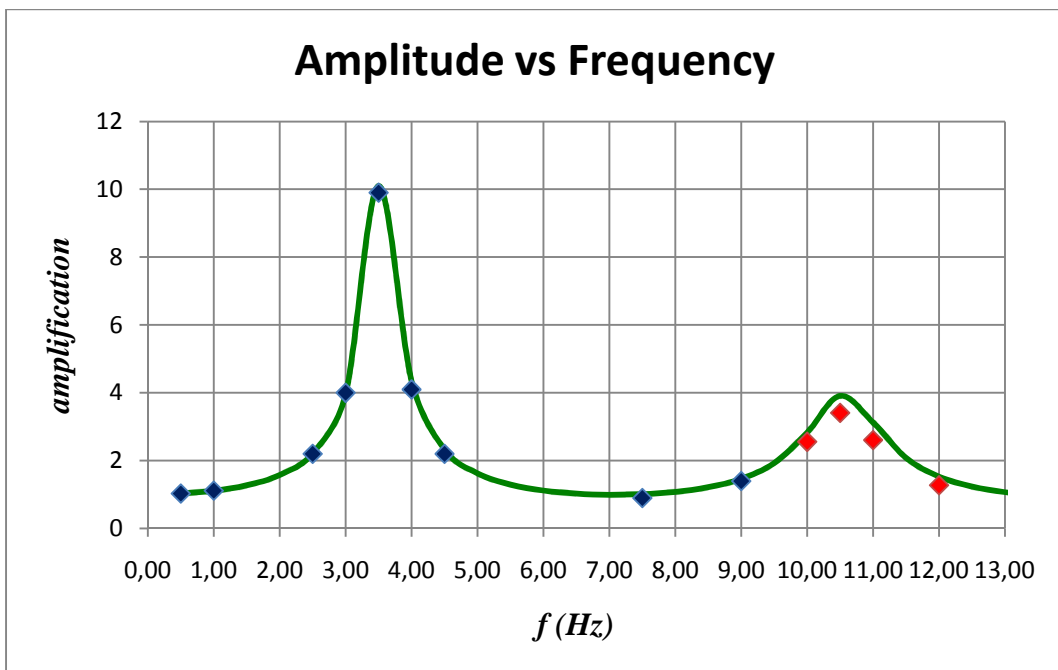
Figure 2.37 – *Comparison between FLAC³ᴰ solution and analytical solution.*

Figure 2.37 shows the comparison based on the new data. Now with a more fine mesh, the two solutions are very similar. Especially refining the mesh in z-direction is possible to observe a better correspondence between the solutions.

Chapter 3 – Influence of free field boundary conditions

The goal of this chapter is to study the performance of the free field boundary condition in slope analyses. A model of a simple slope is constructed and it is subjected to a dynamic load. Then at the sides of the model will be extended, in this way the boundary conditions are more distant from the slope. Three models will be created with different extensions and for each a dynamic analysis will be made. To study the result and the influence of the boundary conditions some monitoring points will be take on the top of the model and the *x*-acceleration will be registered. The results will be presented in summary plots for comparison.

3.1 Model 1 - no extension

A simple slope is created (*Fig. 3.1*) and a dynamic analysis is made at different frequencies ranging from 0,6 Hz to 3,6 Hz. The dynamic input is a simple sinusoidal wave:

$$a(t) = \sin(\omega t)$$

In this first model five monitoring points (A, B, C, D, E) have been taken on top of the model, in which the values of the *x*-acceleration are measured (*Fig 3.2*)
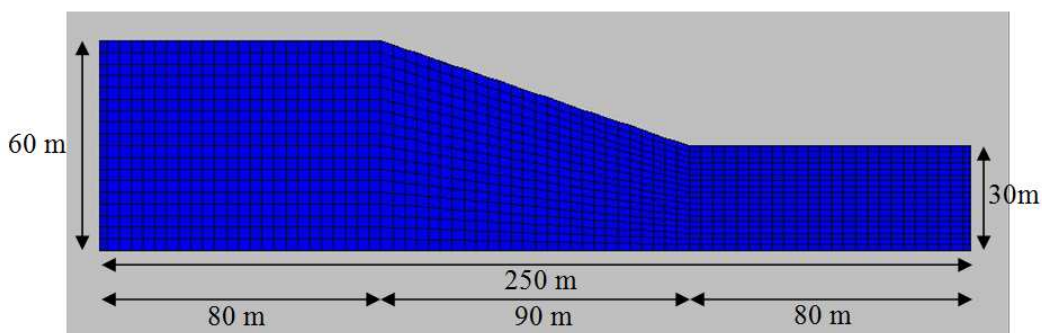
Figure 3.1 - *Geometry of the model*

The material parameters are:

Model: Elastic

With the following properties:

Bulk   modulus   (K) $= 2 \cdot 10^6 \ kPa$

Shear   modulus   (G) $= 0{,}4 \cdot 10^5 \ kPa$

Density   (ρ) $= 2 \cdot 10^3 \ \frac{kg}{m^3}$

The model is discretized using 72 elements in *x*-direction, 1 element in *y*-direction and 18 elements in *z*-direction. Even though a 3D model is used, the analysis represents a plane strain case because of the size of the model in the *y-direction*. The zone length is smaller than 1/10 of the shortest wavelength (on the basis of elastic proprieties of the material and the input frequency) to provide accurate wave transmission.

$$\Delta l \leq \frac{\lambda}{10}$$

$$\lambda = \frac{v_s}{f_{max}}$$

$$v_s = \sqrt{\frac{G}{\rho}} = \sqrt{\frac{40000}{2}} = \sqrt{20000} = 141{,}42 \, \frac{m}{s}$$

On the left side the height of the model is 60 *m* so the first natural frequency is:

$$f_l = \frac{v_s}{4 \cdot H} = \frac{141{,}42}{4 \cdot 60} = 0{,}6 \ Hz$$

On the right side the height is 30 *m* so the first natural frequency on that side is:

$$f_r = \frac{v_s}{4 \cdot H} = \frac{141{,}42}{4 \cdot 30} = 1{,}2 \ Hz$$

The range of frequency considered for the analyses vary between 0,6 Hz and three times the frequency of the right side that is 3,6 Hz. As f_{max} is taken 4Hz:

$$f_{max} = 4.0 \; Hz$$

$$\lambda = \frac{v_s}{f_{max}} = \frac{141.42}{4} = 35.3 \; m$$

$$\Delta l \leq \frac{\lambda}{10} \leq \frac{35.3}{10} = 3.53 \; m$$

Whereby in *x*-direction (*250m*) there must be at least 71 elements, in *y*-direction (*1m*) at least 1 element and in the *z*-direction, considering the highest side (left side: 60 *m*), 17 elements.
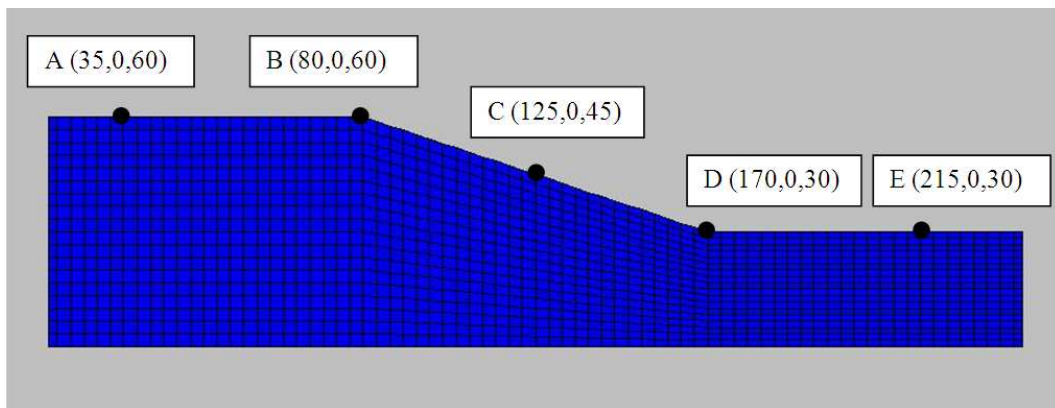
Figure 3.2 – Position of the monitoring points.

The steady-state accelerations, as for the frequencies, for the monitoring points *A-E* are plotted in *Figures 3.3* to *3.7*. Because the input acceleration on the base is $1\frac{m}{s^2}$, these plots can also be considered as transfer function.
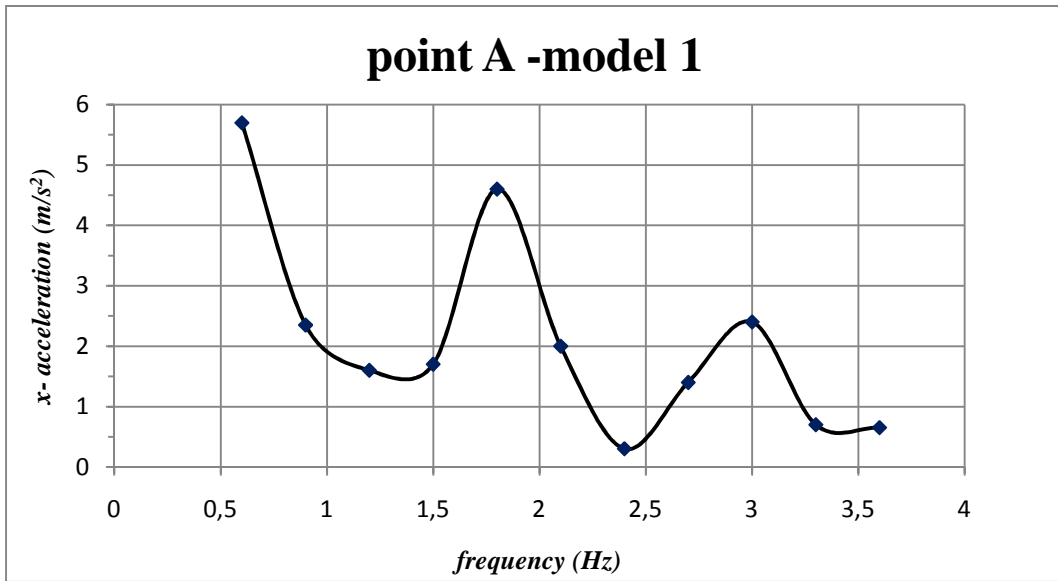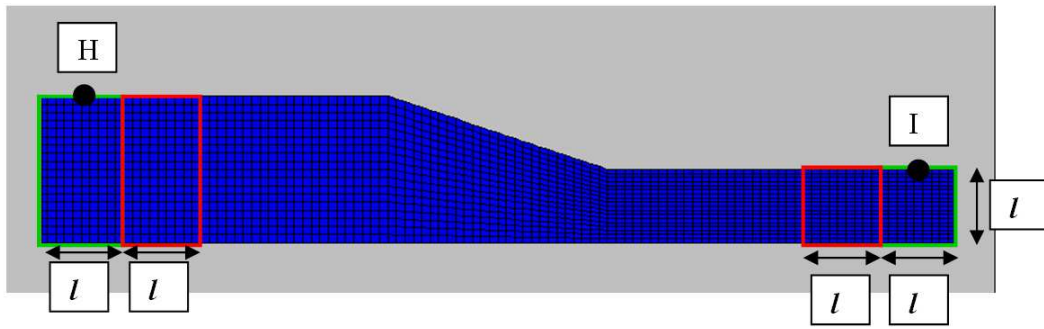
Figure 3.3 *– Steady-state acceleration for monitoring point A.*
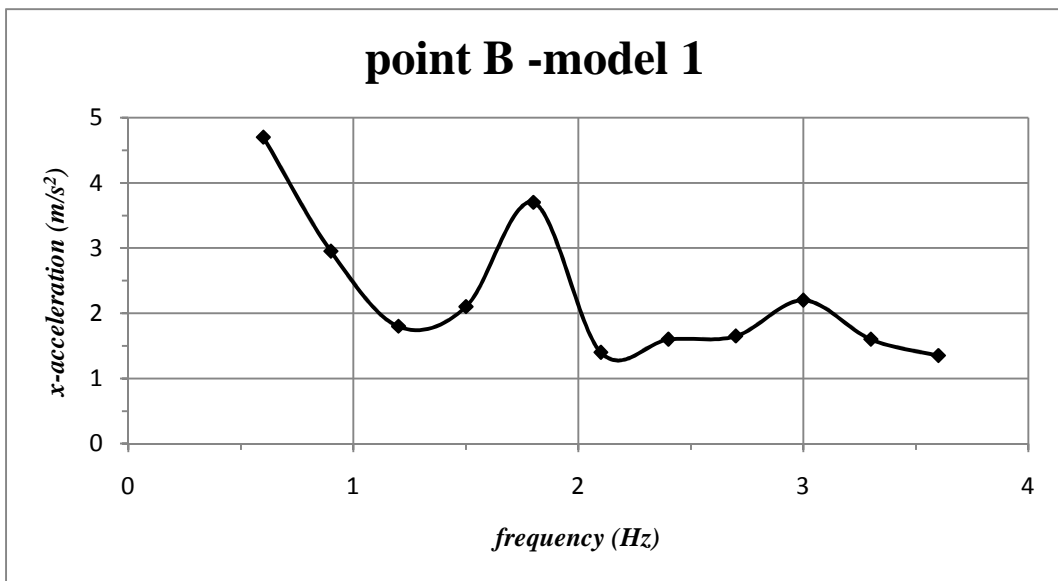
Figure 3.4 *– Steady-state acceleration for monitoring point B.*
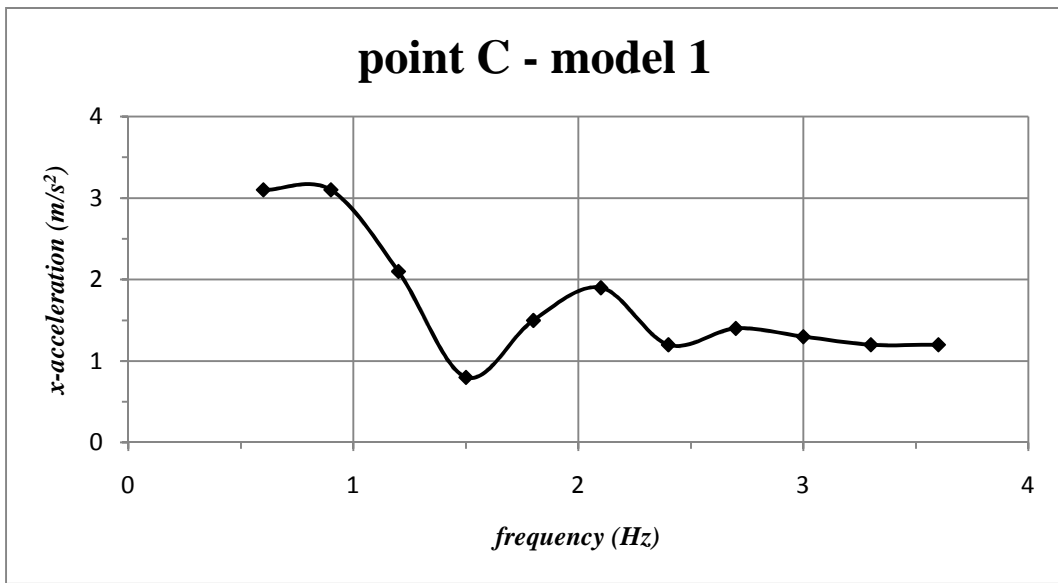
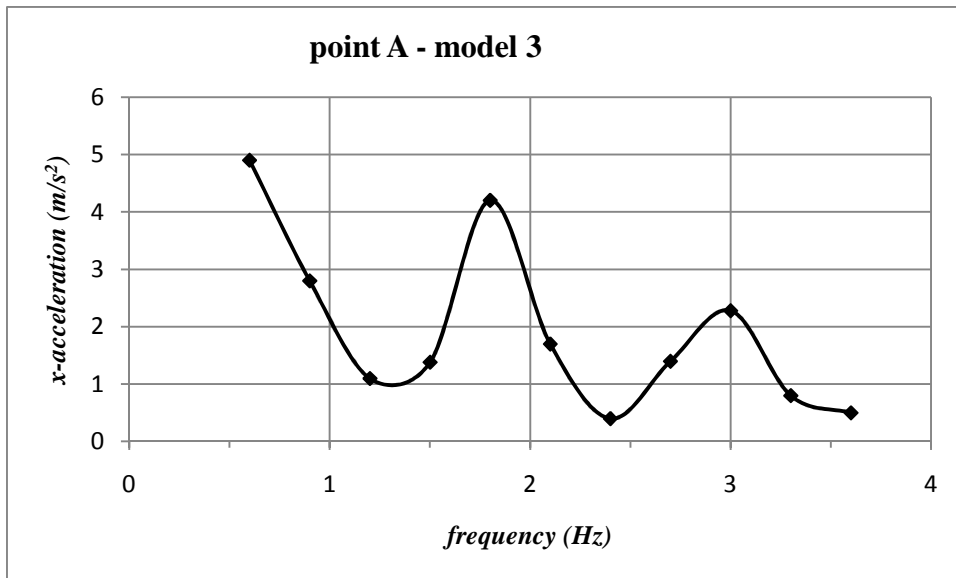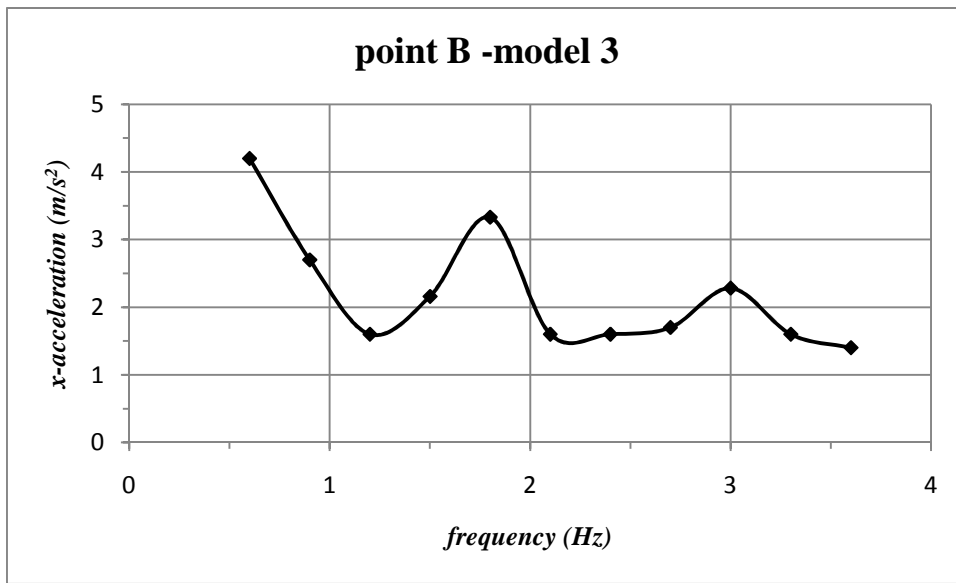***Figure 3.5** – Steady-state acceleration for monitoring point C.*
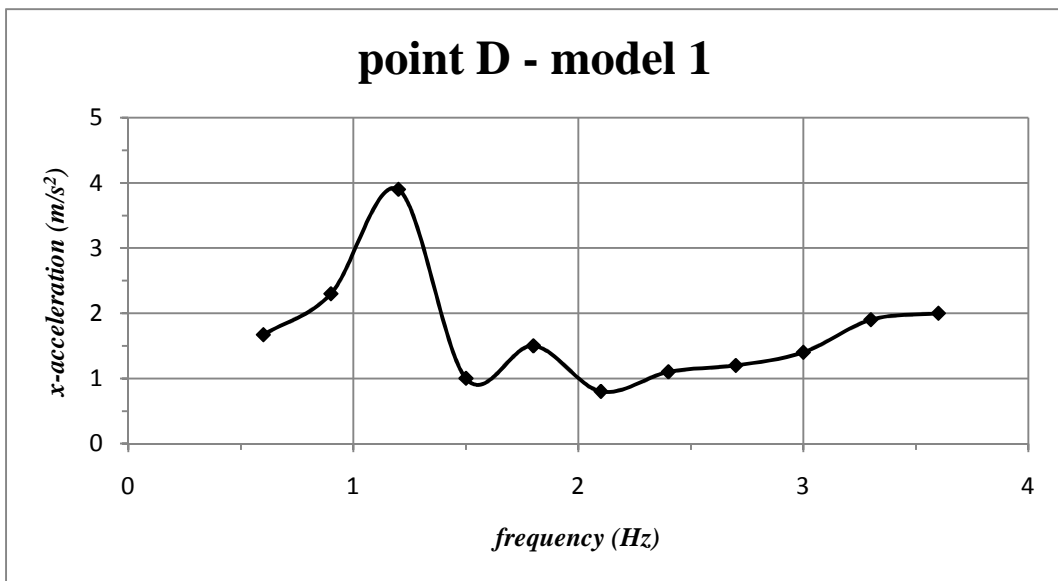
***Figure 3.6** – Steady-state acceleration for monitoring point D.*
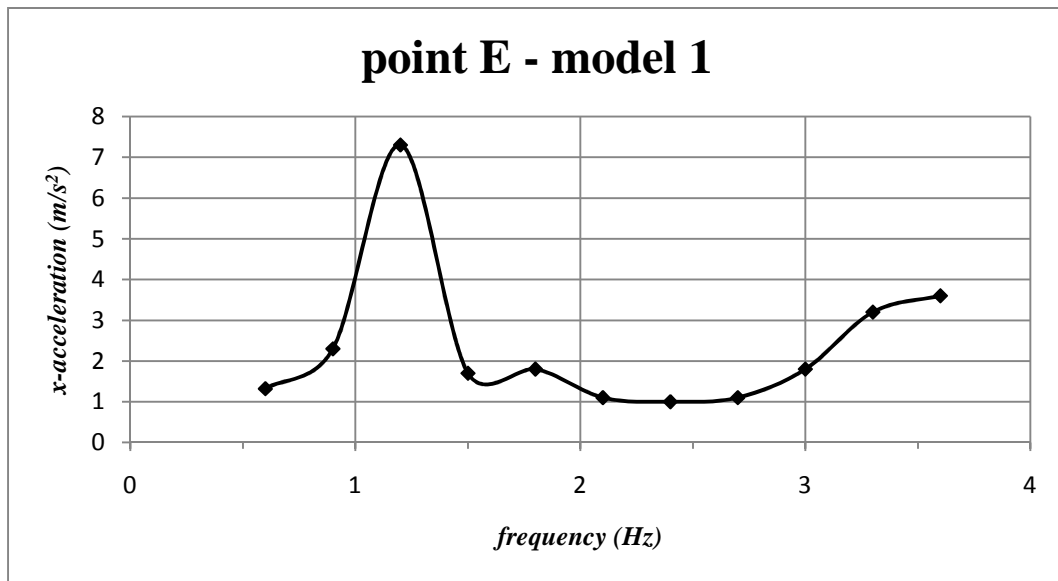
Figure 3.7 – *Steady-state acceleration for monitoring point E.*

3.2   Model 2 - one extension

In this analysis, the model is extended at its sides (*Fig. 3.8, 3.9*), so that the boundary conditions are farther away from the slope. Two extra monitoring points (F,G) (*Fig. 3.8*) are added on the extensions and a new dynamic analysis is run. The same element size was used.
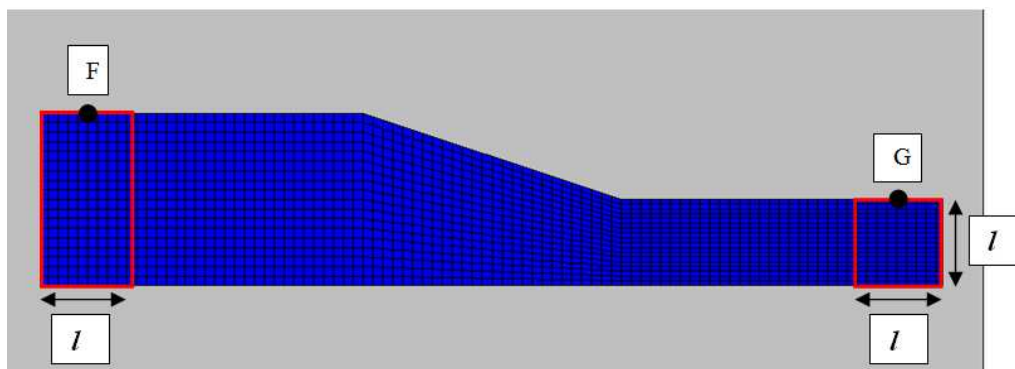
Figure 3.8 - *Geometry of the model with the extension on the two sides and position of the two new monitoring points F and G.*
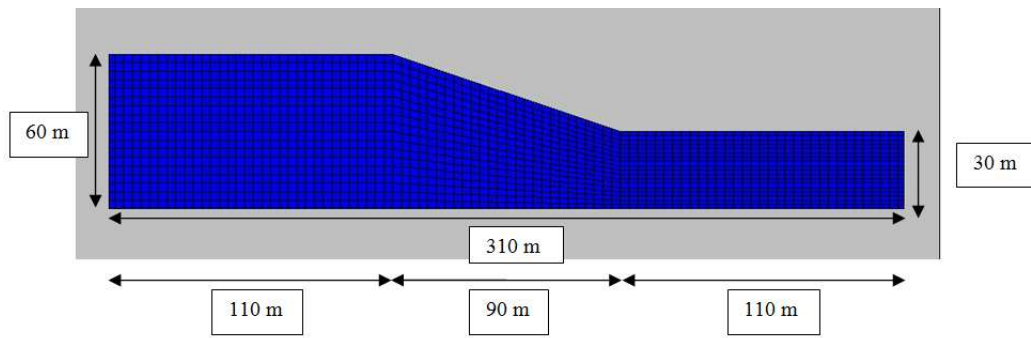
Figure 3.9 - *Geometry of the model*

The steady-state accelerations, as for the frequencies, for the monitoring points A-G are plotted in *Figures 3.10* to *3.16*.
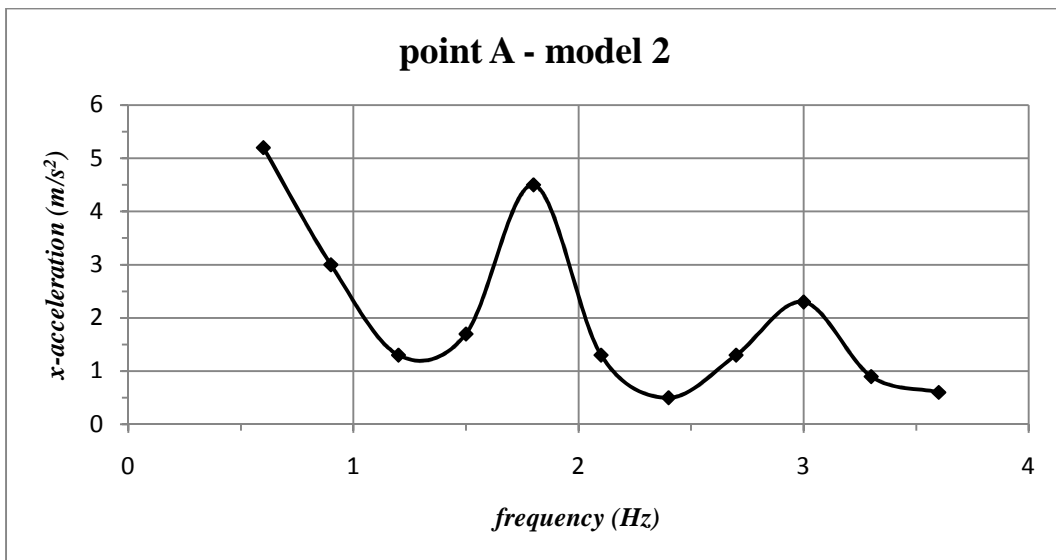
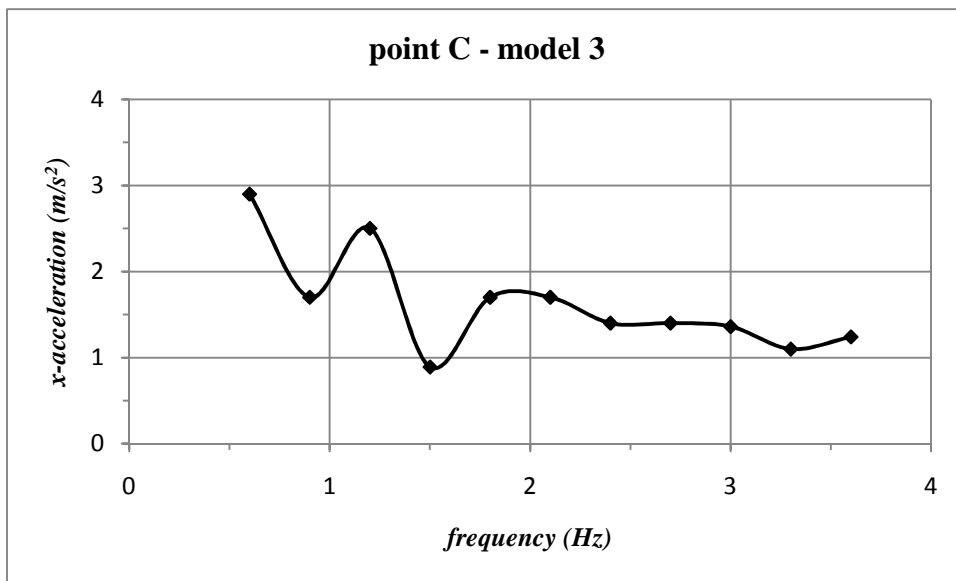**Figure 3.10 –** *Steady-state acceleration for monitoring point A.*
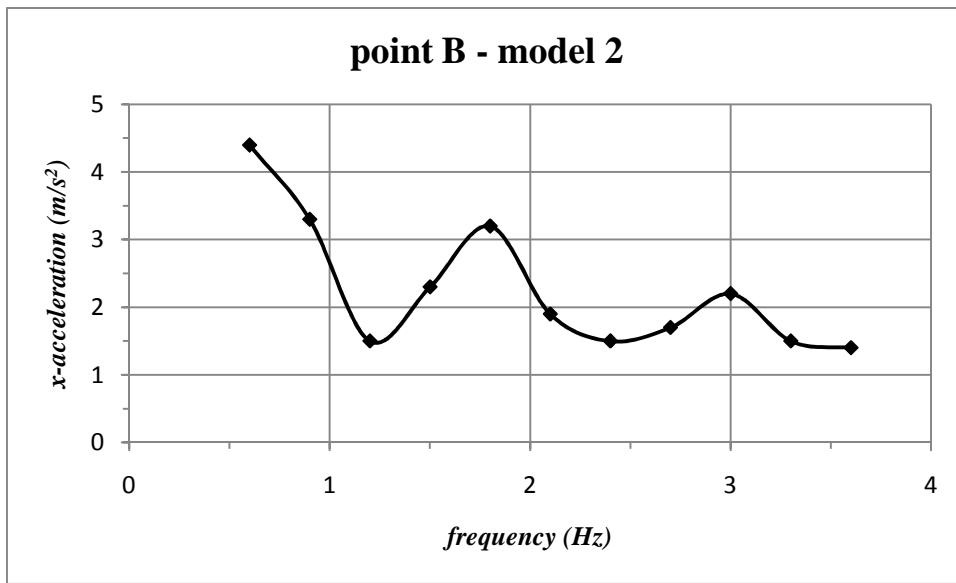
Figure 3.11 – *Steady-state acceleration for monitoring point B.*
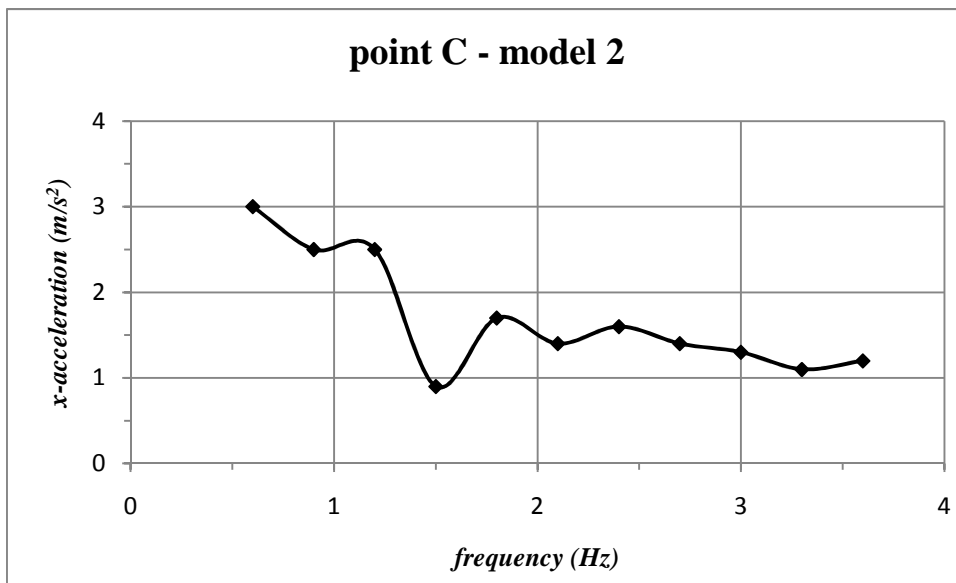
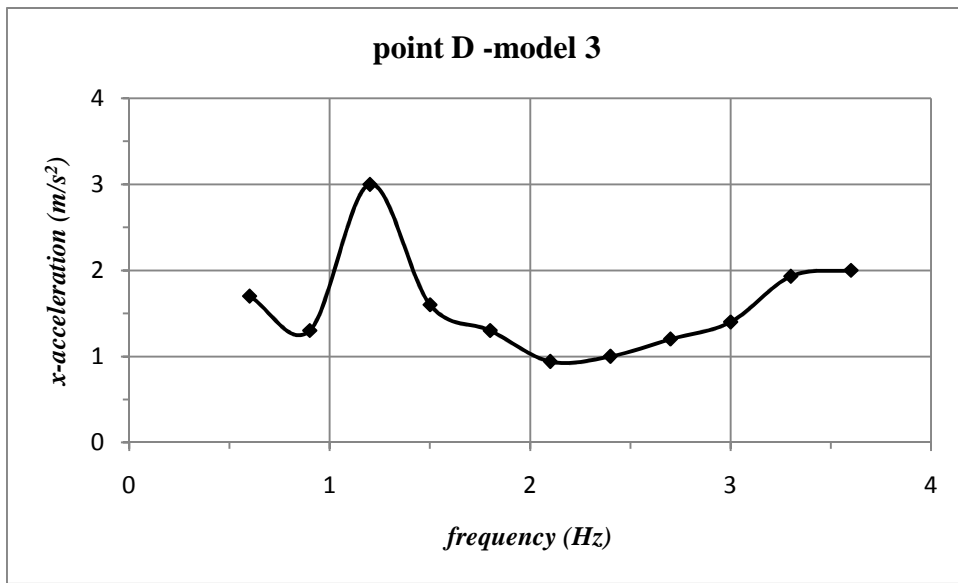**Figure 3.12** – *Steady-state acceleration for monitoring point C.*
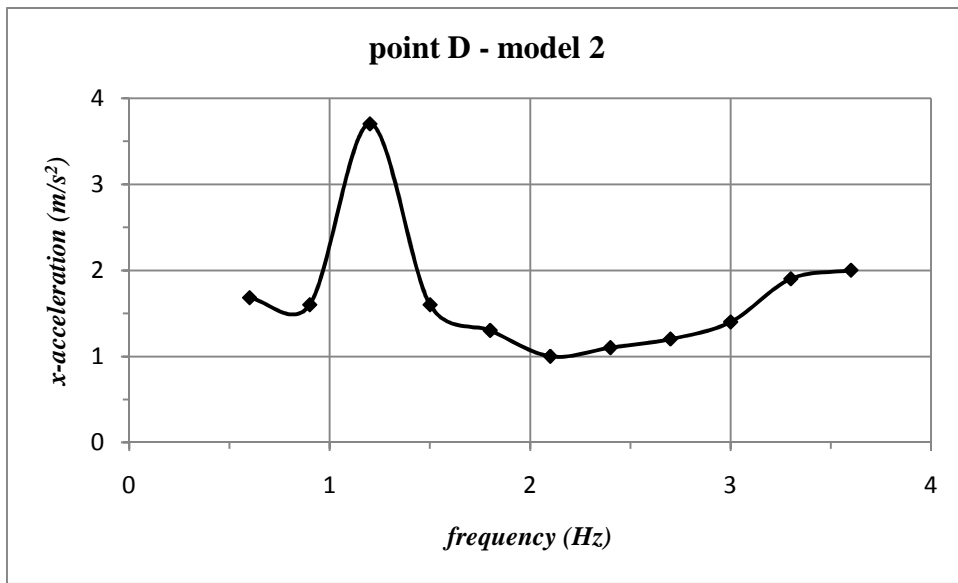
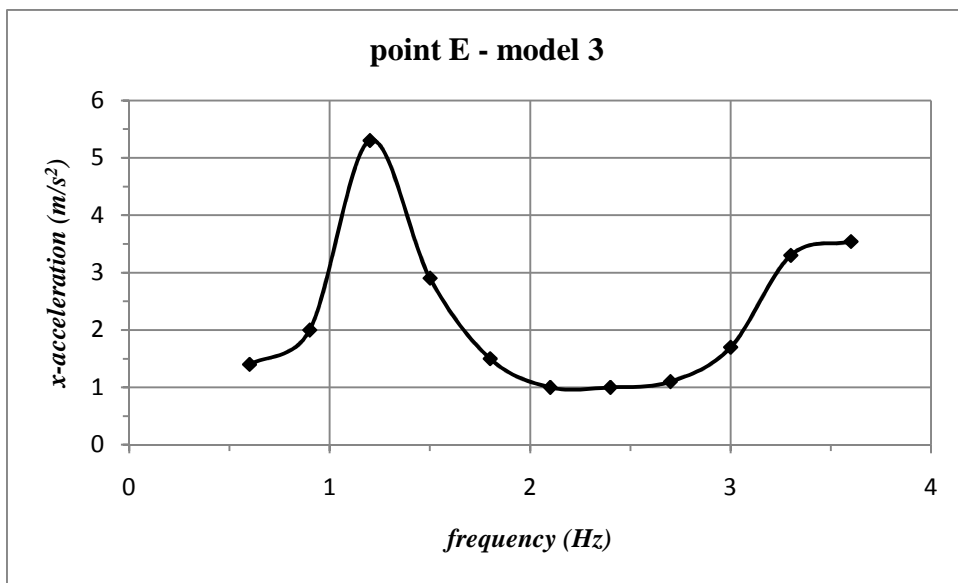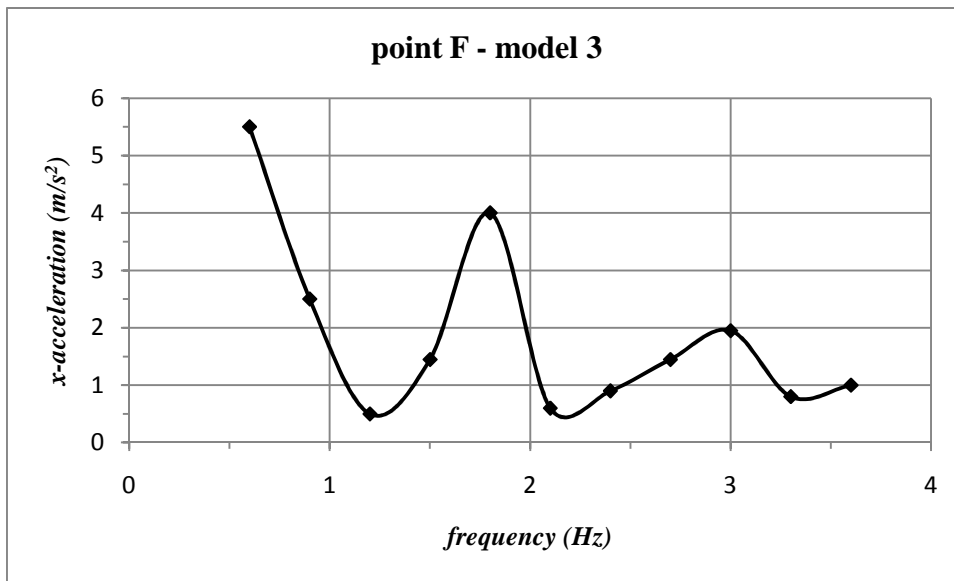**Figure 3.13** – *Steady-state acceleration for monitoring point D.*
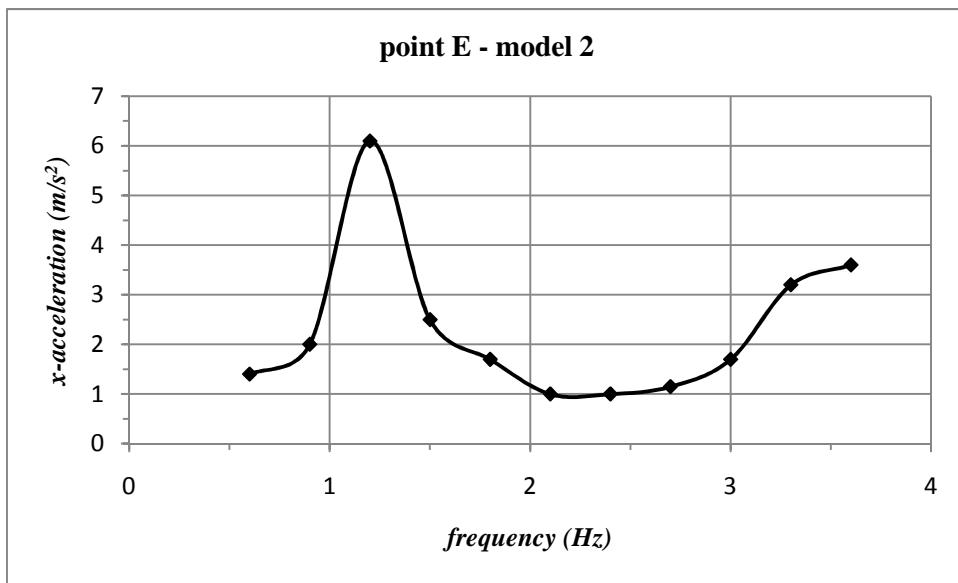
Figure 3.14 – *Steady-state acceleration for monitoring point E.*
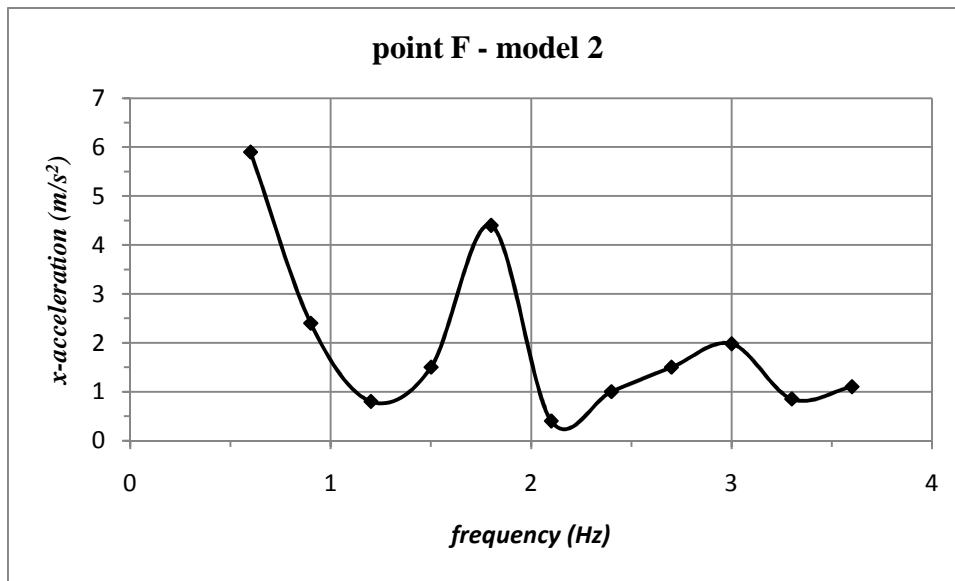
Figure 3.15 – *Steady-state acceleration for monitoring point F.*
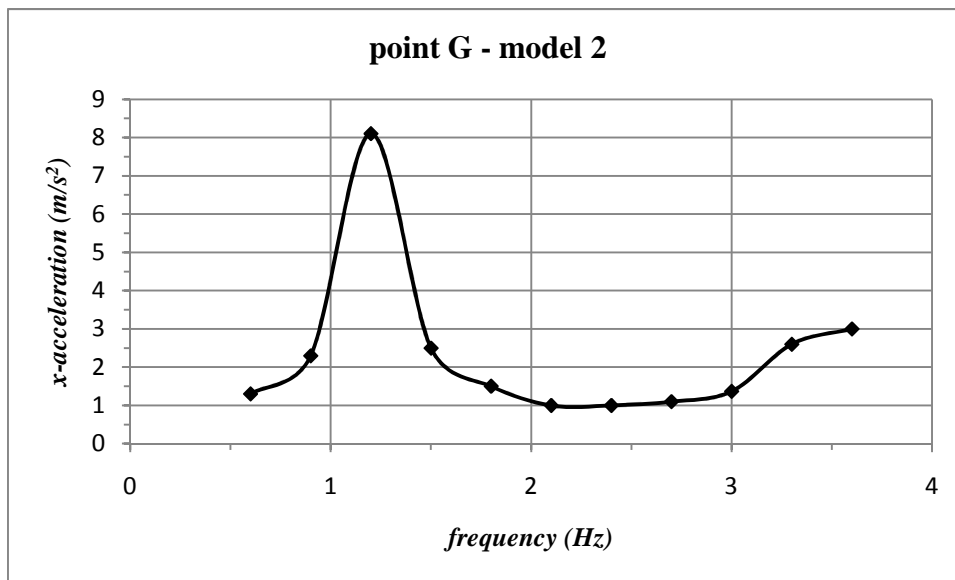
Figure 3.16 – *Steady-state acceleration for monitoring point G.*

3.3   Model 3 - two extensions

In this analysis, the model is extended again at its (*Fig. 3.17, 3.18*), so that the boundary conditions are farther away from the slope. Other two monitoring points (H, I) are added on the new extensions and a dynamic analysis is run. The same element size was used. The steady-state accelerations, as for the frequencies, for the monitoring points A-G are plotted in Figures 3.19 to 3.27.

Figure 3.17 *- Geometry of the model with the extension on the two sides and position of the two new monitoring points H and I.*
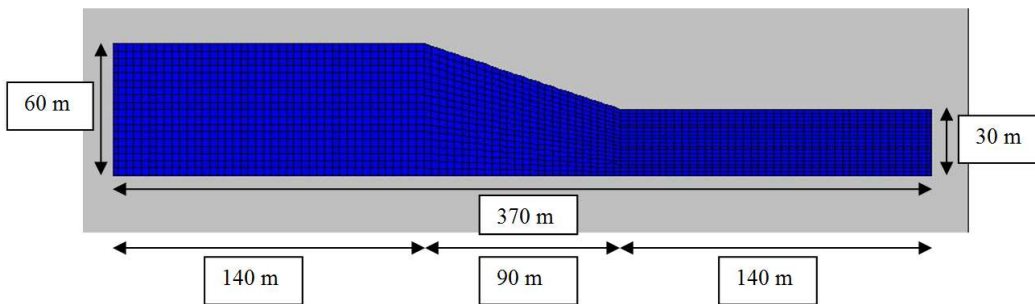
Figure 3.18 *- Geometry of the model*

Figure 3.19 *– Steady-state acceleration for monitoring point A.*

Figure 3.20 *– Steady-state acceleration for monitoring point B.*

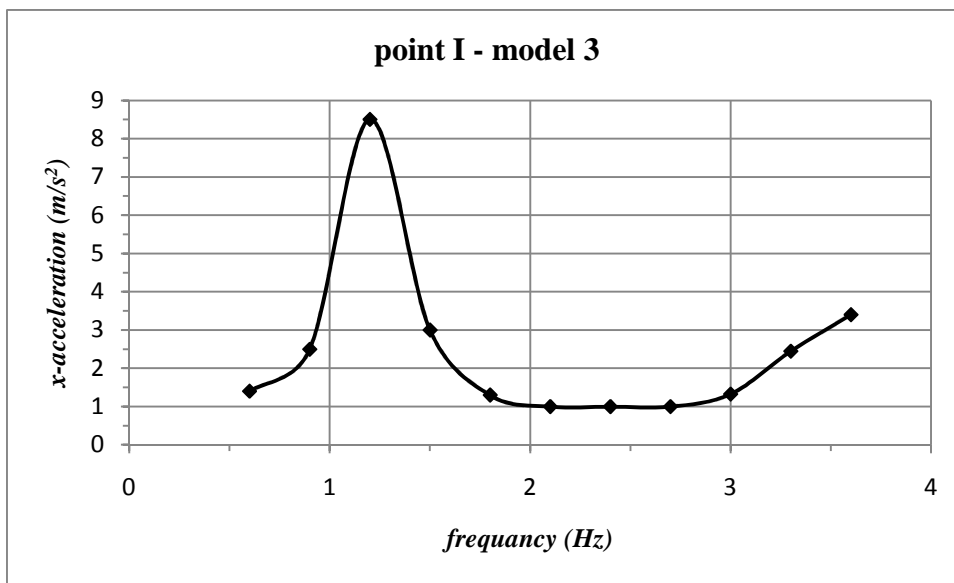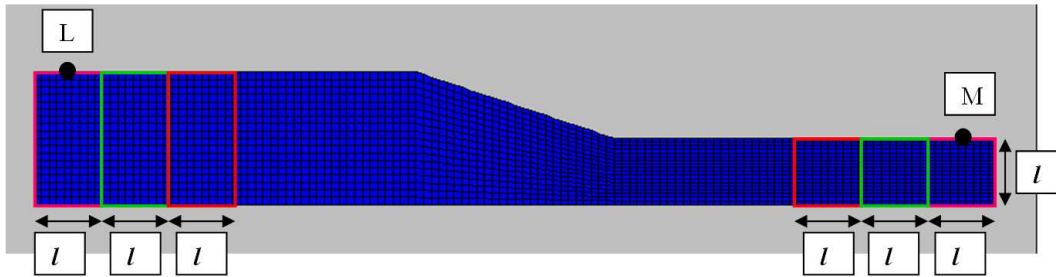***Figure 3.21*** *– Steady-state acceleration for monitoring point C.*

Figure 3.22 – *Steady-state acceleration for monitoring point D.*

Figure 3.23 – *Steady-state acceleration for monitoring point E.*

Figure 3.24 – *Steady-state acceleration for monitoring point F.*
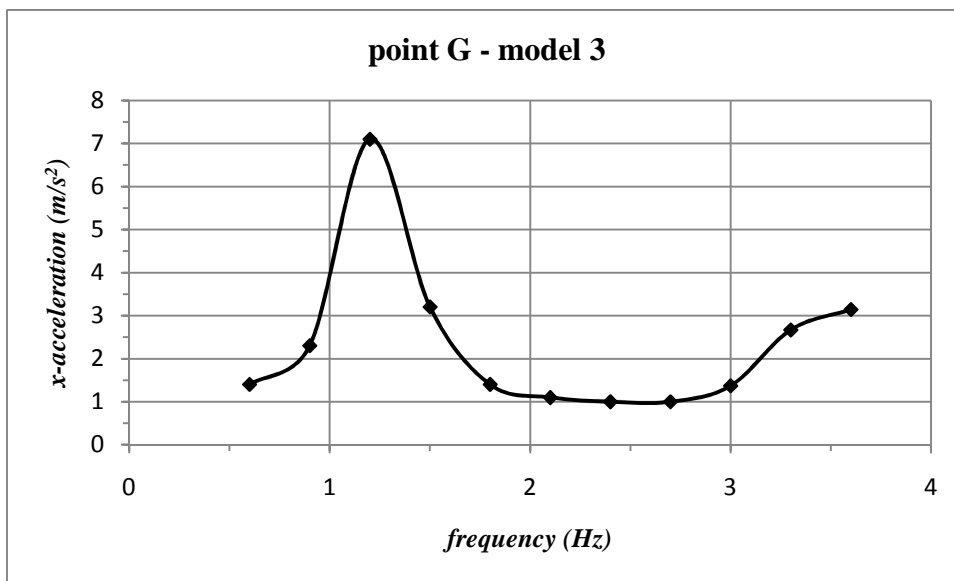
Figure 3.25 – *Steady-state acceleration for monitoring point G.*
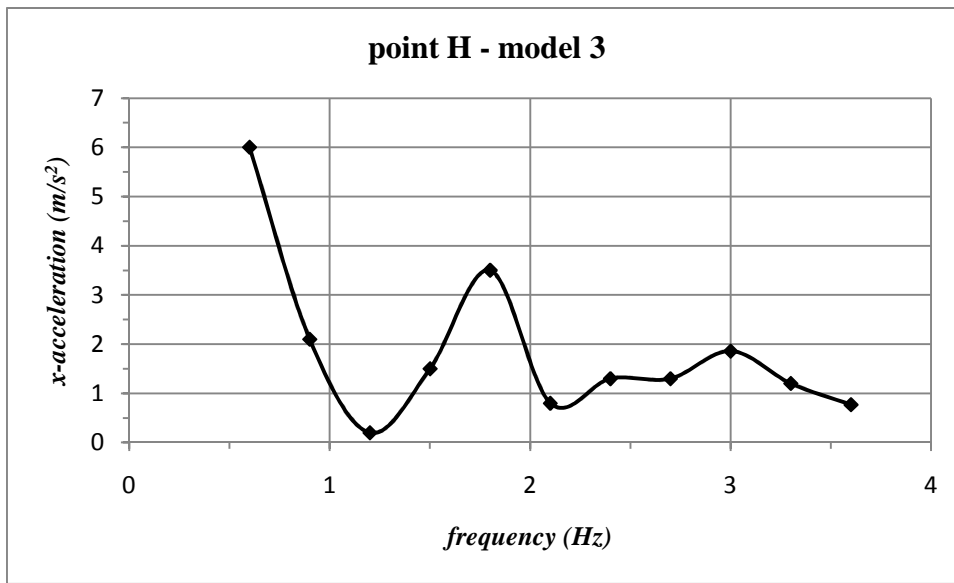
Figure 3.26 – *Steady-state acceleration for monitoring point H.*

Figure 3.27 – *Steady-state acceleration for monitoring point I.*

3.4 Model 4 - three extensions

In the last analysis, the model is extended the third time at its sides (Fig. 3.28, 3.29). Other two monitoring points (L, M) are added on the new extensions and a dynamic analysis is run. The same element size was used. The steady-state accelerations, as for the frequencies, for the monitoring points A-G are plotted in Figures 3.30 to 3.40.

Figure 3.28 - *Geometry of the model with the extension on the two sides and position of the two new monitoring points H and I.*
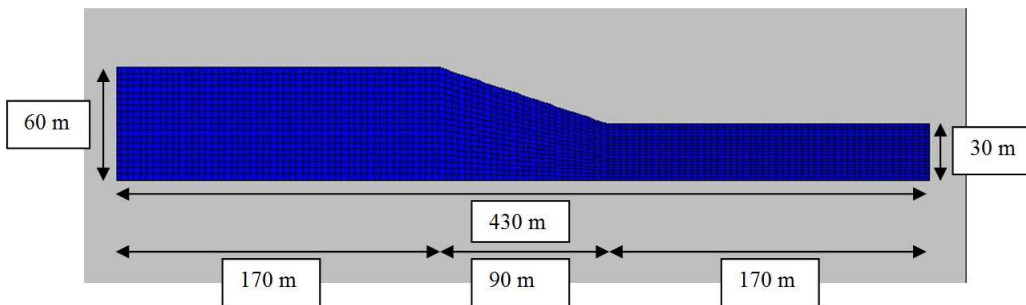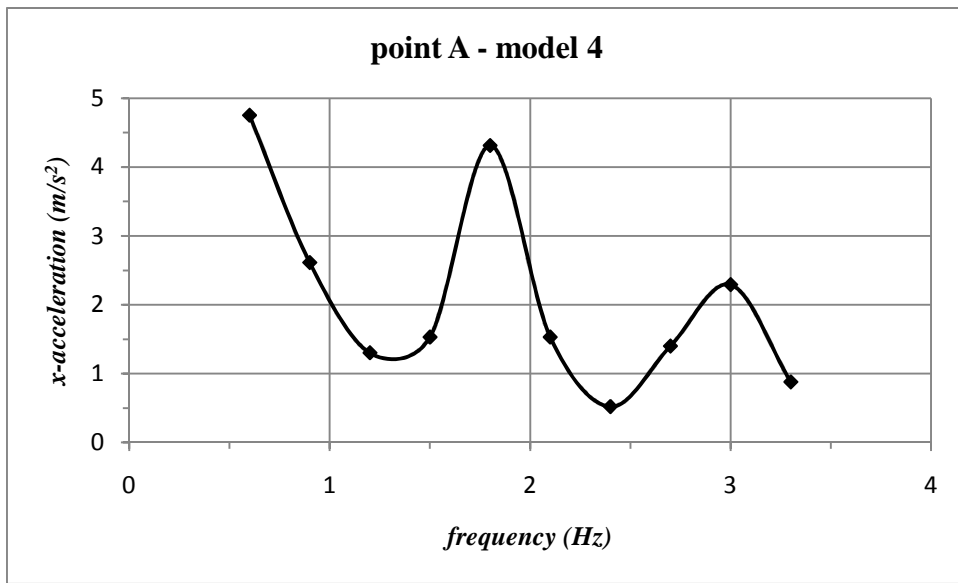

Figure 3.29 - *Geometry of the model*

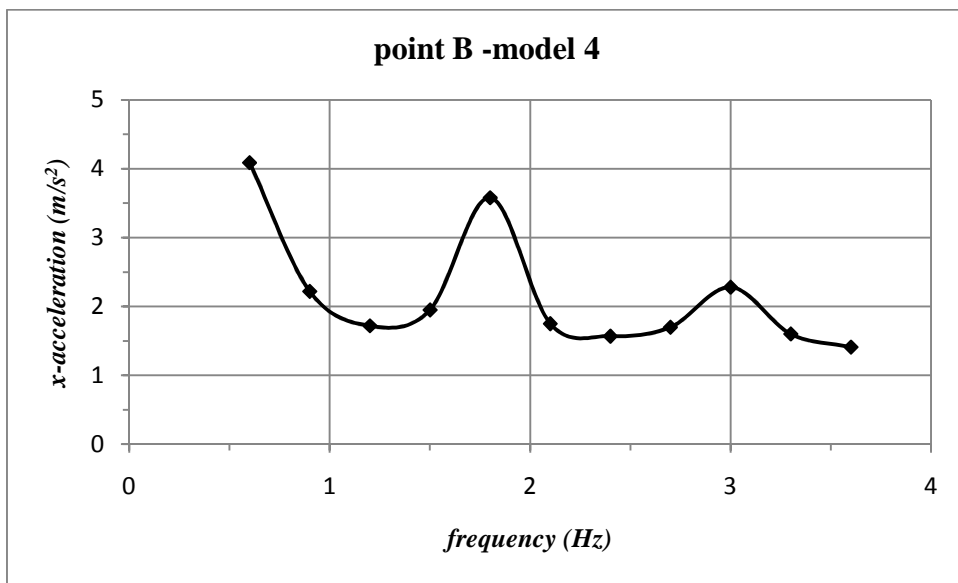**Figure 3.30** – *Steady-state acceleration for monitoring point A.*

Figure 3.31 – *Steady-state acceleration for monitoring point B.*
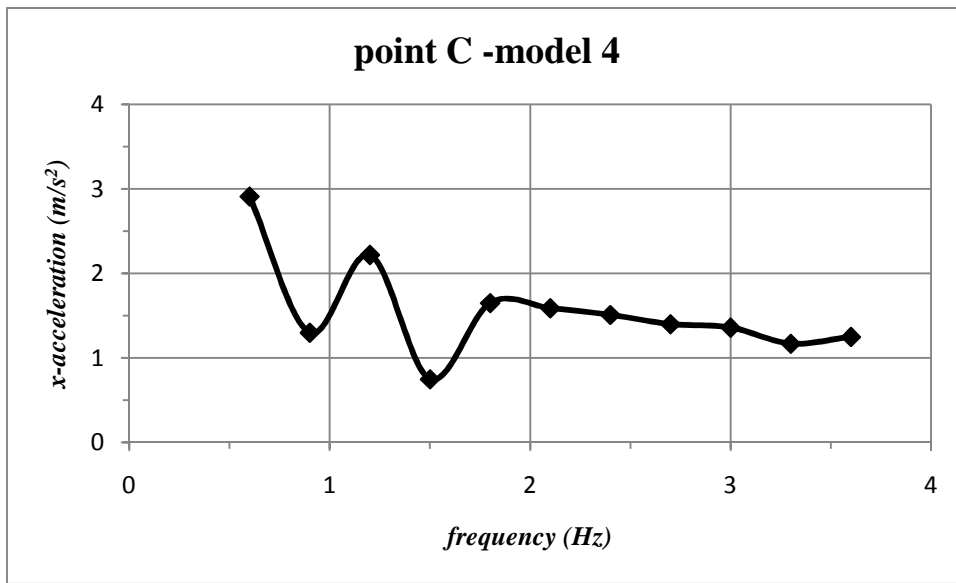
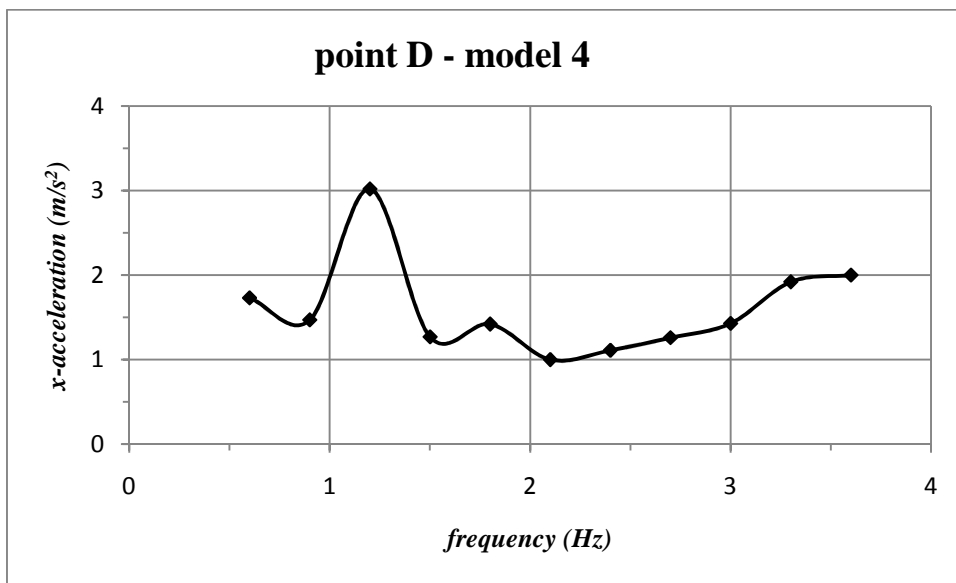**Figure 3.32** – *Steady-state acceleration for monitoring point C.*

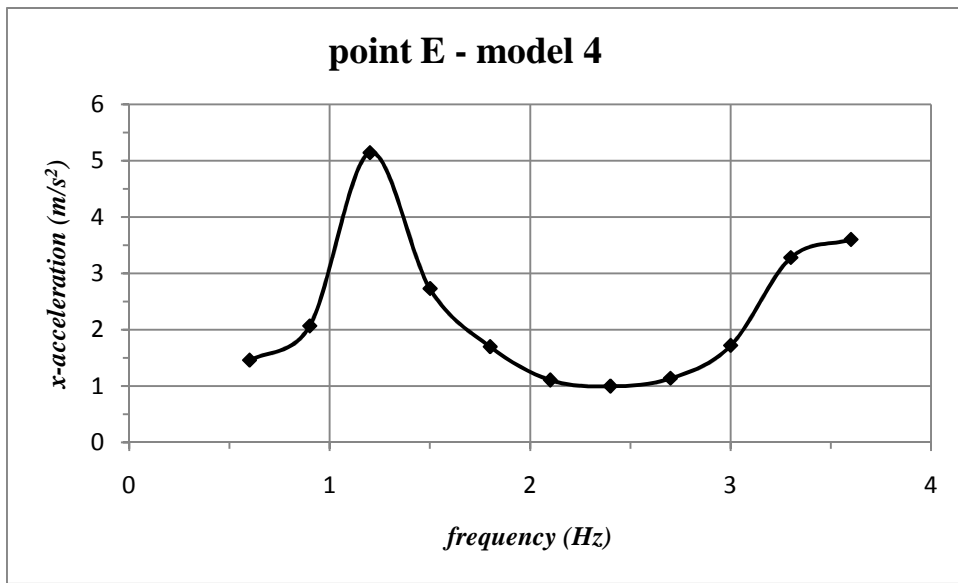**Figure 3.33** – *Steady-state acceleration for monitoring point D.*

Figure 3.34 – *Steady-state acceleration for monitoring point E.*

Figure 3.35 – *Steady-state acceleration for monitoring point F.*

Figure 3.36 – *Steady-state acceleration for monitoring point G.*

Figure 3.37 – *Steady-state acceleration for monitoring point H.*
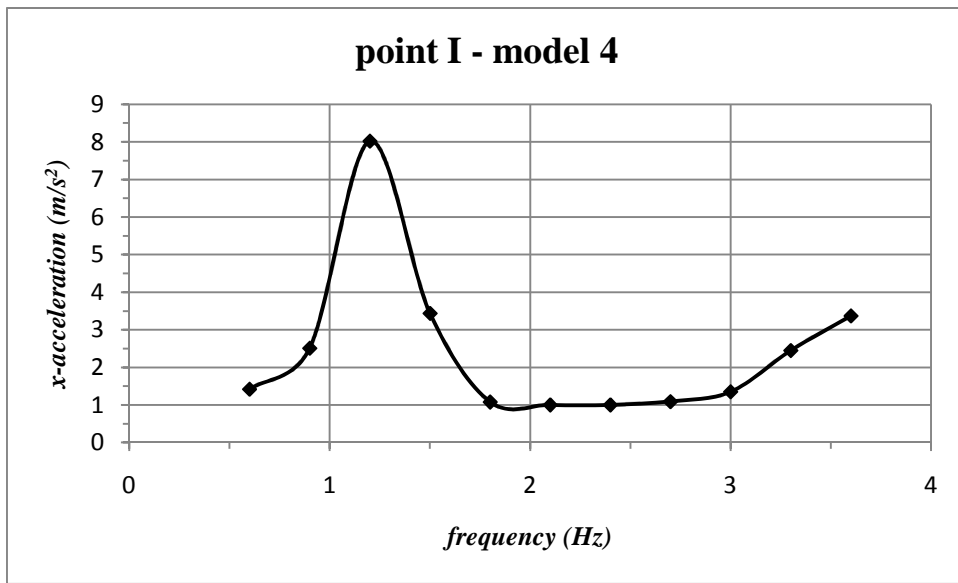
Figure 3.38 – *Steady-state acceleration for monitoring point I.*
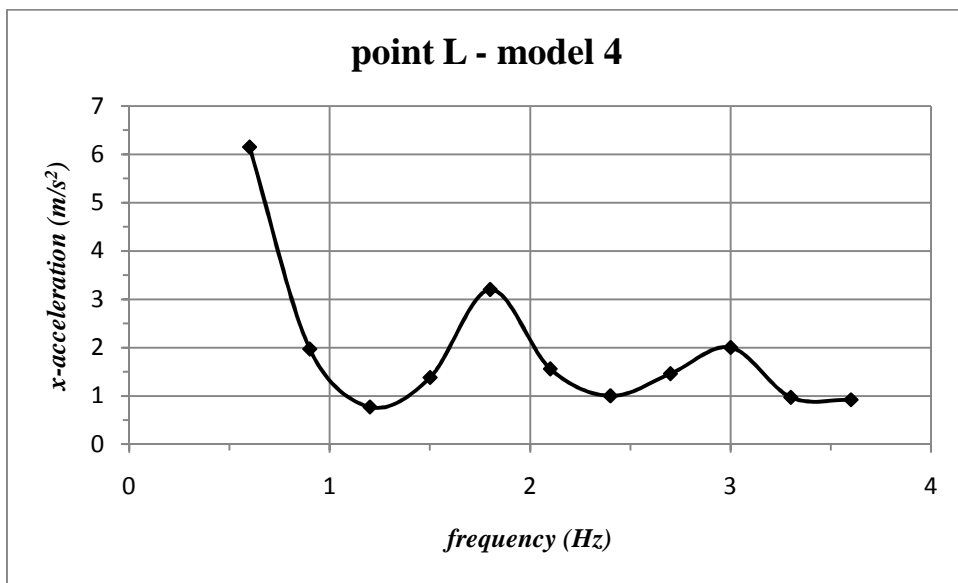
Figure 3.39 – *Steady-state acceleration for monitoring point L.*

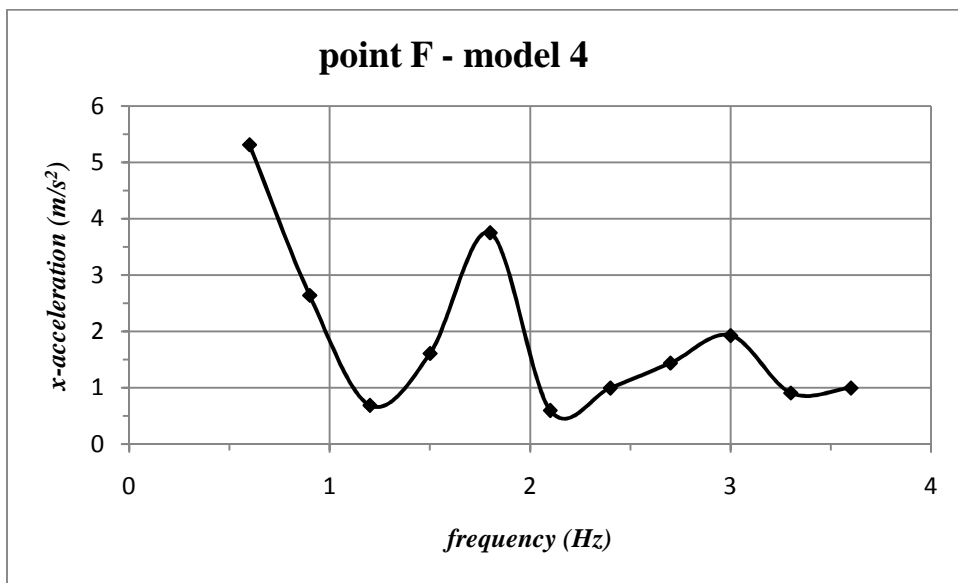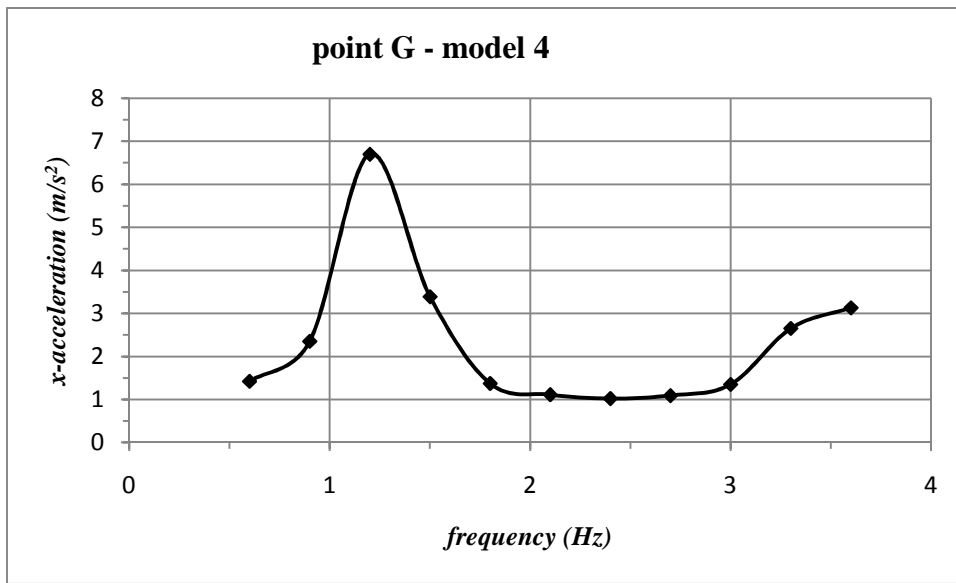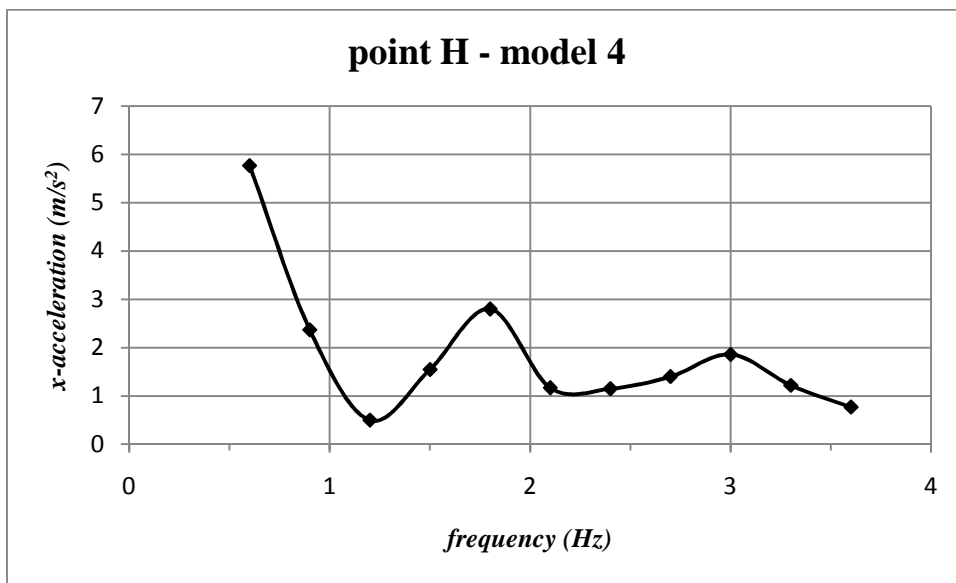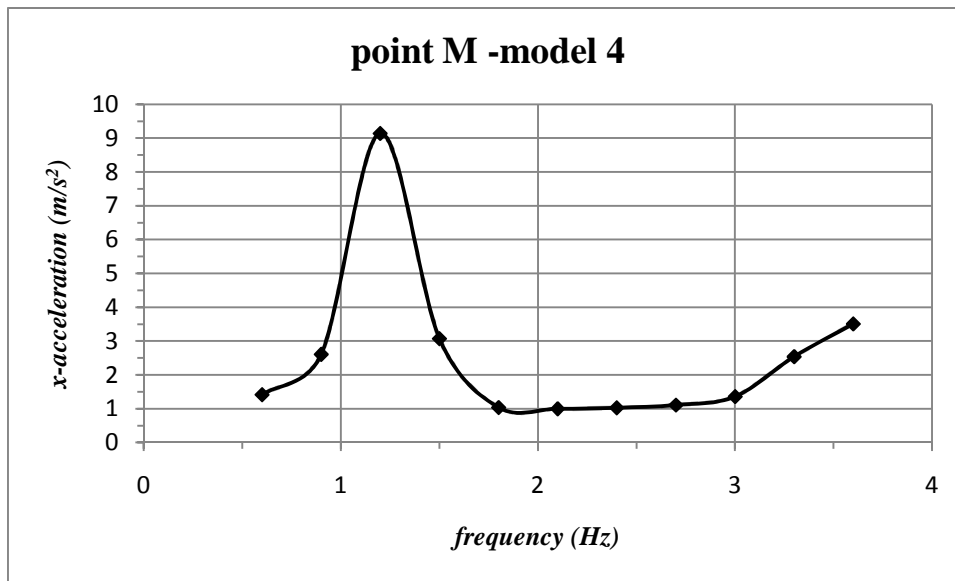**Figure 3.40** – *Steady-state acceleration for monitoring point M.*

3.5   Comparison between the results of different model

To analyze the results and understand the influence of boundary conditions, the monitoring points are considered one by one in different models. The four different models are resumed in *Figure 3.41* to *3.49*.
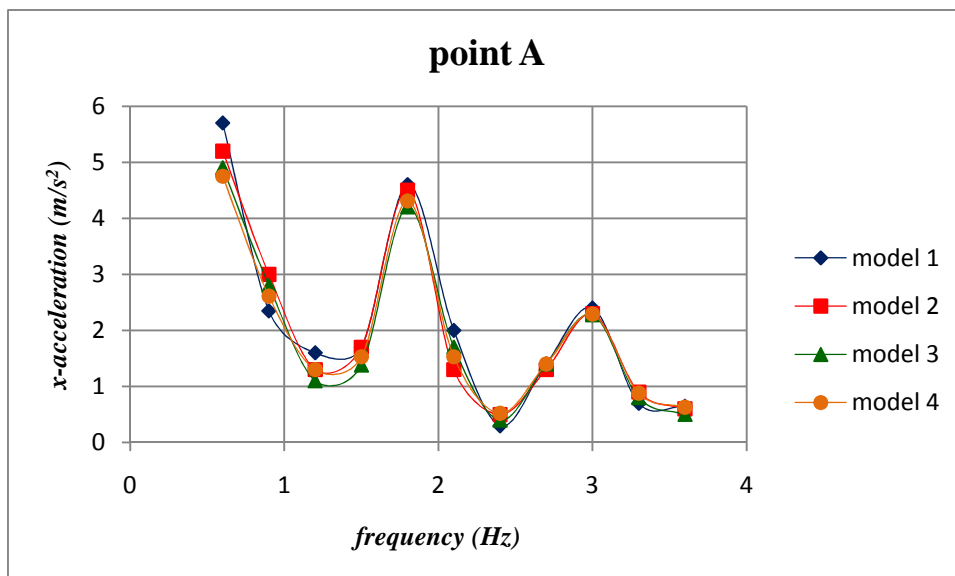
Figure 3.41 - *Monitoring point A.*
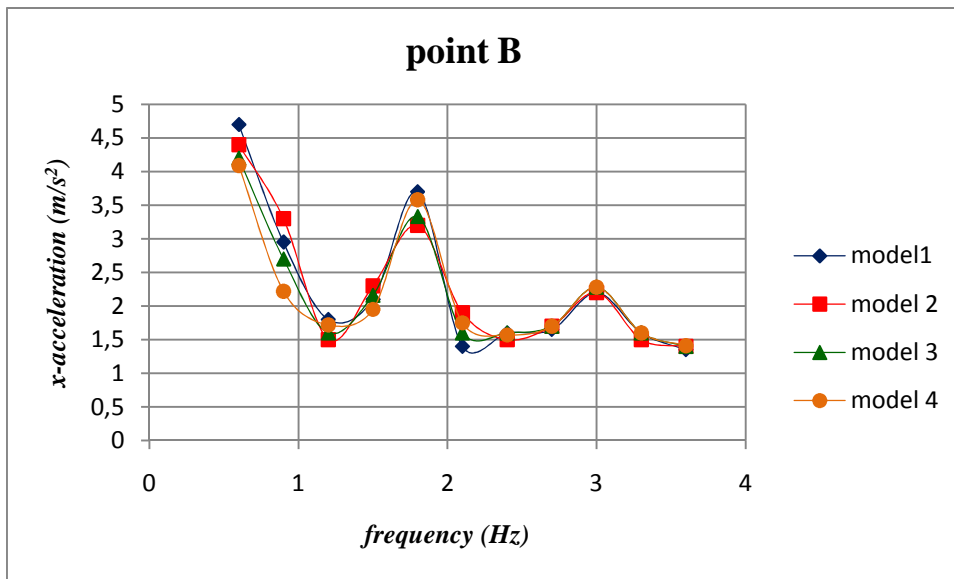
Figure 3.42 – *Monitoring point B.*
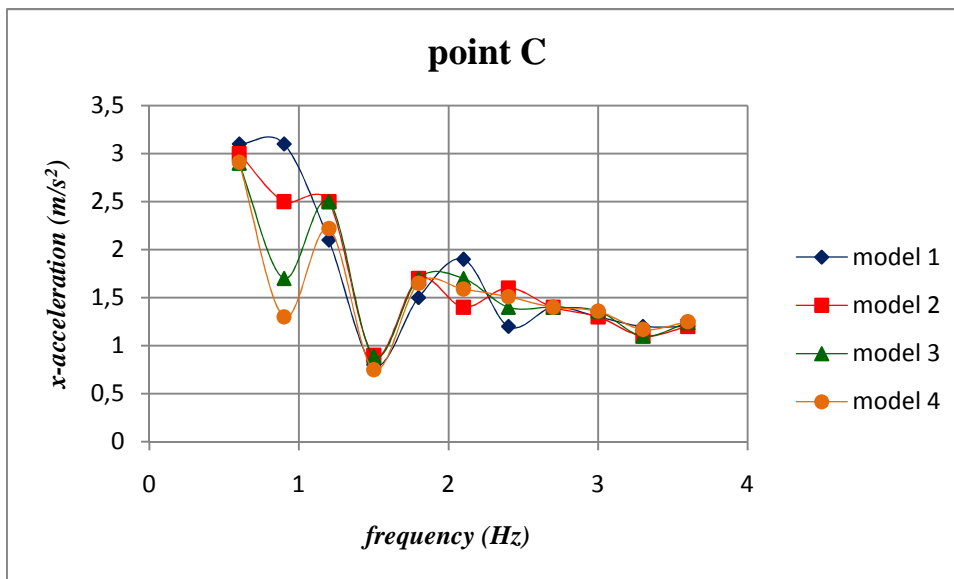
Figure 3.43 – *Monitoring point C.*
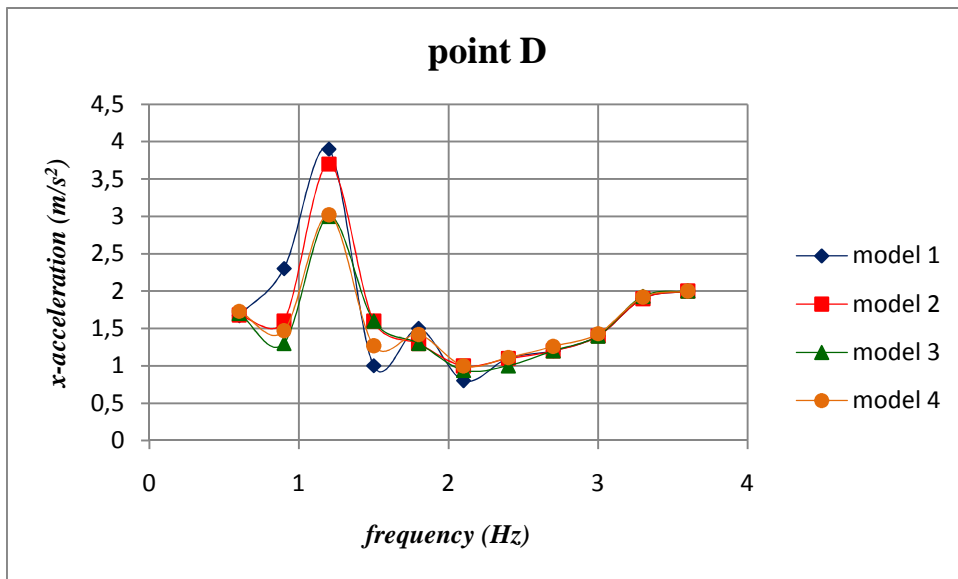
Figure 3.44 – *Monitoring point D.*
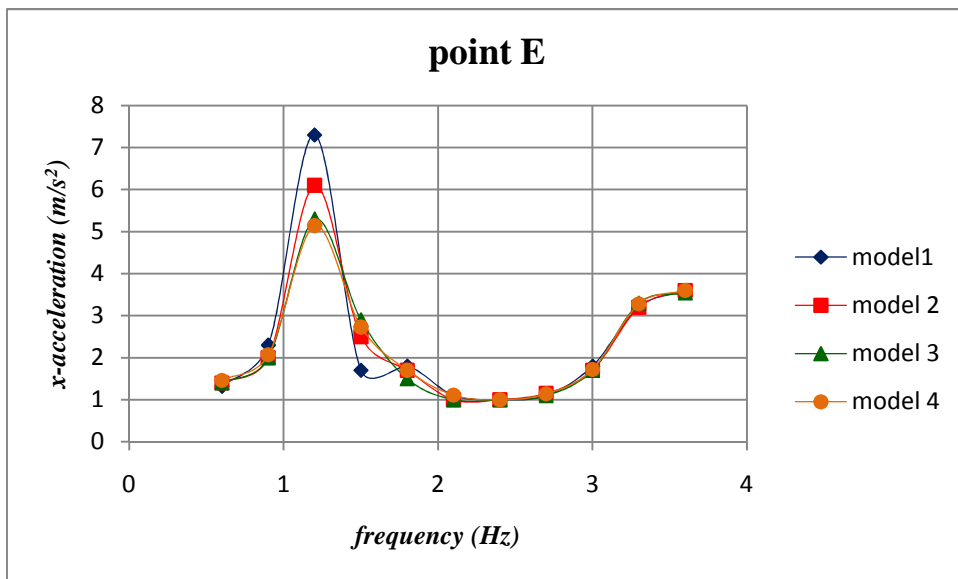
Figure 3.45 – *Monitoring point E.*
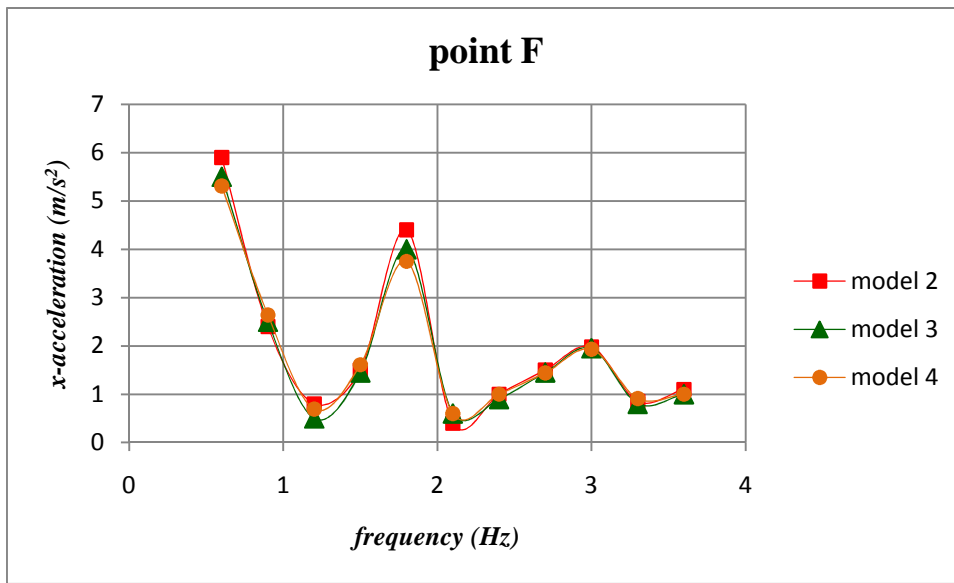
***Figure 3.46** – Monitoring point F.*
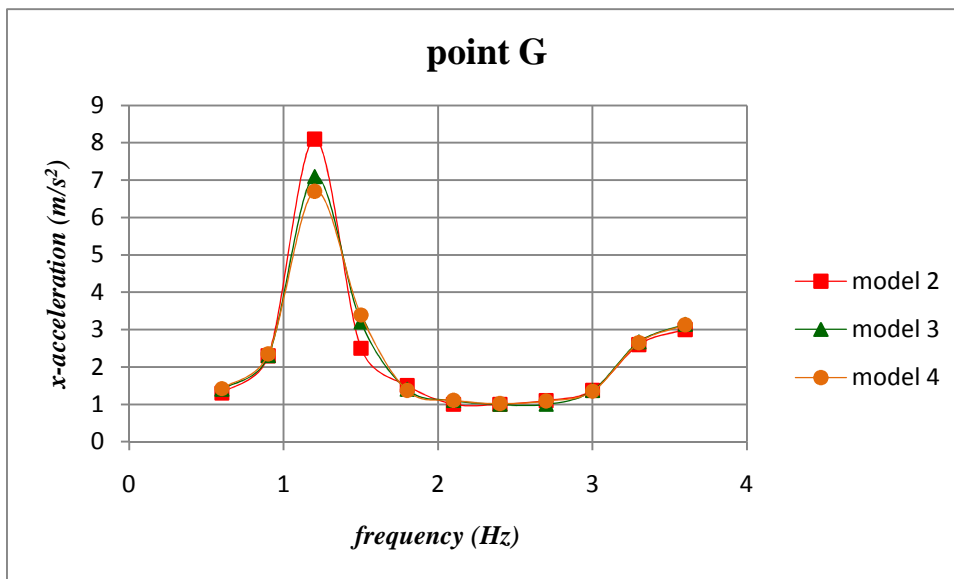
***Figure 3.47** – Monitoring point G.*
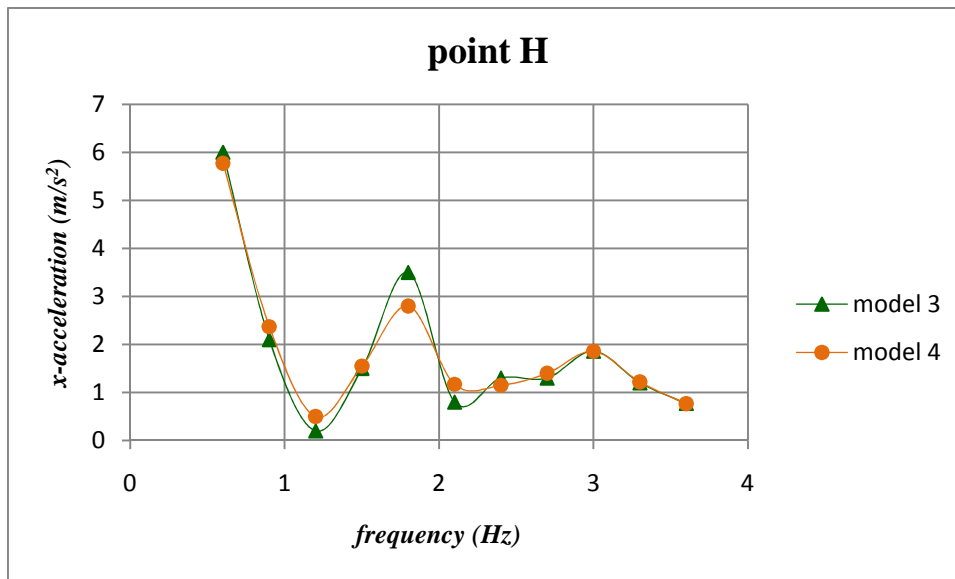
***Figure 3.48** – Monitoring point H.*
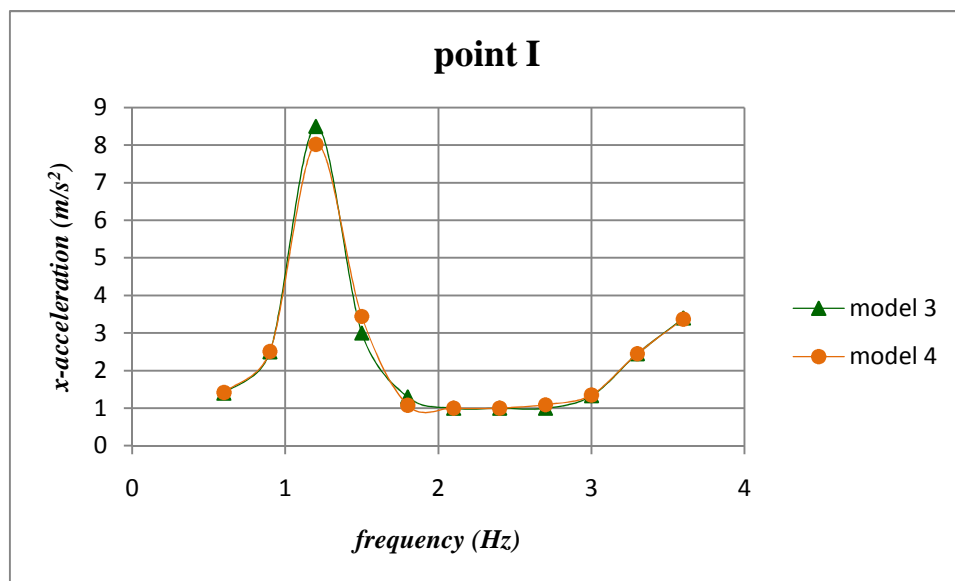
***Figure 3.49** – Monitoring point I.*

Using these plots, one notes that the differences between *model 3* and *model 4* are very small. So it is possible to conclude that the location of the lateral boundaries in *model 3* is satisfactory for obtaining reliable results and there is no need to use longer model laterally. This observation on the optimum location of the boundaries will be used in the analyses in the slope analyses in this thesis.

Chapter 4 – Performance of SANICLAY model

The objective of this chapter is to perform some numerical simulation with the SANICLAY model and to test its sensitivity.

4.1 Description of the model and initialization

The first simulation consisted of some different dynamic analyses. The geometry of the model is a slope with a simple shape, as shown in *Figure.4.1,* excited by a dynamic load at the bottom in the *x-direction*.
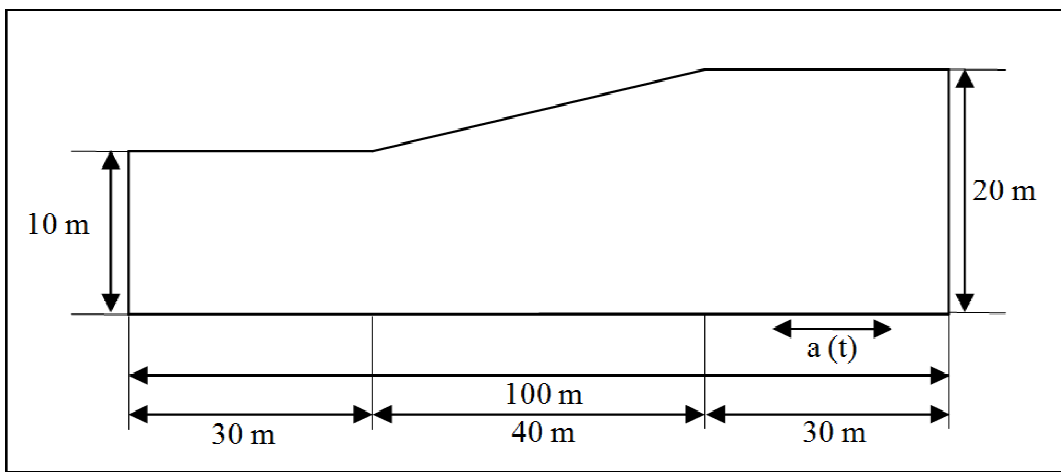
Figure 4.1 - *Geometry of the model with the dynamic load in the x-direction.*

The dynamic load has the following expression (*Figure 4.2*):

$$a(t) = 1,0 \cdot \sqrt{\beta \cdot e^{(-\alpha t)} \cdot t^{\gamma}} \cdot \sin(\omega t)$$

Where the values of the parameters α, β, γ are:

$$\alpha = 3,3$$

$$\beta = 0,19$$

$$\gamma = 12$$

$$freq = 2\ Hz$$

$$\omega = 2 \cdot \pi \cdot freq = 12{,}56 \, \frac{rad}{sec}$$

With these values the maximum acceleration of the input is

$$a_{max} = 2{,}5 \, \frac{m}{s^2}$$
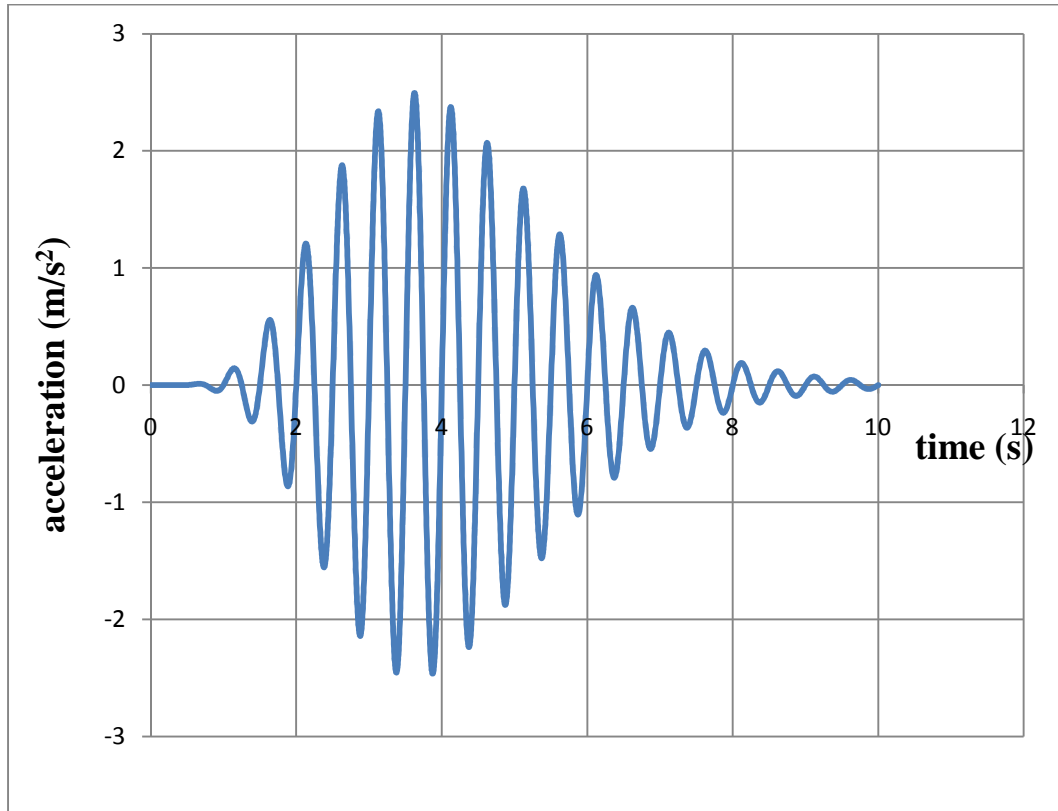
Figure 4.2 - *Excitation applied at the bottom of the models in the x-direction.*

For these analyses free field boundary condition have been used.

4.2 Influence of boundary conditions

As in the previous chapter, it is interesting to analyze the influence of the boundary conditions when SANICLAY model is adopted. The results of three dynamic analyses with different geometries are compared. The first analysis is with the original model, model *n.1* (*Figure 4.3 a)*), in the second analysis an extension of $30 \, m$ is added at both sides of the first geometry (*Figure 4.3 b)*) and in the third model, a second extension of *30 m* is added at both sides (*Figure 4.3 c)*).
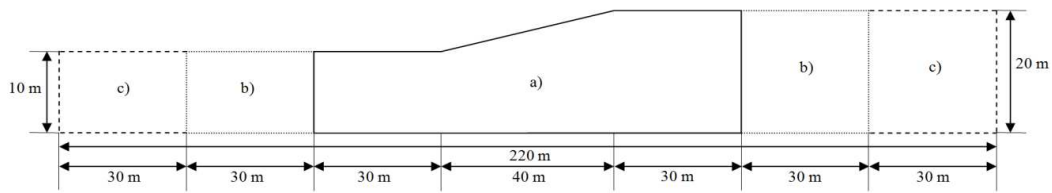
Figure 4.3 - *Geometry of the model: a) model n.1; b) model n.2 c) model n.3.*

Below are shown the time histories of shear strain at the monitoring points *P3* (from *Figure 4.4* to *Figure 4.6*) and *P5* (from *Figure 4. 7* to *Figure 4. 9*) which present some interesting results.
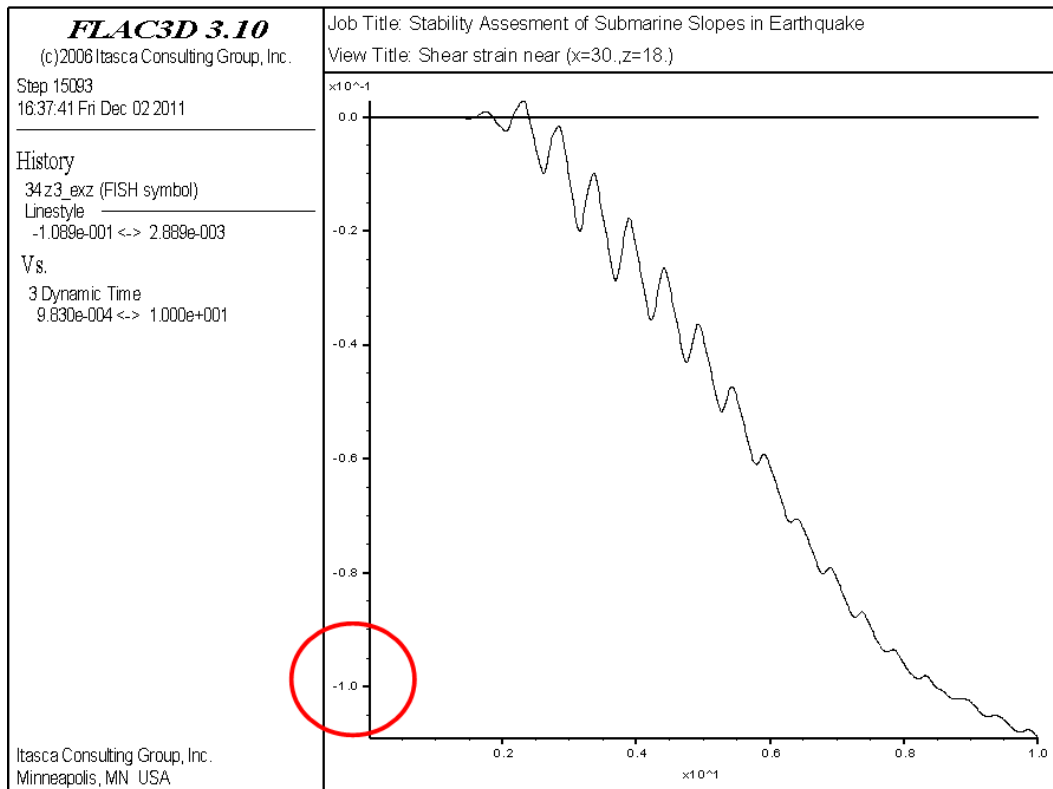
Figure 4.4- *Shear strain vs Dynamic time of P3 (x=30,y=18), model n.1.*
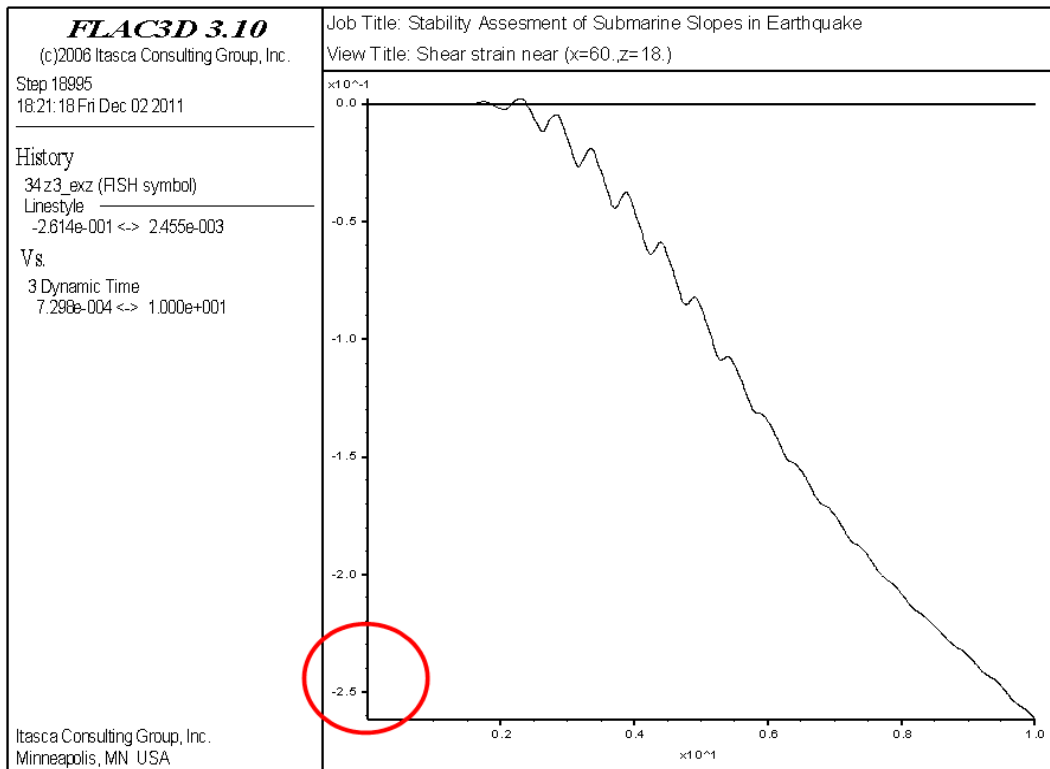
Figure 4.5 - *Shear strain vs Dynamic time of P3 (x=30,y=18), model n.2.*
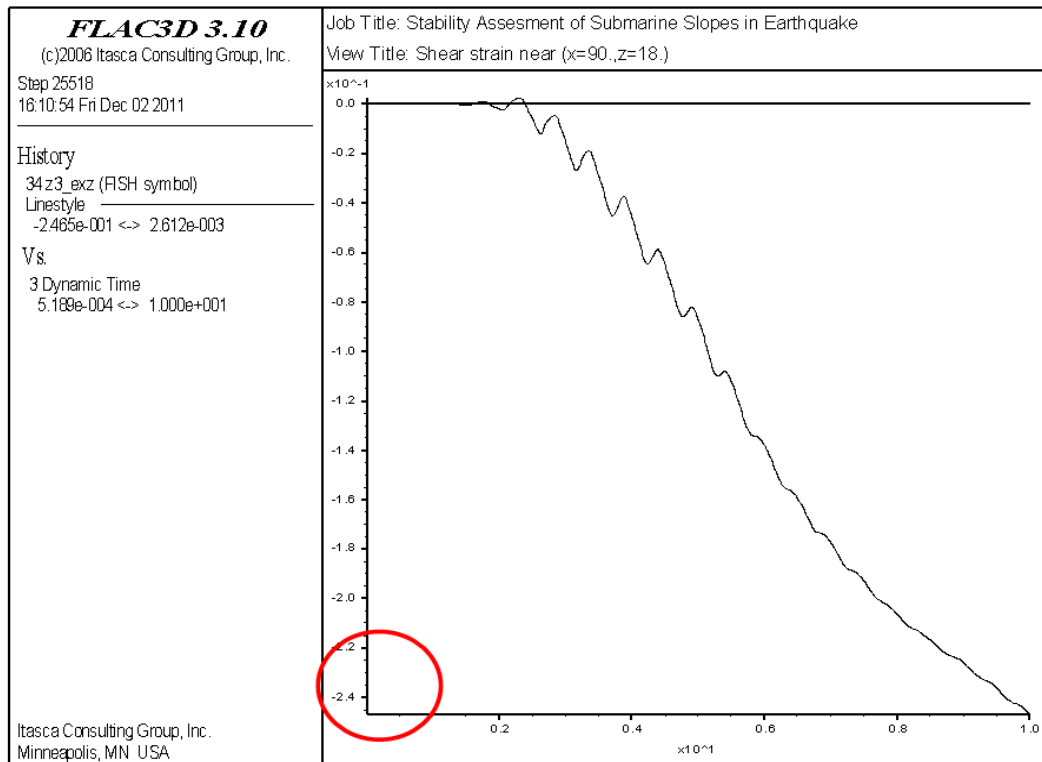
Figure 4.6 - *Shear strain vs Dynamic time of P3 (x=30,y=18), model n.3.*
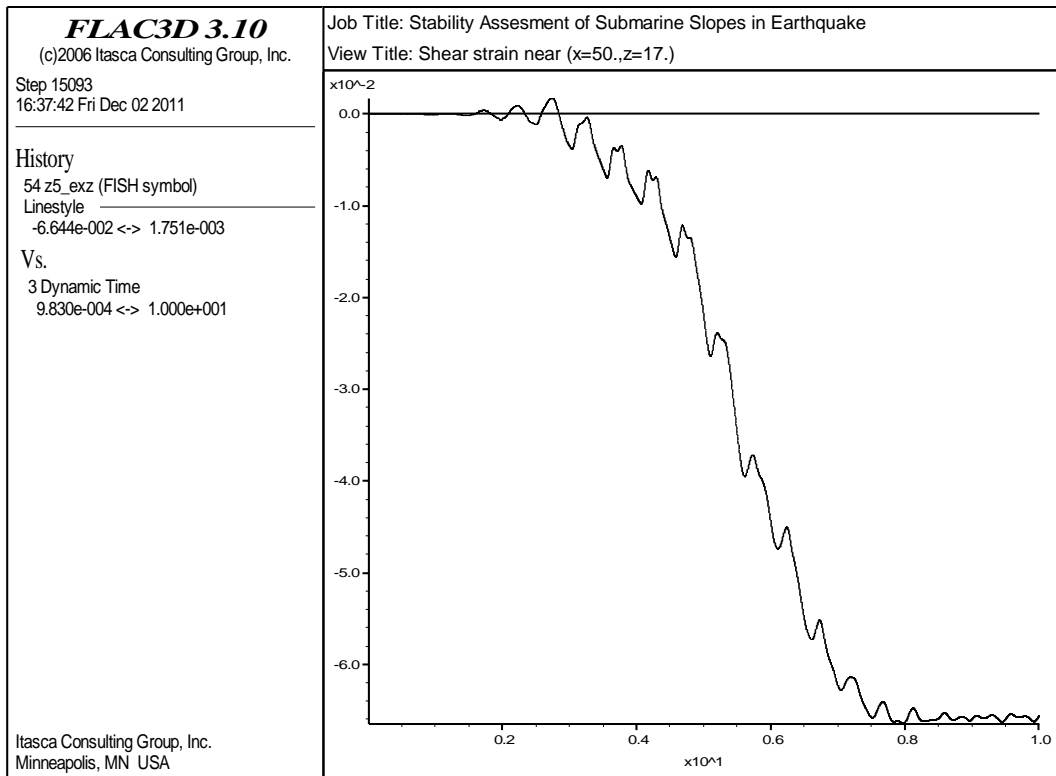
Figure 4.7 - *Shear strain vs Dynamic time of P5 (x=50,y=17), model n.1.*
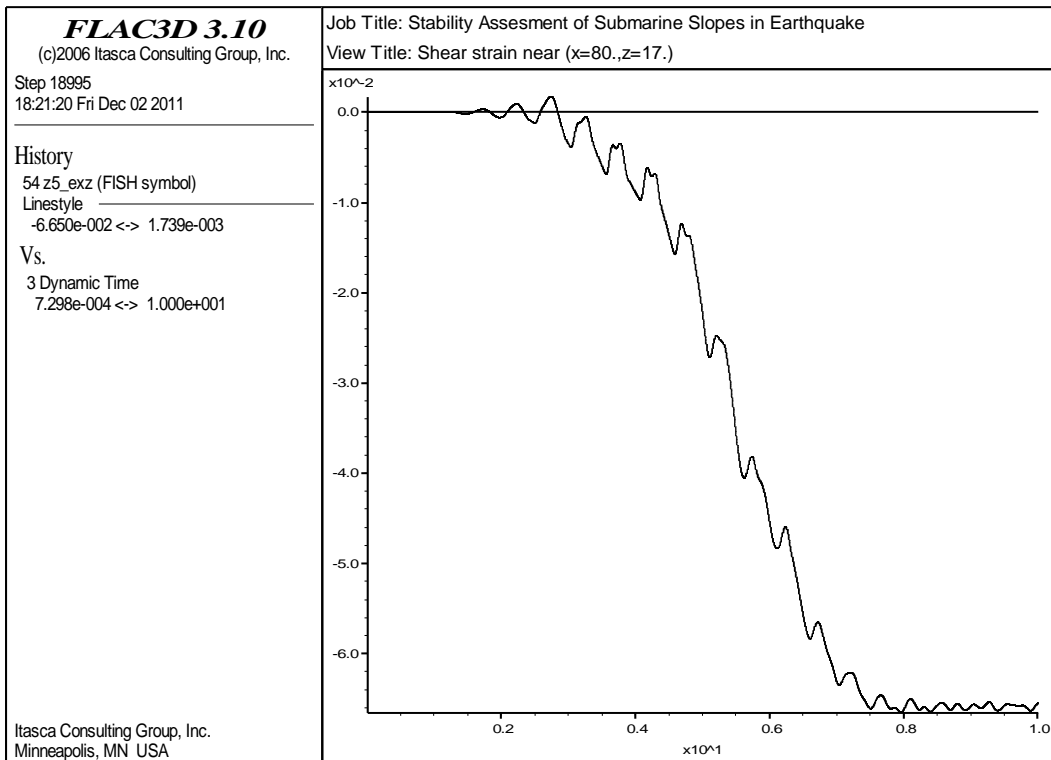
Figure 4.8 - *Shear strain vs Dynamic time of P5 (x=50,y=17), model n.2.*

FLAC3D 3.10
(c)2006 Itasca Consulting Group, Inc.

Step 25518
16:10:56 Fri Dec 02 2011

History
54 z5_exz (FISH symbol)
Linestyle
-6.442e-002 <-> 1.743e-003

Vs.
3 Dynamic Time
5.189e-004 <-> 1.000e+001

Itasca Consulting Group, Inc.
Minneapolis, MN USA

Job Title: Stability Assesment of Submarine Slopes in Earthquake
View Title: Shear strain near (x=110.,z=17.)
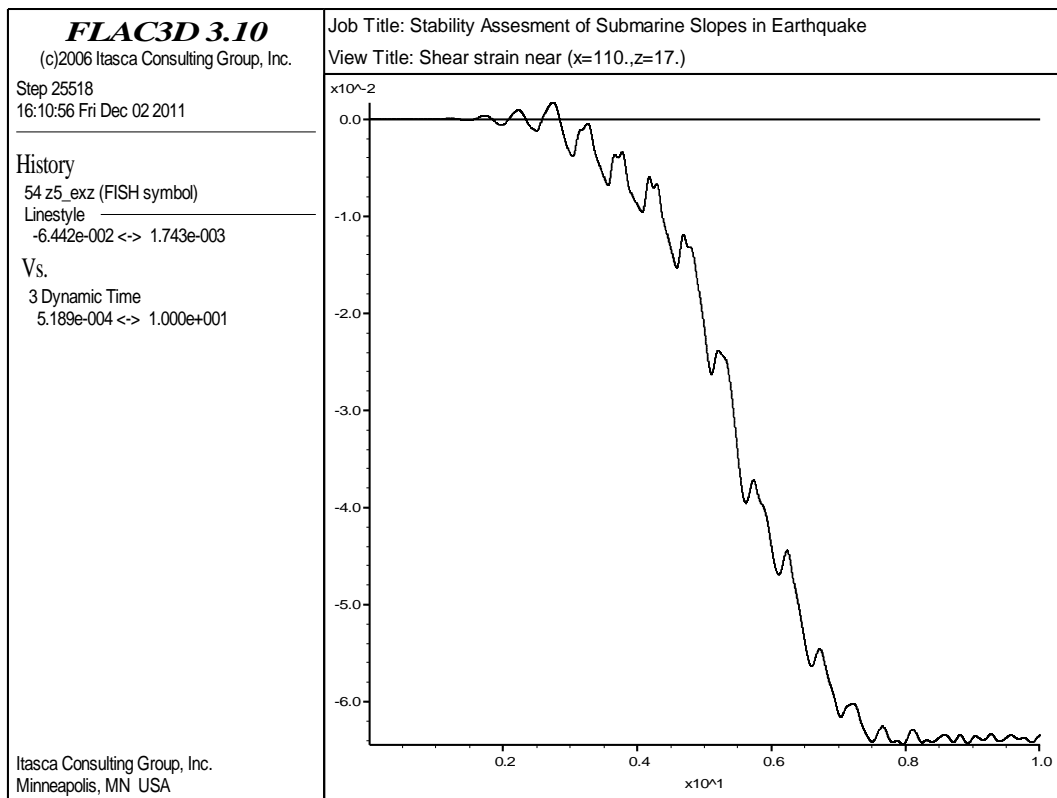
Figure 4.9- *Shear strain vs Dynamic time of P5 (x=50,y=17), model n.3.*

Considering the results of point P3, one might conclude that the extension in *4.3 b)* is sufficient to obtain stable results which are almost unaffected by the lateral boundaries.

4.3 Sensitivity to parameter κ (slope of elastic swelling line)

In this section, the sensitivity of the results to parameter κ, which represents the slope of elastic swelling line (*Figure 4.10*), is studied.
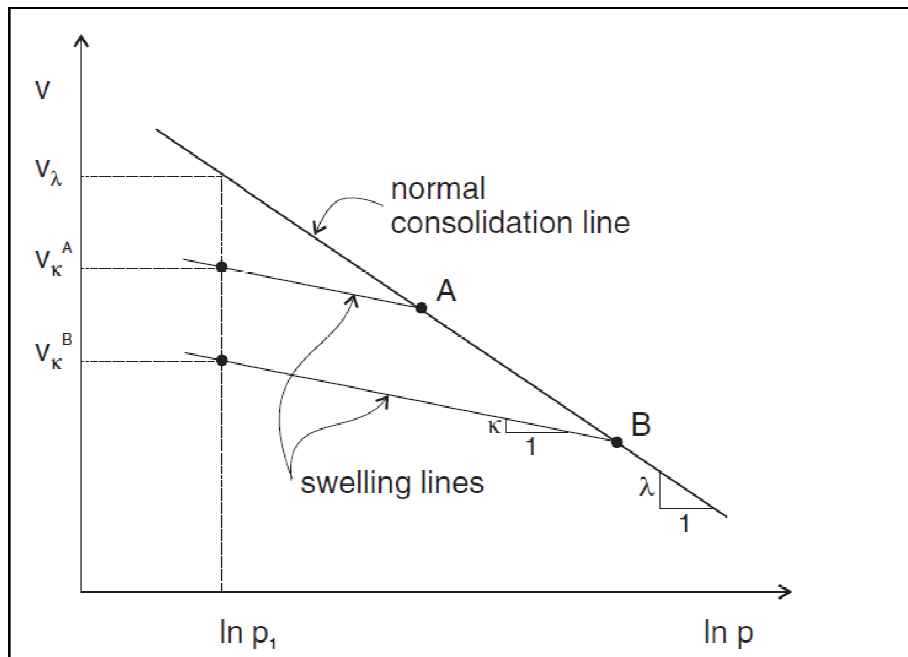
***Figure 4.10** - Normal consolidation line and unloading-reloading (swelling) line for an isotropic compression test. (FLAC[3D] Manual).*

Because of the results of the previous analyses only the model with one extension applied at each side is used (*Figure 4.11*).
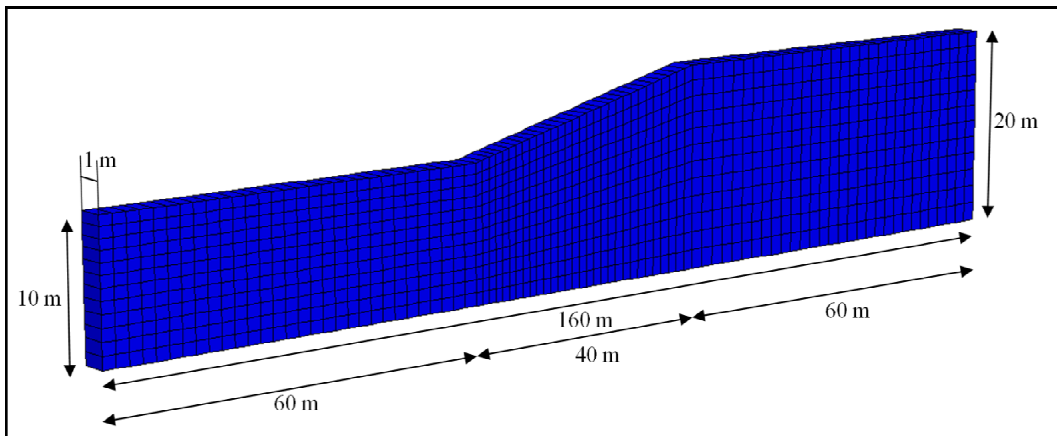
***Figure 4.11** - Geometry of the model.*

A value of $\lambda = 0{,}07$ (slope of normal consolidation line, see *Figure 4.10*) is considered realistic. Then four different dynamic analyses are made, changing each time the value of parameter κ (see *Table 4.1*)

:

case	values of κ
case 1	0,005
case 2	0,010
case 3	0,03
case 4	0,04

Table 4.1 - *Values of parameter κ.*

At the end of each analysis the trend of *Bulk modulus* (K) is considered and the graphics are shown in *Figure 4.13*. In every case two value of K are taken: one on the left side (K_L) of the model and the other on the right side (K_R), both at an average height ($10\ m$ for the left side, $15\ m$ for the right side), see *Figure 4.12*. Starting from these values of K, the value of own frequency of the model is calculated as follows:

$$E = 3K(1 - 2v) \ ; \quad G = \frac{E}{2(1+v)}$$

$$v_s = \sqrt{\frac{G}{\rho}}$$

$$f = \frac{v_s}{H}$$

where:

$\rho = 2000\ \frac{kg}{m^3}$

$v = 0{,}2$

$H_{left} = 10\ m \quad H_{right} = 20\ m$

In *Table 4.2* are shown the different values of the frequency of the model at the left side and at the right side, for all the cases considered.

k	Frequency at left side (Hz)	Frequency at right side (Hz)
0,005	8,66	5,30
0,01	6,12	4,33
0,03	4,74	2,73
0,04	3,87	2,37

Table 4.2 - *Values of the frequency of the model at the left side and at the right side.*
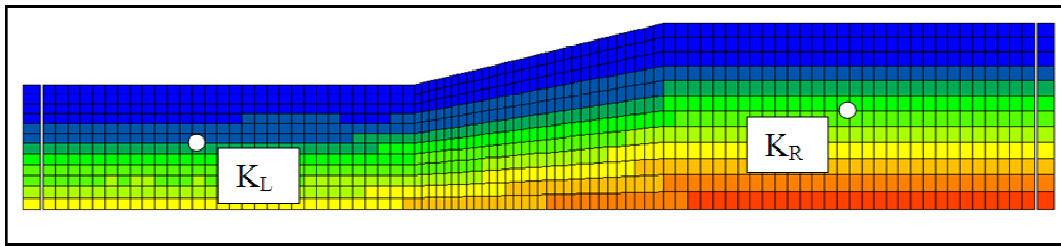
Figure 4.12 - *Zones in which are taken the values of the Bulk modulus, K_L and K_R.*
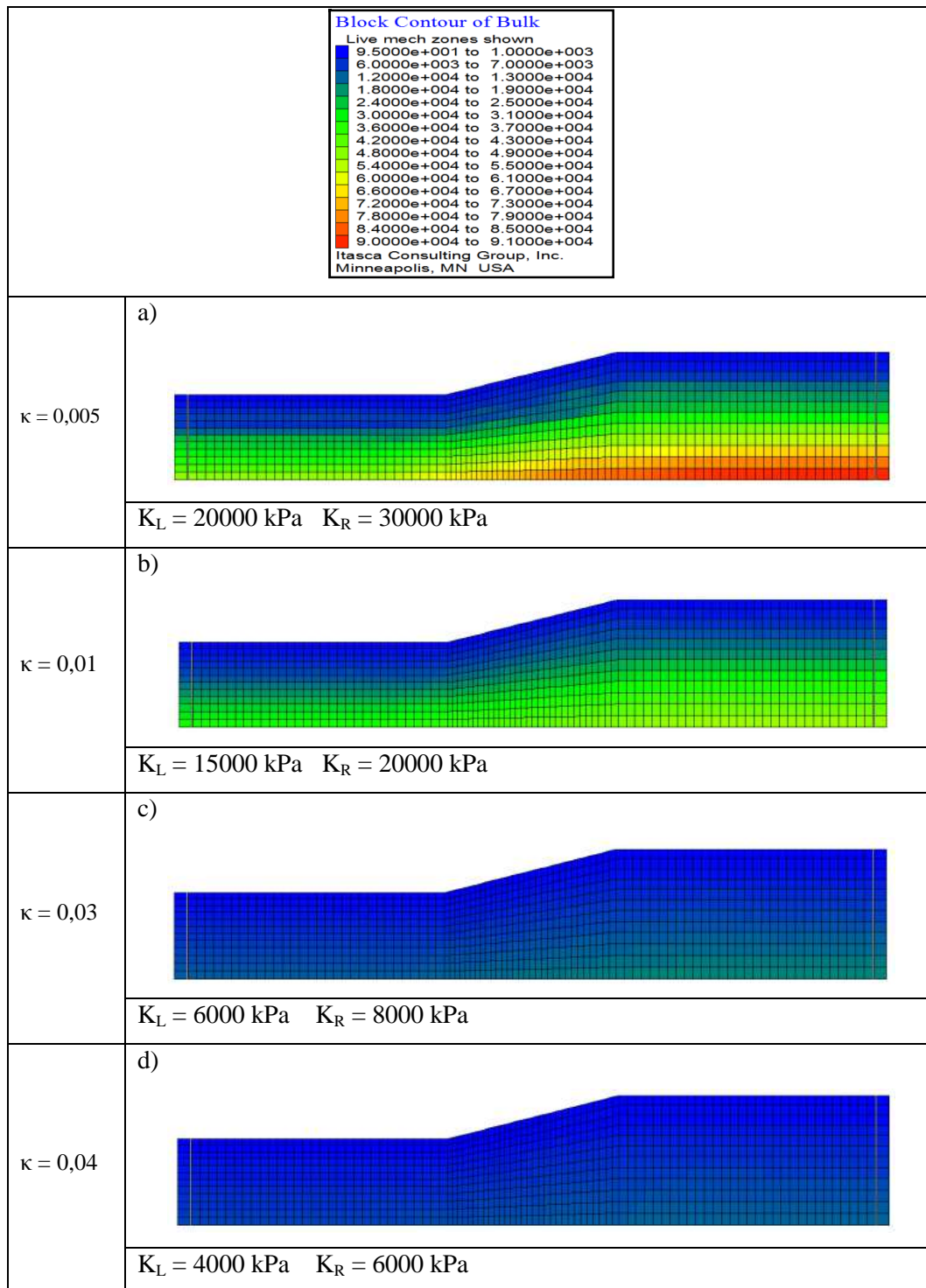
Figure 4.13 - *Bulk modulus: a) κ = 0,005 b) κ = 0,01 c) κ = 0,03 d) κ = 0,04*

Figure 4.14 shows the graphics of the final displacements of the sensitivity analysis with parameter κ, in the two cases without damping and with a Rayleigh damping of 2%.
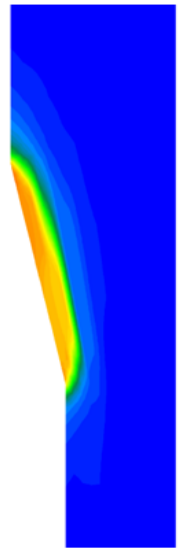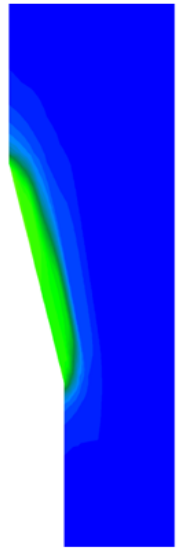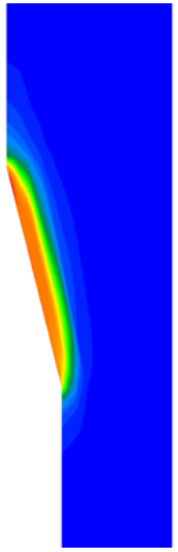
Figure 4.14 - Graphics of final displacements in the sensitivity analysis of parameter κ.

The excitation frequency is 2 Hz. Observing the graphics of the displacement (*Figure 4.14*) it is possible to note that no resonance happens; in fact the larger displacements happens in the case with κ equal to 0,01, in which:

κ	*Frequency at left side (Hz)*	*Frequency at right side (Hz)*
0,010	6,12	4,33

In this case the maximum displacement is $7,53\,m$ for the case without damping and 3,68 m for 2% of damping. The case with the frequencies closest to the input frequency ($2\,Hz$) is the one with $\kappa = 0,04$ that is the case with minimum displacements. The results are not in accord with the theory, probably because of the non linearity in the response.

Next, it was is decided to consider again three of the previous analyses, exactly those with the following values of parameter κ: 0,005, 0,01 and 0,03. The *x*-displacements of three different monitoring points (*Figure 4.15*) on the top of the model are registered and their graphs are shown in *Figure 4.16* (without damping) and *Figure 4.17* (2% of damping).
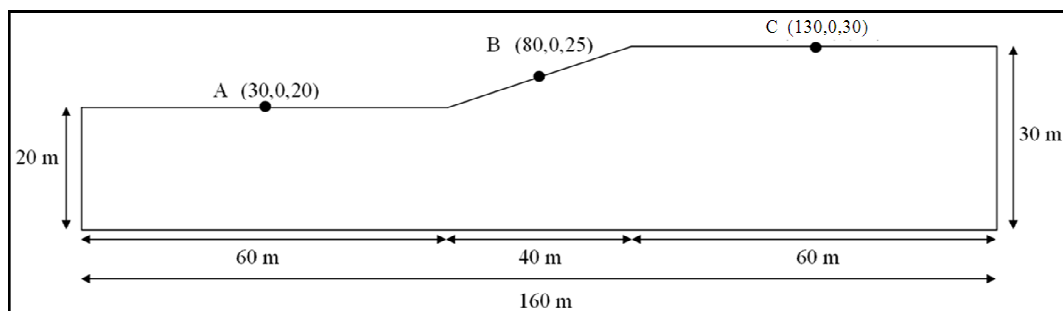
Figure 4.15 - *Geometry of the model and coordinates of the monitoring points A, B and C.*
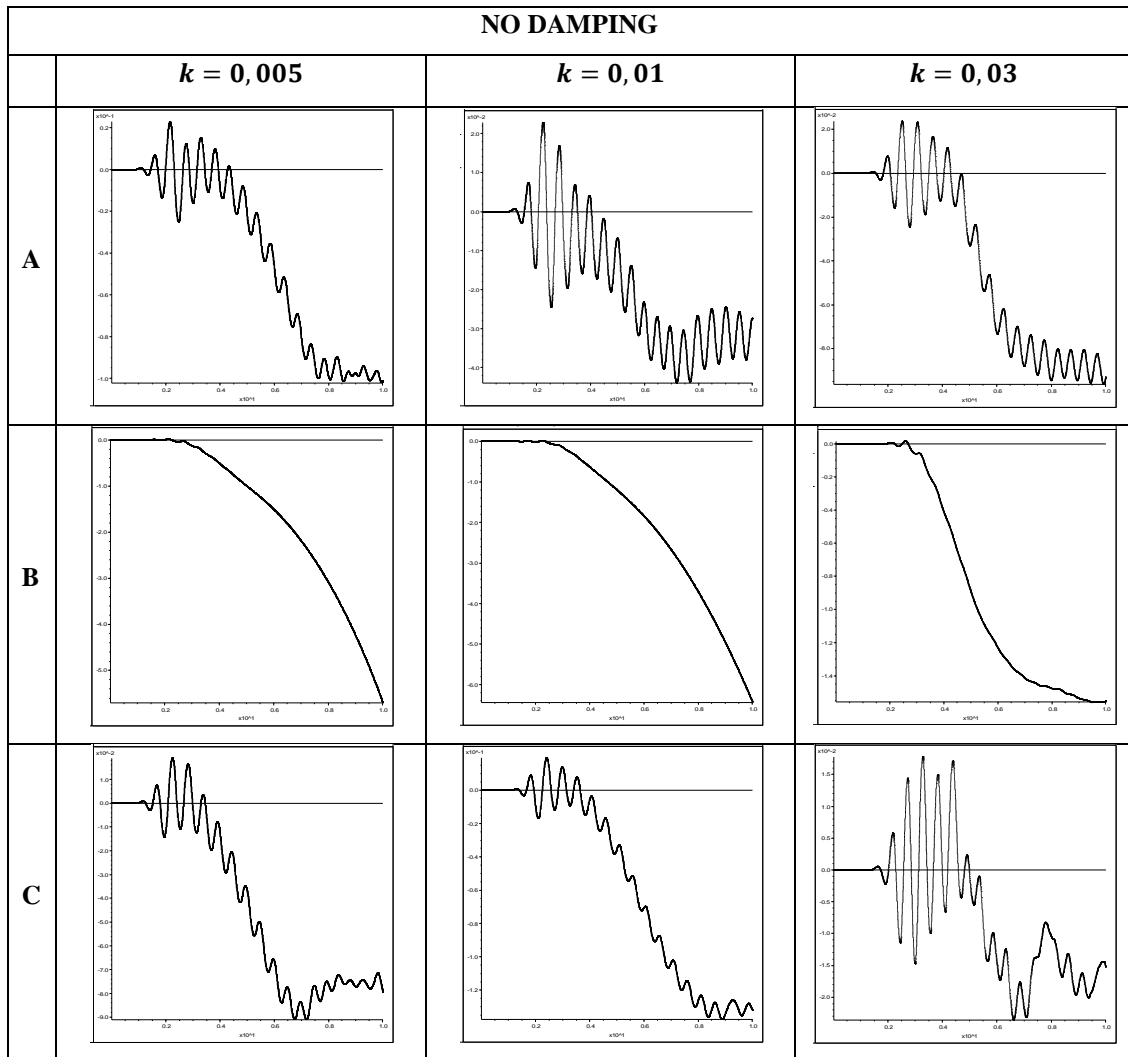
Figure 4.16 - *Graphics of x-displacements of the three monitoring points A, B and C for the*

three different values of parameter k. Analysis without damping.

DAMPING		
$k = 0,005$	$k = 0,01$	$k = 0,03$
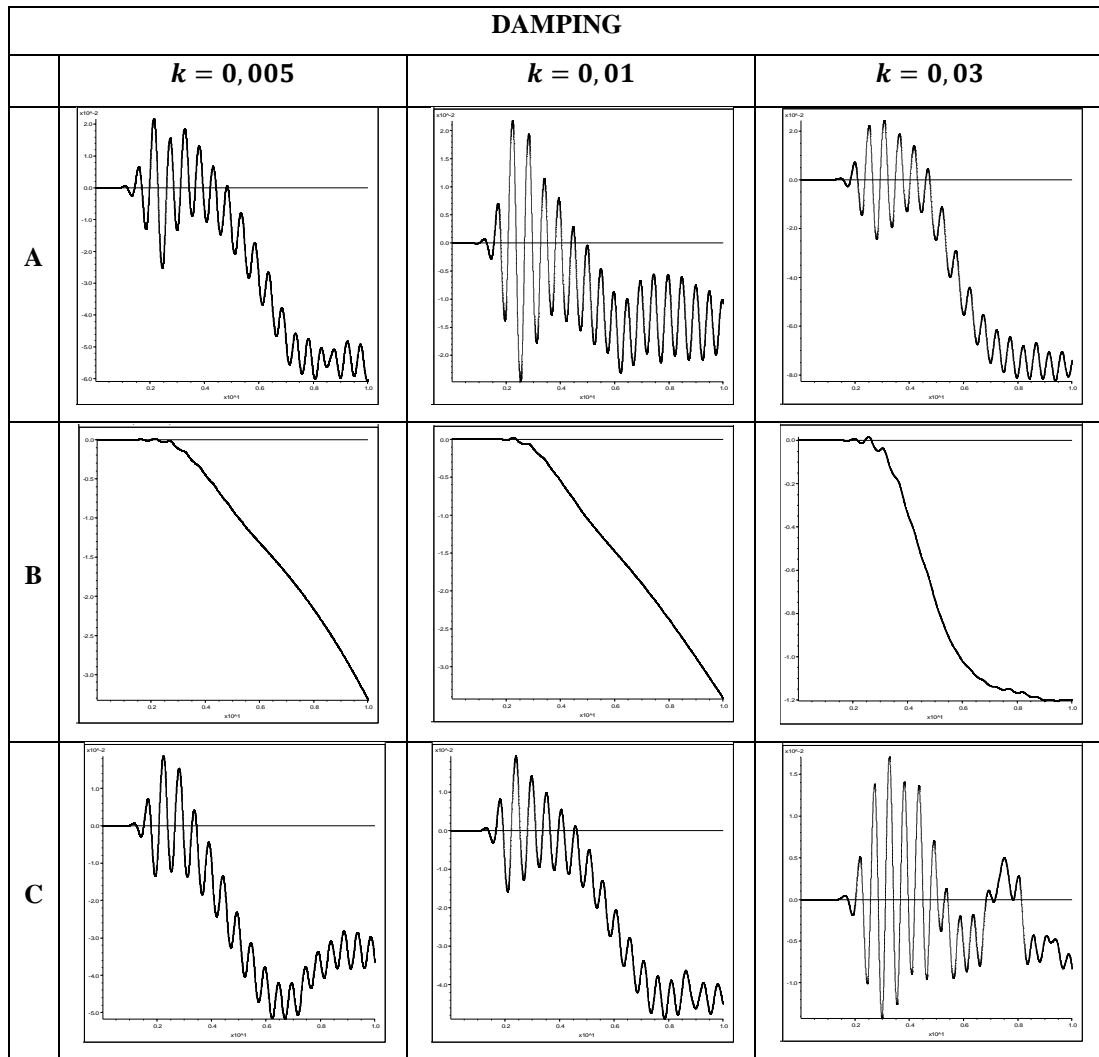
Figure 4.17 - *Graphics of x-displacements of the three monitoring points A, B and C for the three different values of parameter k. Analysis with 2% of damping.*

Observing the displacements of the three monitoring points it is possible to draw the same conclusion as before. The displacements of the case with $\kappa = 0,01$ are larger than those of the case with $\kappa = 0,03$ which is the case with the frequencies of the model closest to the frequency of the input wave.

4.4 Sensitivity analysis of the model, isotropic structuration factor S_i

The last sensitivity test was about the parameter S_i (Structuration factor). The three analyses with the three different values of κ are considered again. For each value of κ four analyses are made changing the value of S_i. The four different values of S_i considered are: 3,0 , 2,5, 2,0, 1,0. A value of S_i equal to 1,0 means the absence of structuration of the clay, while values of $S_i > 1$ means the presence of structuration. In this sensitivity analysis are considered the two cases with and without damping and the results (final displacements) are shown in *Figure 4.18 and 4.19.*
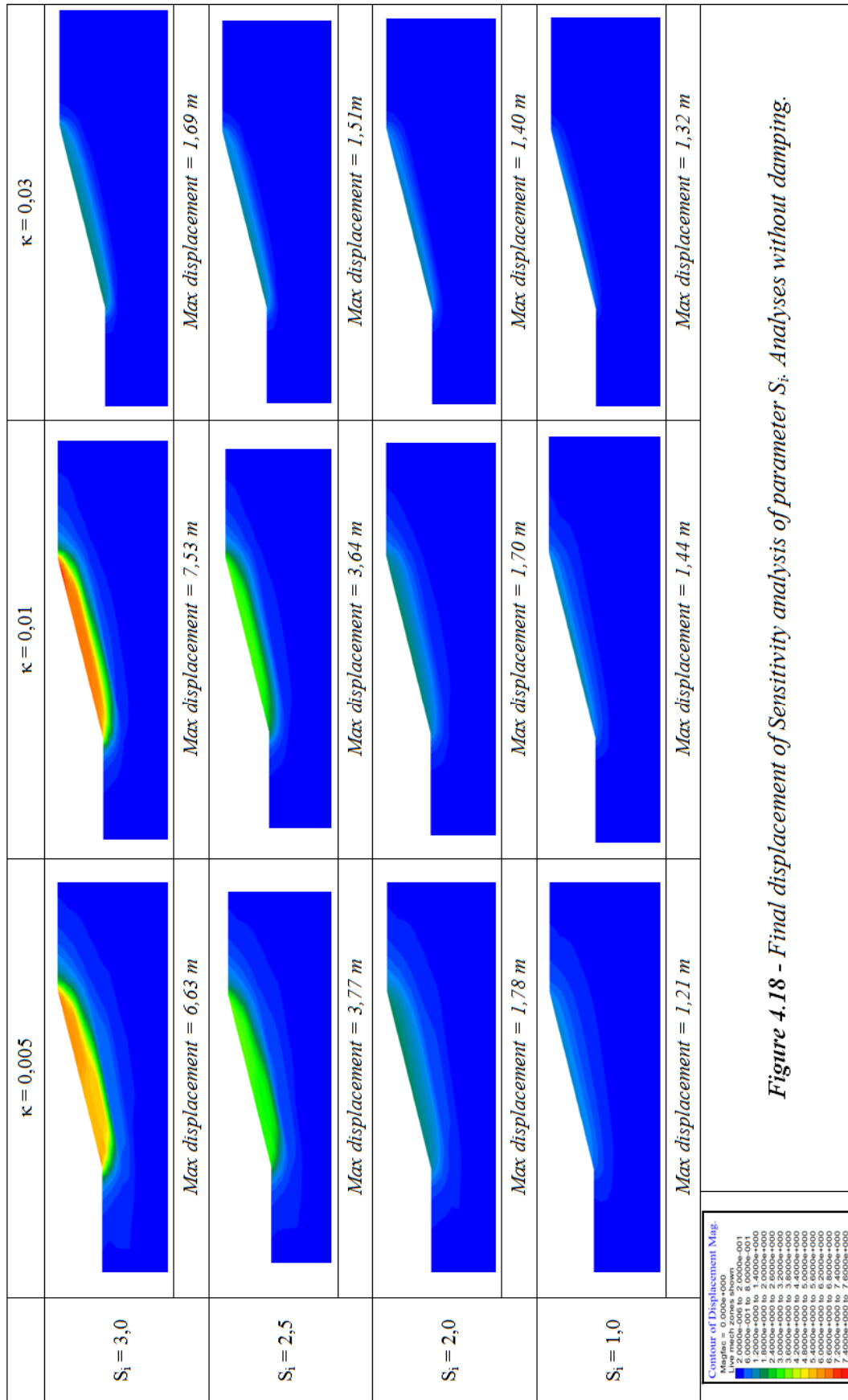
Figure 4.18 - Final displacement of Sensitivity analysis of parameter S_i. Analyses without damping.
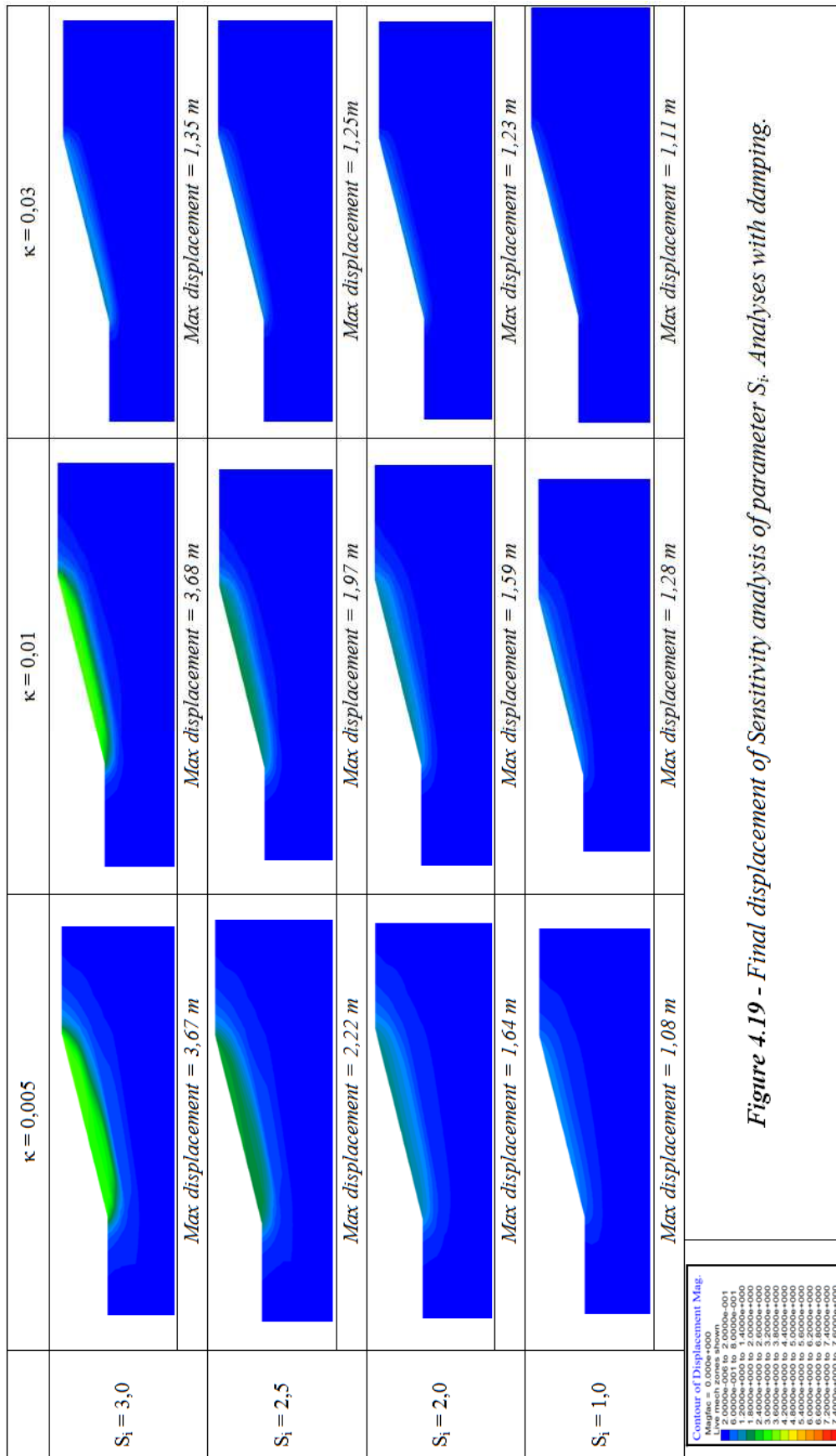
Figure 4.19 - Final displacement of Sensitivity analysis of parameter S_i. Analyses with damping.

From these results, focusing on the more realistic case with the presence of damping, it is possible to conclude that in the absence of structuration ($S_i = 1$) the displacements are smallest. The presence of structuration ($S_i > 1$) increase clearly the displacement. About the parameter κ, for the cases considered, it is not easy to draw a conclusion; more tests on sensitivity analysis for this parameter may help elucidate the role of this parameter.

Chapter 5 – Effects of the three-dimensionality

The goal of this chapter is to investigate the importance of considering the three-dimensionality in the dynamic response of slopes. To this end, a three-dimensional geometry is created and on this geometry it is performed an extensive sensitivity analysis. Moreover, in order to quantify the effect of three dimensionality, the results of the three-dimensional simulations are compared with those obtained for the corresponding two-dimensional model.

5.1 Geometry of the model

The three-dimensional geometry of the model is shown *Figure 5.1*. In this model there are slopes in the two directions as follows: the main slope, in the *x*-direction (direction of the dynamic input), identified by α angle and the second slope, in *y*-direction, defined by β angle. The presence of this second slope is the main aspect that permits to observe the effects of the three-dimensionality in the dynamic response of the model.

One of the parameters in the sensitivity analysis is the inclination of the slope. The angles of the two slopes are allowed vary in a way that the ratio between the vertical size and the horizontal size of the slope take on the values of 1:4, 1:5 or 1:6. For example, considering the main slope, the difference of height is constant and equal to 10m, so the three different horizontal measures to have the right ratios are: 40 m, 50m, 60m. In presenting the results in this chapter the different inclinations of the slopes will be indicated with α 1:4, α 1:5, α 1:6 for the main slope, and β 1:4, β 1:5, β 1:6 for the secondary slope.
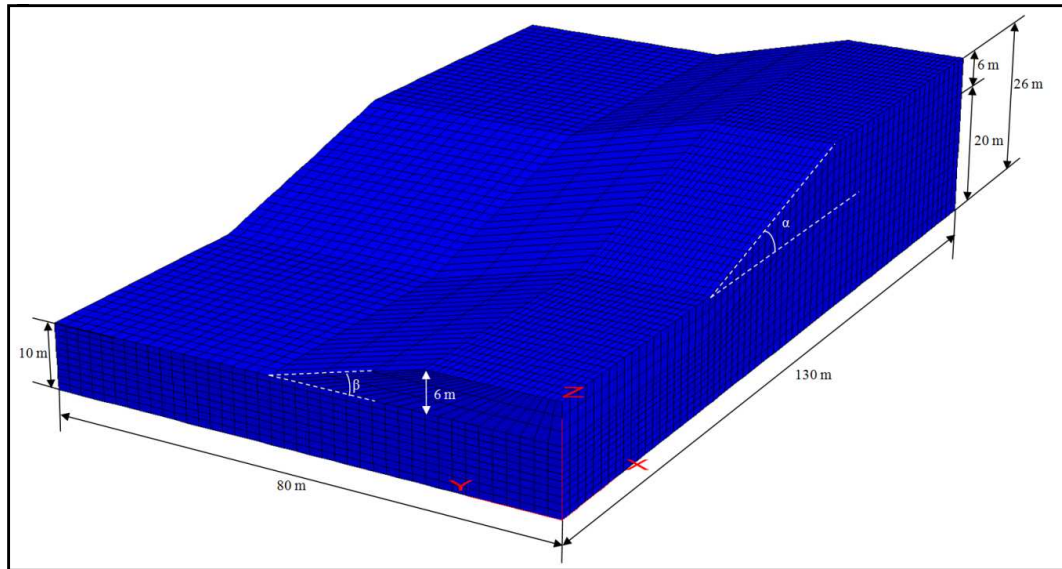
Figure 5.1 - *Geometry of the model.*

5.2 Material properties

An undrained clay is chosen for the numerical simulation and the Mohr-Coulomb constitutive model is adopted. In the depth range from *0 m* to *10 m* the material parameters are varied linearly, while in the highest part of the model the material is considered homogeneous. The values adopted in the homogeneous upper part are:

Cohesion: $c = 25{,}0\ kPa$

Shear modulus: $G = 1000 \cdot c = 25000\ kPa$

Bulk: $K = \frac{2G(1+\nu)}{3(1-2\nu)} = 241666{,}7 kPa$ with: $\nu = 0{,}45$

Internal angle of friction: $\varphi = 0{,}0°$

Dilation angle: $\psi = 0{,}0°$

Tension limit: is given a very large tension cut off to avoid failure in tension

Density : $\rho = 2000\ \frac{kg}{m^3}$

In the lower part of the model (from *0 m* to *10 m*), where it has been decided to take the properties non-homogeneous, the relations adopted are shown in Figure 5.2
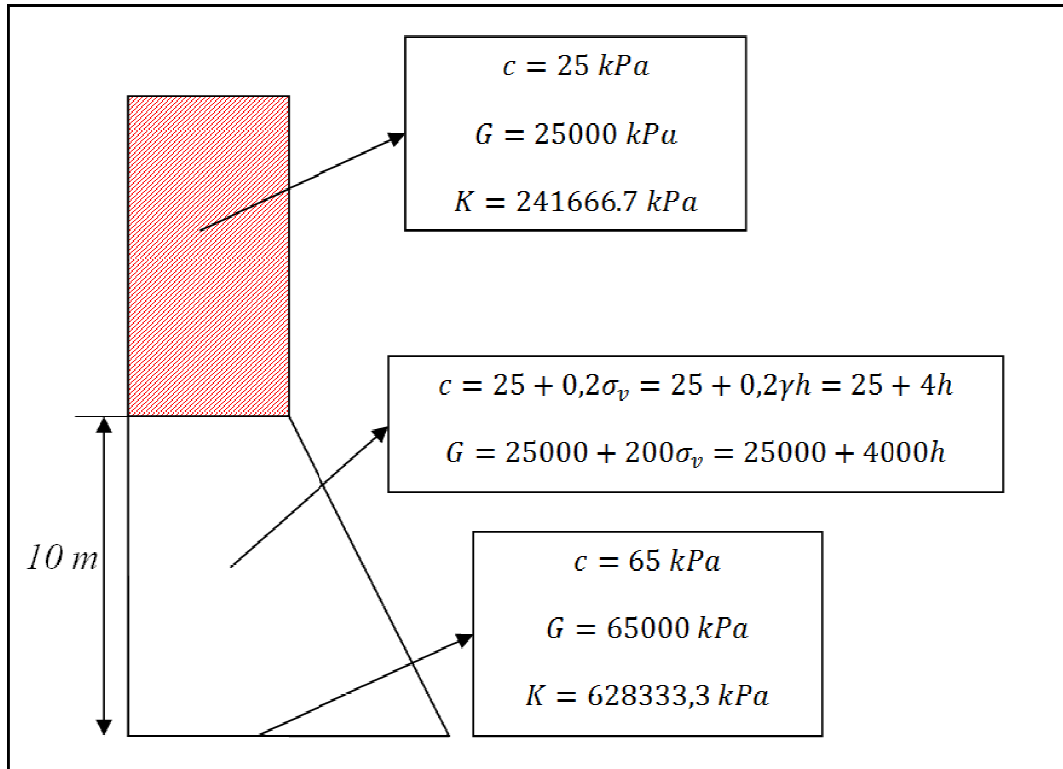
Figure 5.2 - *Variation of material parameters with depth.*

To make the properties vary with the depth, the function *gradient* was uses, adopting variation per meter equal to *4* for the cohesion, *4000* for the shear modulus and *38666,67* for the bulk modulus. The variation of one material parameter (shear modulus *G*) with the depth is show in *Figure 5.3*.
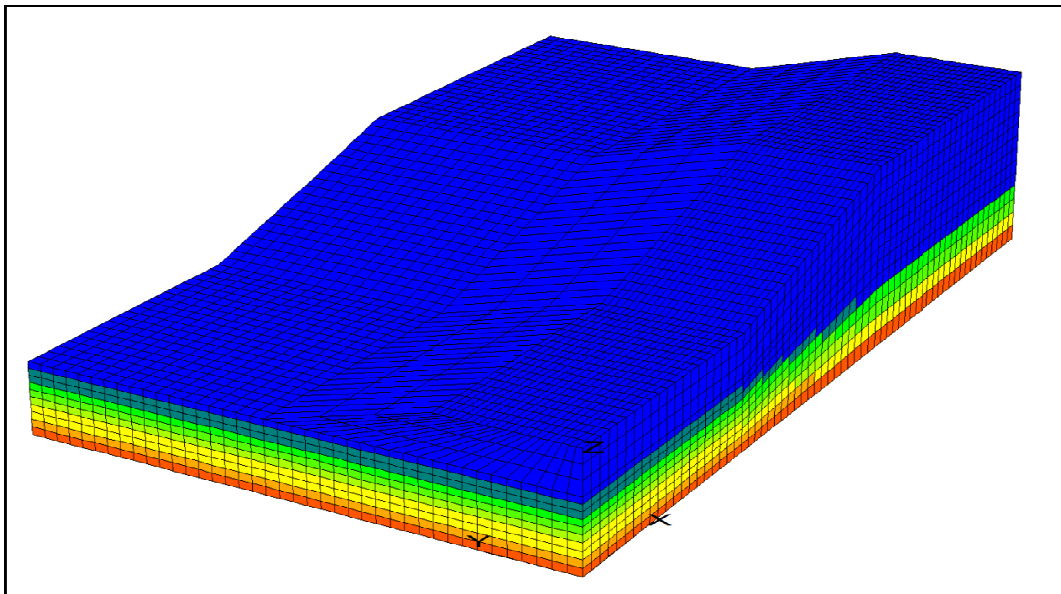
Figure 5.3 - *Variation of shear modulus G with depth.*

5.3   Dynamic input

For simplicity and better interpretation of the results a sinusoidal wave with the following expression has been used:

$$\dot{u} = -\frac{a}{\omega}\cos{(\omega t)}$$
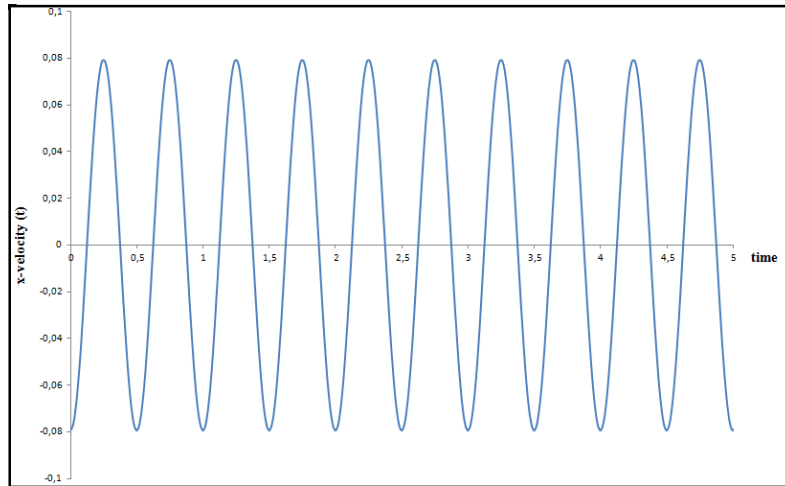
Figure 5.4 *- Dynamic input.*

In this way the acceleration and the displacements are sinuisoidal functions beginning from zero and expressed as follows.

$$u = -\frac{a}{\omega^2}\sin{(\omega t)}$$

$$\ddot{u} = a\sin{(\omega t)}$$

The dynamic input is specified as a velocity time history in the *x*-direction and is applied at the bottom of the model (see *Figure 5.5*).
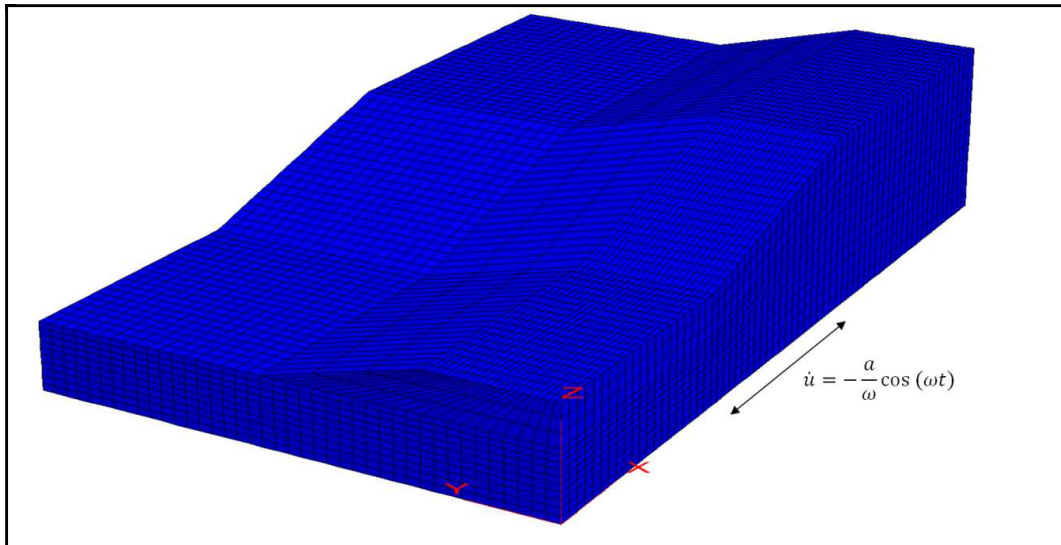
Figure 5.5 - Direction of the dynamic input.

Free field boundary conditions are adopted as shown in *Figure 5.6*.
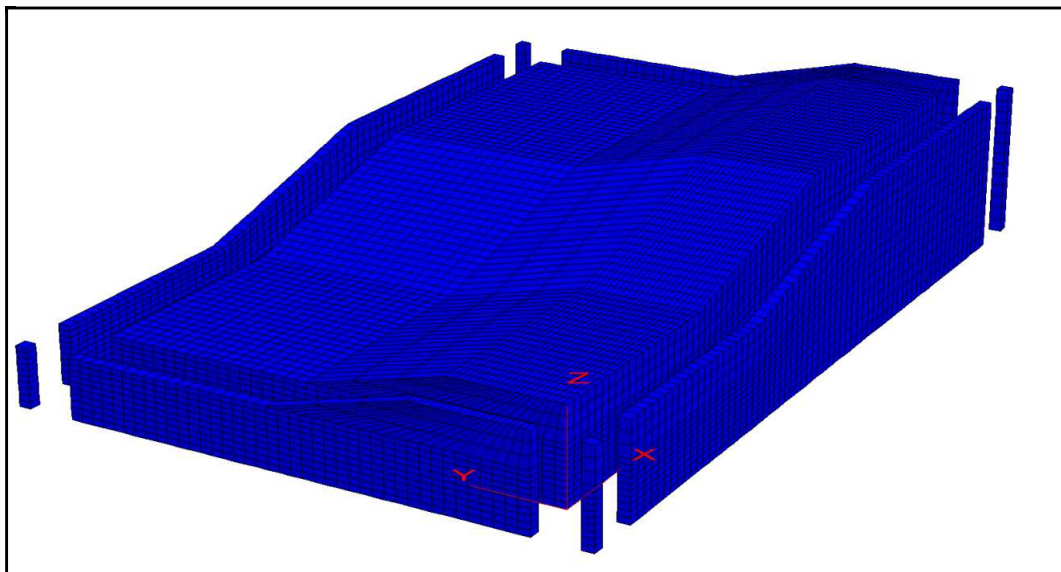
Figure 5.6 - Free field boundary condition.

5.4 Sensitivity analysis

Using this three-dimensional geometry an extensive sensitivity analysis has been performed on the following parameters: earthquake frequency, peak acceleration, and the angles of the two slopes. The different combinations are resumed from *Table 5.1* to *Table 5.3*.

FREQUENCY 2.0 Hz								
α 1:4			α 1:5			α 1:6		
β 1:4	β 1:5	β 1:6	β 1:4	β 1:5	β 1:6	β 1:4	β 1:5	β 1:6
0.1g	0.1g	0.1g	0.1g	0.1g	0.1g	0.1g	0.1g	0.1g
0.15g	0.15g	0.15g	0.15g	0.15g	0.15g	0.15g	0.15g	0.15g
0.2g	0.2g	0.2g	0.2g	0.2g	0.2g	0.2g	0.2g	0.2g

(first column label: peak acceleration)

Table 5.1 - *Analyses made with frequency of 2.0 Hz*

FREQUENCY 3.0 Hz	
	α 1:5
	β 1:5
	0.1g
peak acceleration	0.15g
	0.2g

Table 5.2 - *Analyses made with frequency of 3.0 Hz*

FREQUENCY 5.0 Hz	
	α 1:5
	β 1:5
	0.1g
peak acceleration	0.15g
	0.2g

Table 5.3 - *Analyses made with frequency of 5.0 Hz*

Some representative cases of the sensitivity analysis were chosen to show some key results of the analyses, the cases are:

	Frequency (Hz)	Inclination of main slope	Inclination of the secondary slope	Peak acceleration
Figure 5.7	2.0 Hz	α 1:4	β 1:4	0.15g
	2.0 Hz	α 1:5	β 1:5	0.15g
Figure 5.8	2.0 Hz	α 1:5	β 1:5	0.15g
	3.0 Hz	α 1:5	β 1:5	0.15g
Figure 5.9	2.0 Hz	α 1:5	β 1:5	0.1 g
	3.0 Hz	α 1:5	β 1:5	0.2 g

***Table 5.4** – Summary of the results that are shown in the next figure.*

The results of the total permanent displacements and of the permanent shear strain at the end of the dynamic analyses for these cases are shown in Figure 5.7 to Figure 5.9. The maximum computed values are also listed in these figures for easy comparisons.
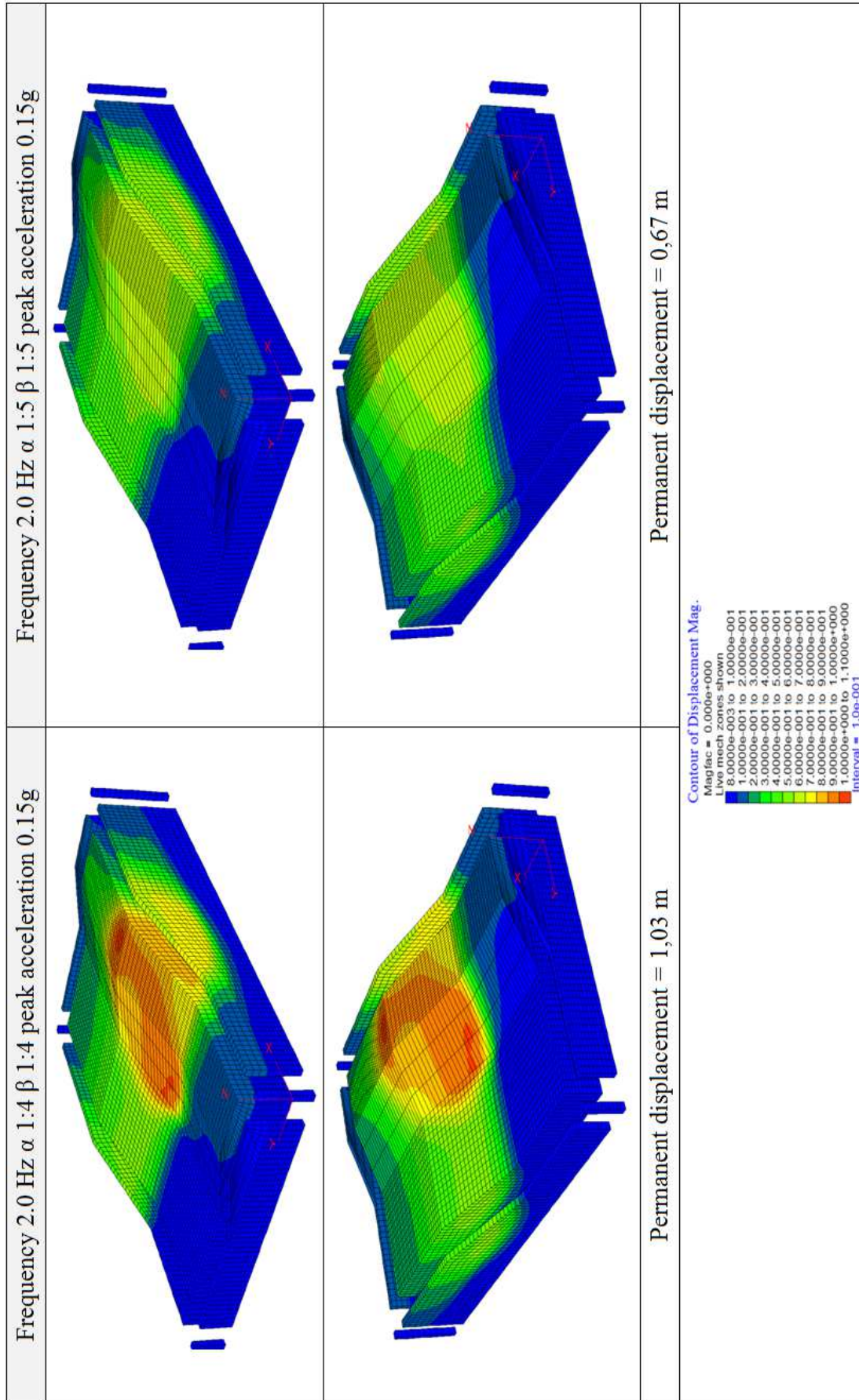
Figure 5. 7 a) *–Permanent displacement, of sensitivity analysis on the angles of the two slopes.*

Frequency 2.0 Hz α 1:5 β 1:5 peak acceleration 0.15g

Permanent shear strain = 8,8%

Frequency 2.0 Hz α 1:4 β 1:4 peak acceleration 0.15g

Permanent shear strain = 10,4%

Contour of Shear Strain Increment
Magfac = 0.000e+000
Live mech zones shown
Gradient Calculation
-4.8000e-002 to -4.0000e-002
-4.0000e-002 to -2.0000e-002
-2.0000e-002 to 0.0000e+000
0.0000e+000 to 2.0000e-002
2.0000e-002 to 4.0000e-002
4.0000e-002 to 6.0000e-002
6.0000e-002 to 8.0000e-002
8.0000e-002 to 1.0000e-001
1.0000e-001 to 1.2000e-001
1.2000e-001 to 1.4000e-001
1.4000e-001 to 1.6000e-001
1.6000e-001 to 1.8000e-001
1.8000e-001 to 2.0000e-001

Figure 5.7 b) –Permanent shear strain, of sensitivity analysis on the angles of the two slopes.
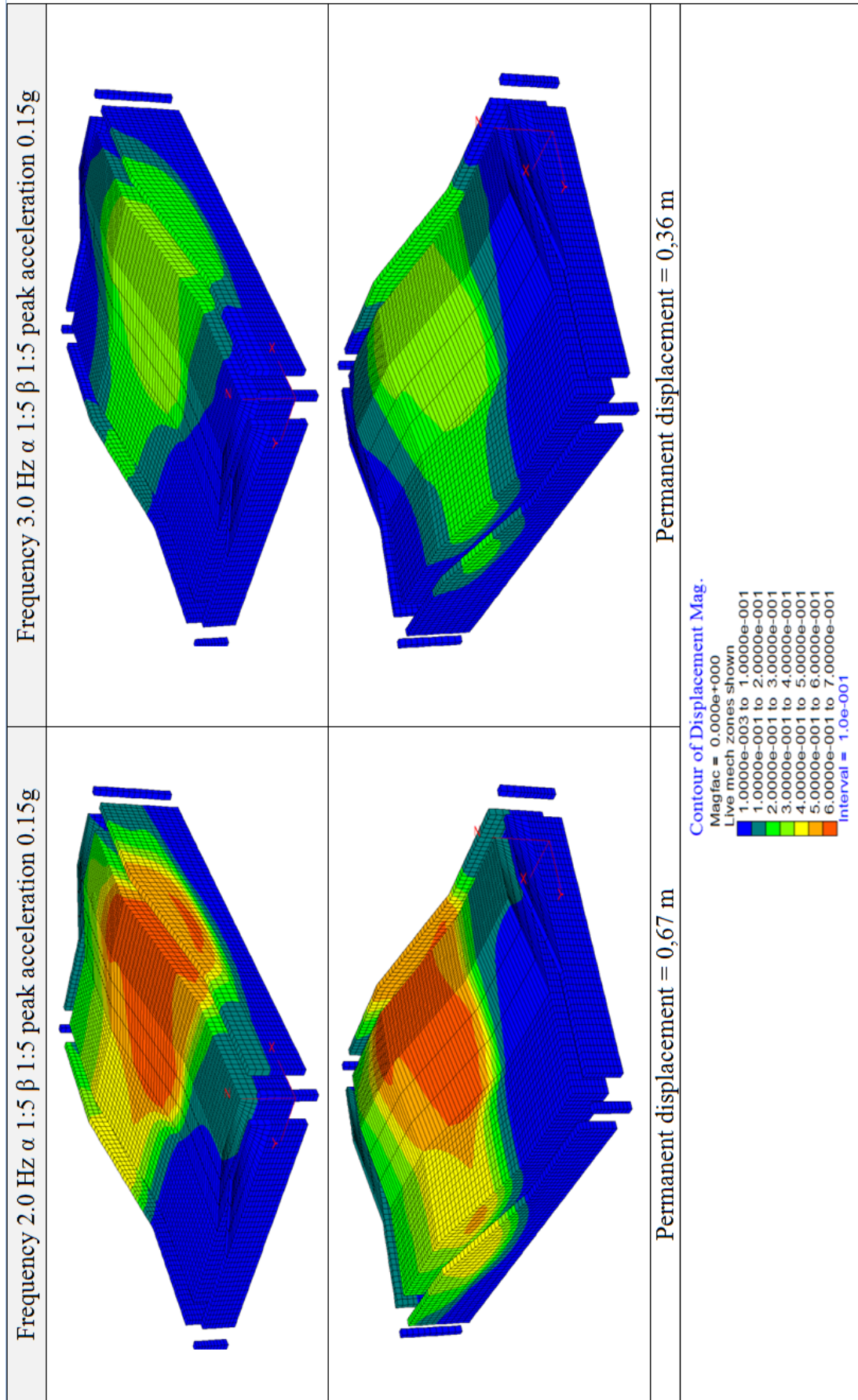
Figure 5.8 a) – Permanent displacement, of sensitivity analysis on frequency of the dynamic input.

Frequency 3.0 Hz α 1:5 β 1:5 peak acceleration 0.15g

Permanent shear strain = 5,6%

Frequency 2.0 Hz α 1:5 β 1:5 peak acceleration 0.15g

Permanent shear strain = 8,8%

Contour of Shear Strain Increment
Magfac = 0.000e+000
Live mech zones shown
Gradient Calculation

-4.7000e-002 to -4.0000e-002
-4.0000e-002 to -2.0000e-002
-2.0000e-002 to 0.0000e+000
0.0000e+000 to 2.0000e-002
2.0000e-002 to 4.0000e-002
4.0000e-002 to 6.0000e-002
6.0000e-002 to 8.0000e-002
8.0000e-002 to 1.0000e-001
1.0000e-001 to 1.2000e-001
1.2000e-001 to 1.4000e-001
1.4000e-001 to 1.6000e-001
1.6000e-001 to 1.8000e-001
1.8000e-001 to 2.0000e-001

Figure 5.8 b) –Permanent shear strain, of sensitivity analysis on frequency of the dynamic input.
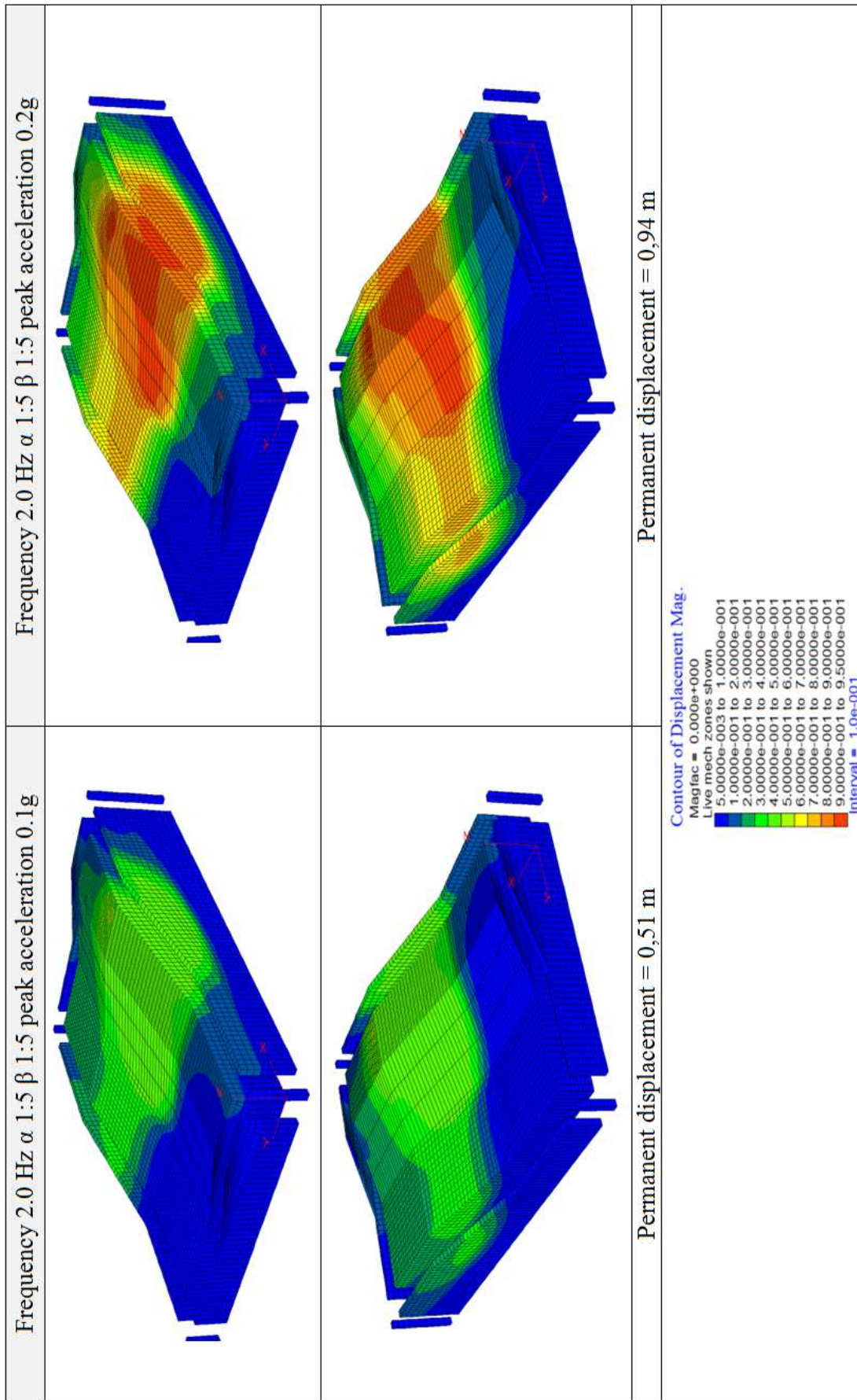
Figure 5.9 a) – Permanent displacement, of sensitivity analysis on peak acceleration.
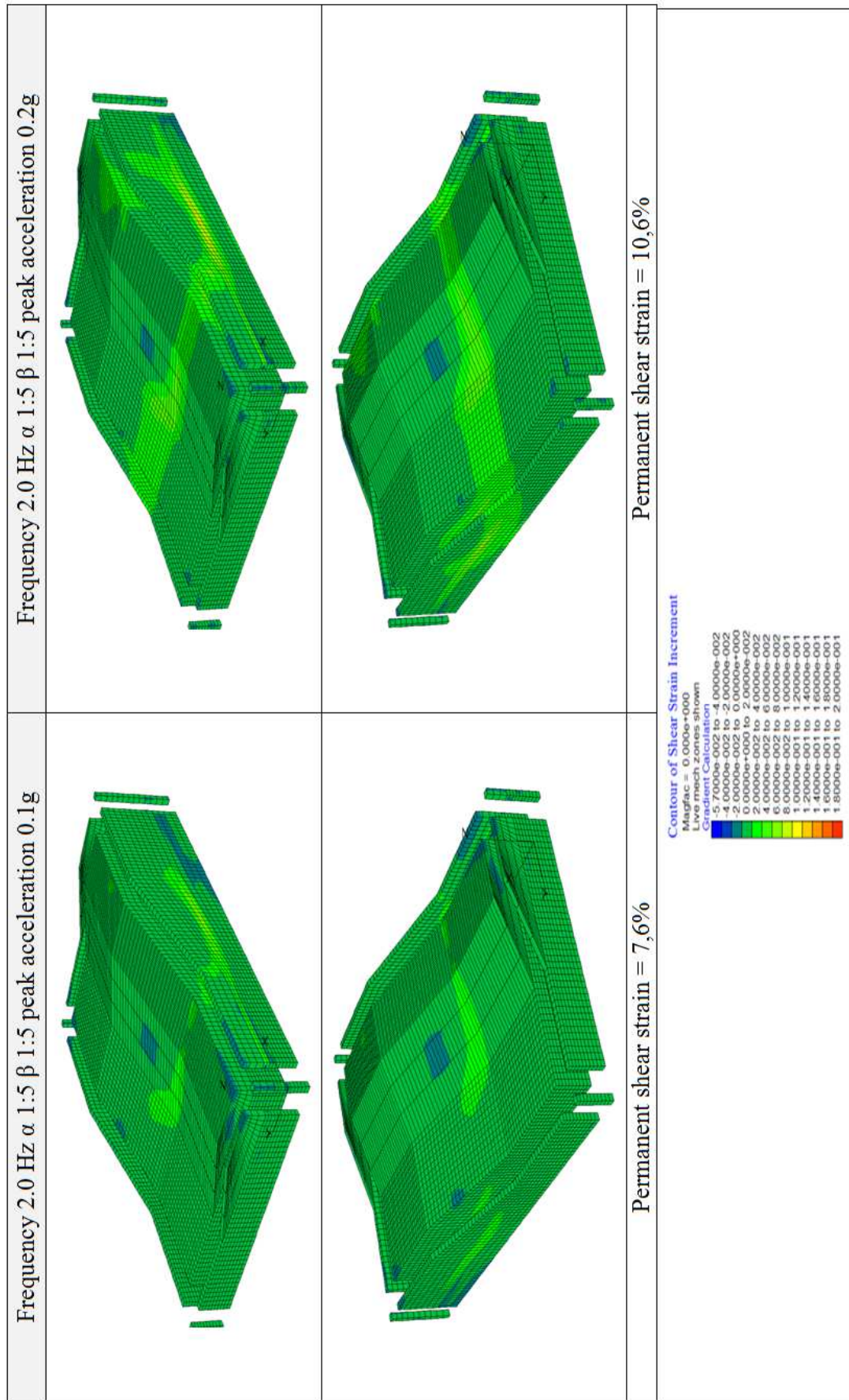
Figure 5.9 b) –Permanent shear strain, of sensitivity analysis on peak acceleration.

Another interesting thing is to show the results of displacements separately in the horizontal and vertical directions. These results are shown in Figure 5.10 and they are referred to one significant case with the following parameters.

Frequency (Hz)	Inclination of main slope	Inclination of the secondary slope	Peak acceleration
2.0 Hz	α 1:5	β 1:5	0.15g

Permanent *x*-displacement

Permanent *y*-displacement

Permanent *z*-displacement
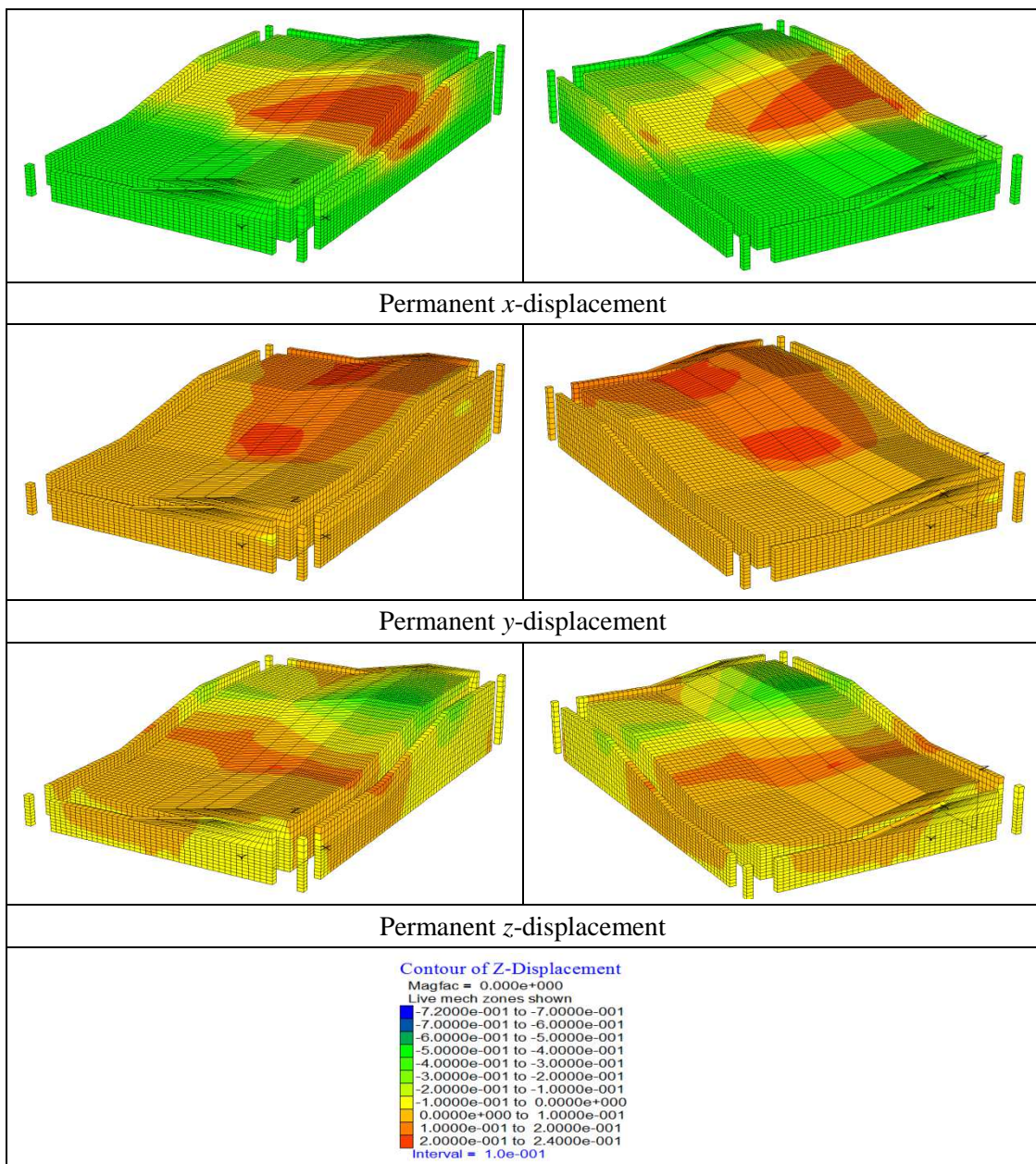
Figure 5.10 - *Results of permanent displacements separately in the horizontal and vertical directions*

In Figure 5.12 are shown plots of horizontal displacements in excitation direction of three monitoring points A, B, C lying on the slope (see Figure 5.11).
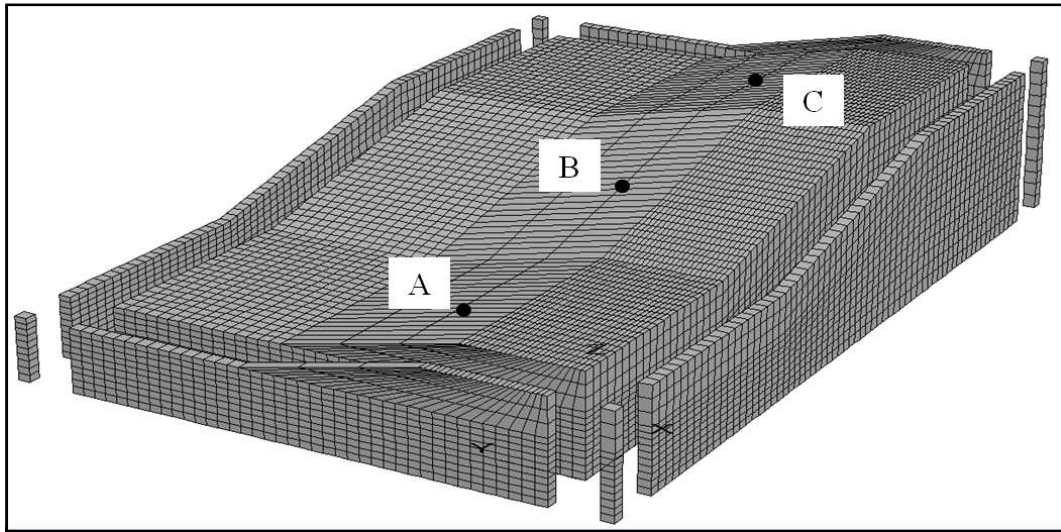
Figure 5.11 - *Position of the monitoring points.*

Time history of permanent *x*-displacement of points A

Time history of permanent *x*-displacement of points B

Time history of permanent *x*-displacement of points C
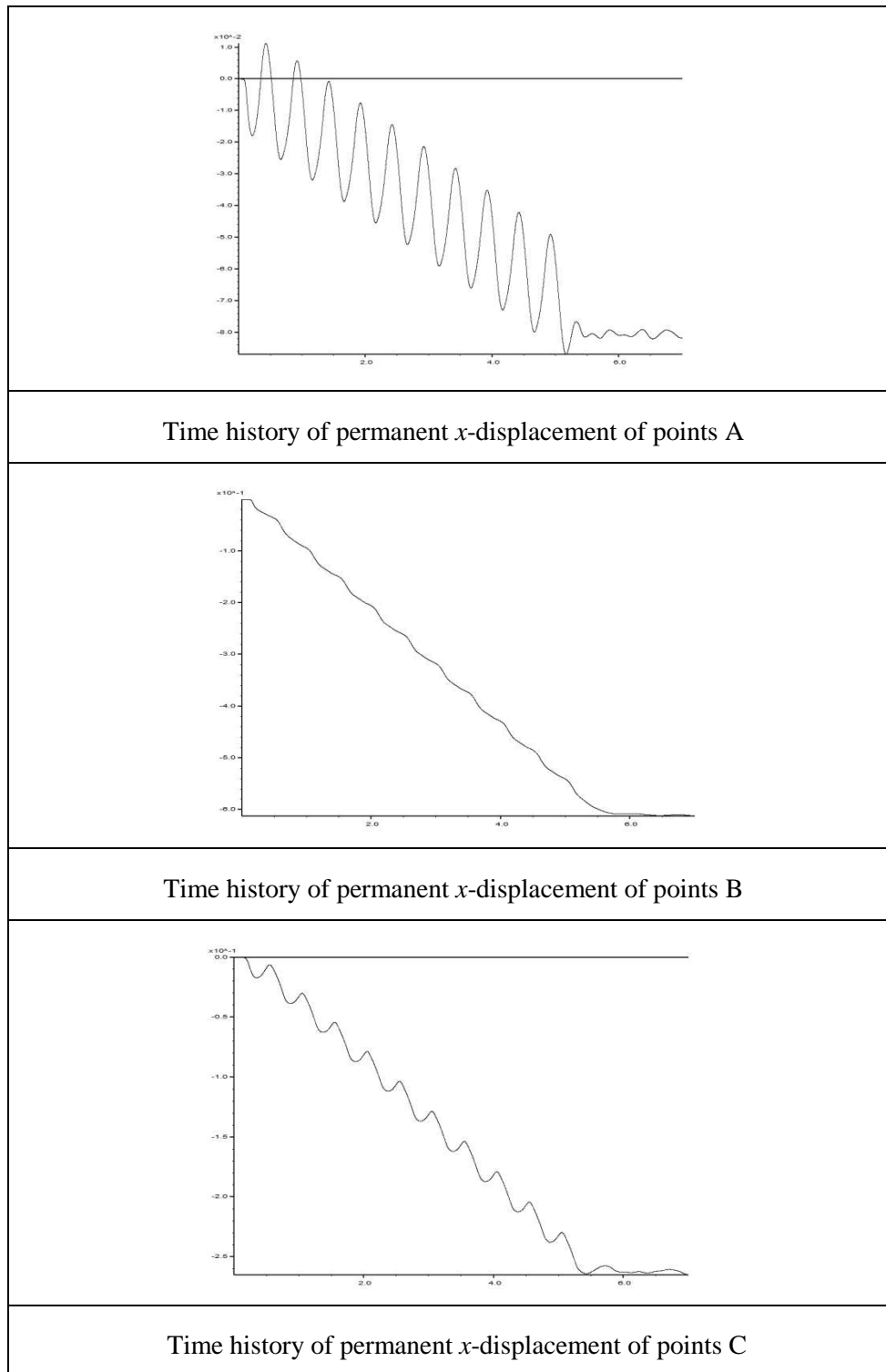
Figure 5.12 - *Plots of permanent horizontal displacements in excitation*

direction

The following table summarizes the results of all the analyses. The results include the permanent displacements and shear strains.

FREQUENCY 2.0 Hz

| | α 1:4 | | | | | | α 1:5 | | | | | | α 1:6 | | | | | |
| | β 1:4, 14° | | β 1:5, 11,3° | | β 1:6, 9,46° | | β 1:4 | | β 1:5 | | β 1:6 | | β 1:4 | | β 1:5 | | β 1:6 | |
Peak acc.	max. Disp. [m]	max. Strain [%]	max. Disp [m]	max. Strain [%]	max. Disp. [m]	max. Strain [%]	max. Disp. [m]	max. Strain [%]	max. Disp. [m]	max. Strain [%]	max. Disp. [m]	max. Strain [%]	max. Disp. [m]	max. Strain [%]	max. Disp. [m]	max. Strain [%]	max. Disp. [m]	max. Strain [%]
0.1g	0,84	10,36	0,73	9,74	0,67	9,02	0,56	7,72	0,51	7,56	0,49	7,44	0,45	7,42	0,423	7,43	0,416	7,44
0.15g	1,03	11,13	0,91	10,42	0,84	9,68	0,74	8,98	0,68	8,80	0,675	8,66	0,63	9,23	0,593	9,34	0,589	9,36
0.2g	1,31	13,03	1,18	12,10	1,11	11,44	1,01	10,90	0,94	10,62	0,93	10,44	0,89	11,56	0,853	11,60	0,847	11,55

FREQUENCY 3.0 Hz

| | α 1:5 / β 1:5 | |
Peak acc.	max. Displacement [m]	max.Strain [%]
0.1g	0,24808	4,3273
0.15g	0,36011	5,626
0.2g	0,50841	6,562

FREQUENCY 5.0 Hz

| | α 1:5 / β 1:5 | |
Peak acc.	max. Displacement [m]	max.Strain [m]
0.1g	0,080346	0,79878
0.15g	0,12303	1,246
0.2g	0,18866	2,0702

127

Figure 5.13 to Figure 5.16 presents the results in graphic form. The results are presented against different parameters to highlight the influence of the parameters.
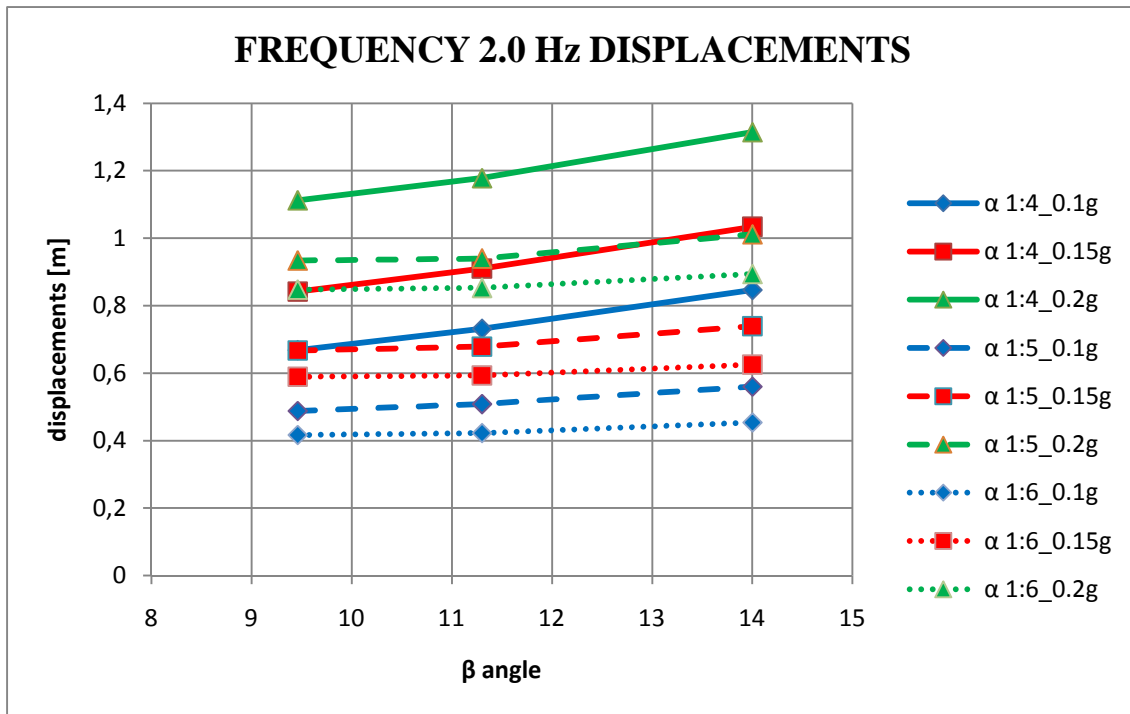
Figure 5.13 *– Permanent displacements in graphic form of the sensitivity analysis.*
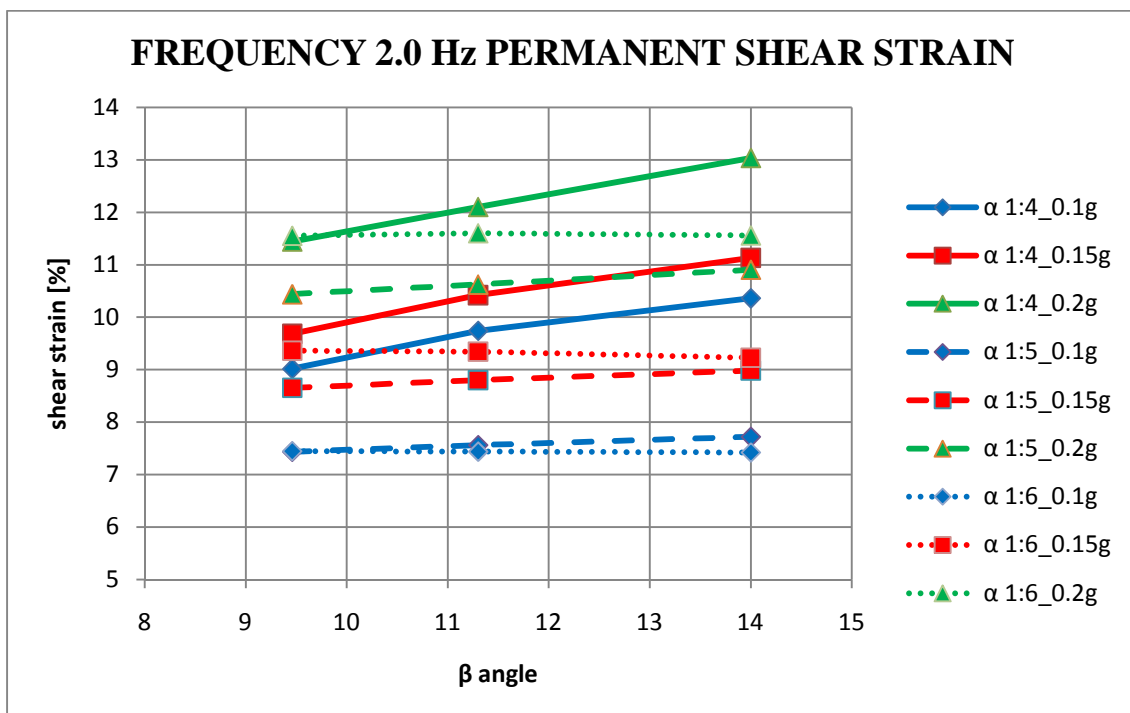
Figure 5.14 *– Permanent shear strain in graphic form of the sensitivity analysis.*
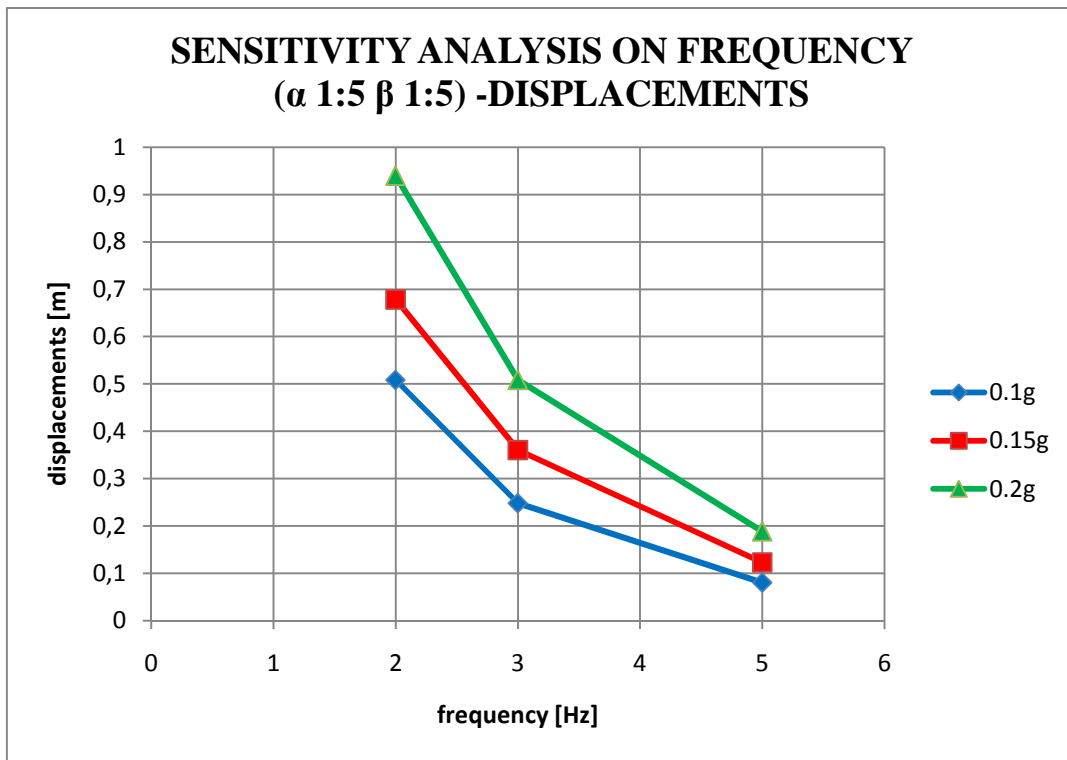
Figure 5.15 – *Permanent displacements in graphic form of sensitivity analysis on frequencies.*
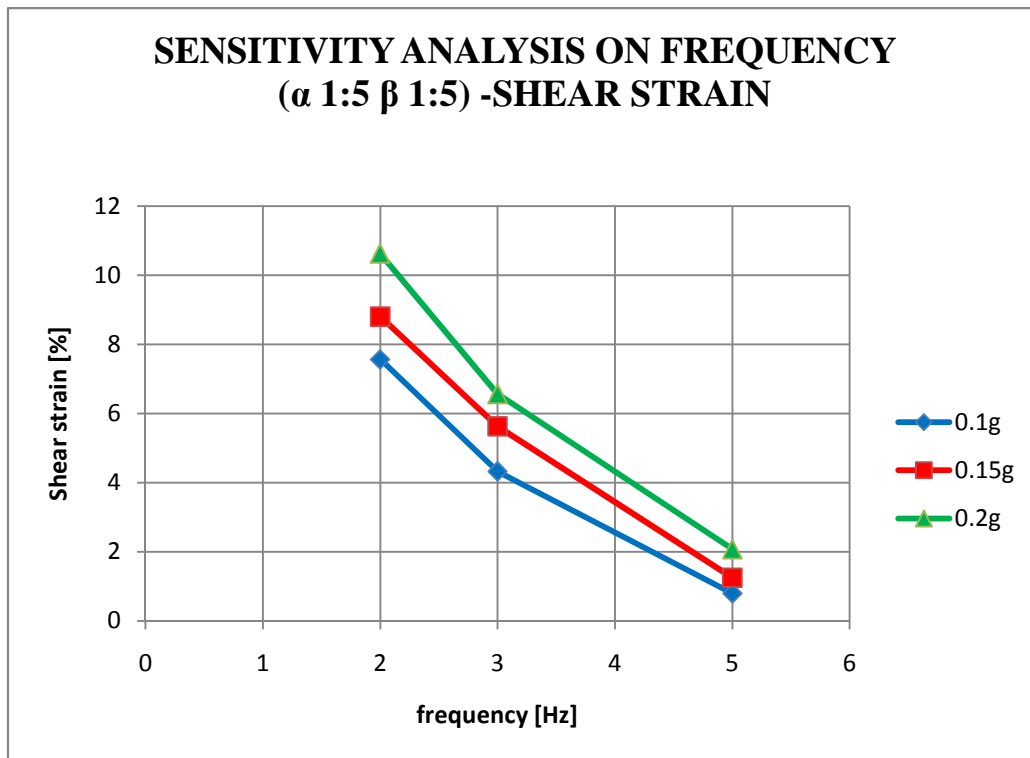
Figure 5.16 - *Permanent shear strain in graphic form of sensitivity analysis on frequencies.*

Considering the results for the displacements, it is clear that the models work well, because, as expected, by increasing the peak acceleration or the inclination of the slope one obtains increase in the displacements. Considering the sensitivity analysis on the frequency, the large values of displacement occurs for a frequency of 2 Hz. This is explainable because this frequency is fairly close to the natural frequency of the soil model.

5.5 2D vs. 3D

In this section, the results of some of the cases of three-dimensional simulations are compared with the results obtained with the corresponding two-dimensional model in order to quantify the effect of three-dimensionality. The cases considered are described in Table 5.5:

	Frequency (Hz)	Inclination of main slope	Inclination of the secondary slope	Peak acceleration
Case 1	2.0 Hz	α 1:4	β 1:4	0.15g
Case 2	2.0 Hz	α 1:5	β 1:5	0.15 g
Case 3	5.0 Hz	α 1:5	β 1:5	0.15 g

Table 5.5 - *Summary of the significant cases considered.*

Then for the two-dimensional simulations, three different geometries are prepared; each one corresponding to a longitudinal section normal to the secondary slope of the three-dimensional model (see Figure 5.17).

3D - section 1: y = 20 m	2D - model a)
3D - section 2: y = 35 m	2D - model b)
3D - section 3: y = 50 m	2D - model c)
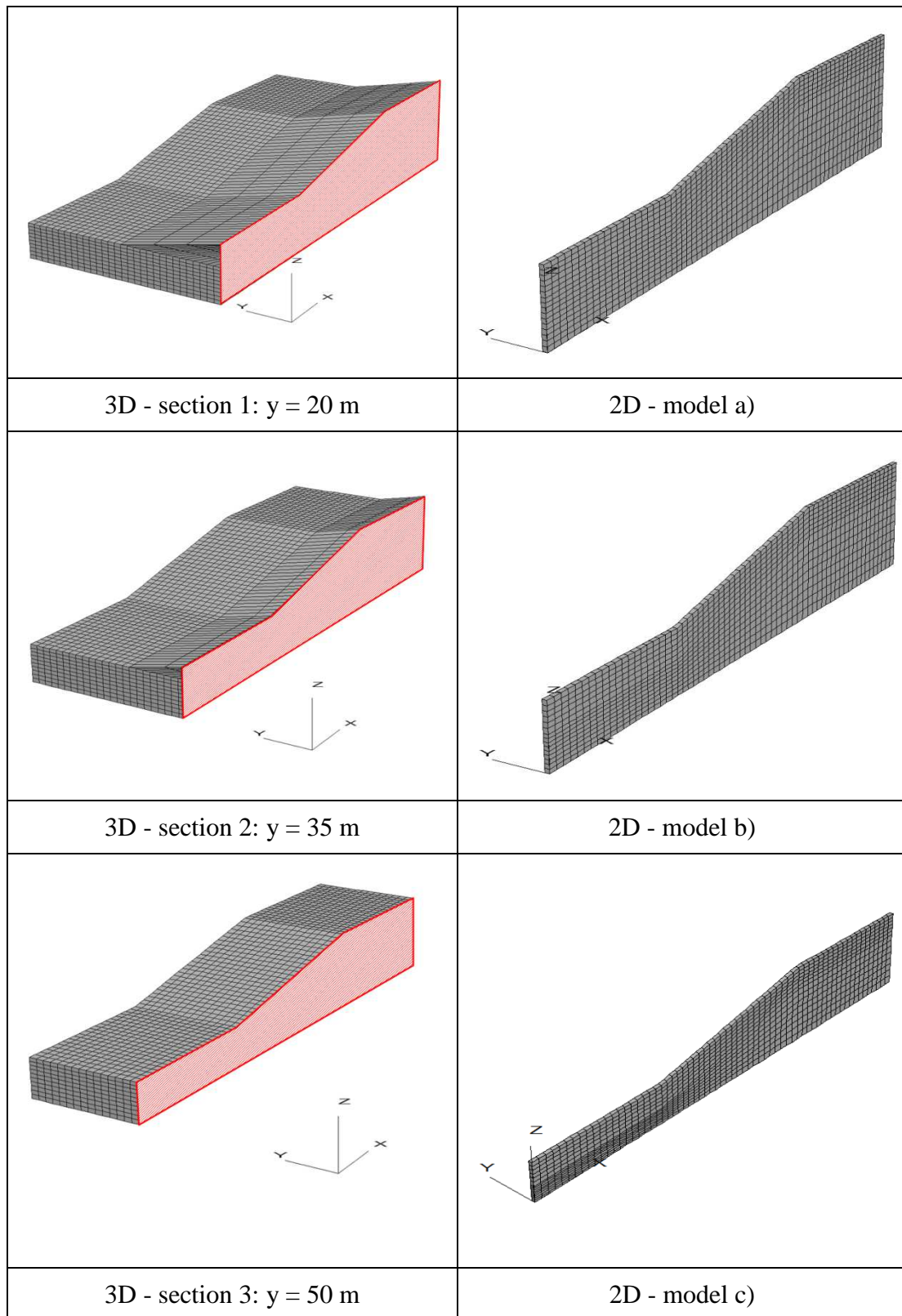
Figure 5.17 *–Sections of the three-dimensional model and corresponding two-dimensional model.*

The comparison between the results of the sections of the three-dimensional models and the corresponding two-dimensional models are shown in Figure: 5.18 to Figure 5.20:

Case 1 : Frequency: 2.0 Hz ; α 1:4; β 1:4; peak acceleration: 0.15g	
3D section	2D models
Max. displacement = 1,043 m	Max. displacement = 0,850 m
Max. displacement = 1,041 m	Max. displacement = 0,694
Max. displacement = 1,009 m	Max. displacement = 0,532

Figure 5.18 a) – *Permanent displacements, case 1*

Case 1 : Frequency: 2.0 Hz ; α 1:4; β 1:4; peak acceleration: 0.15g	
3D sections	2D models
Max permanent shear strain = 9,03%	Max permanent shear strain = 9,72%
Max permanent shear strain = 9,29%	Max permanent shear strain = 8,16%
Max permanent shear strain = 10,00%	Max permanent shear strain = 5,34%
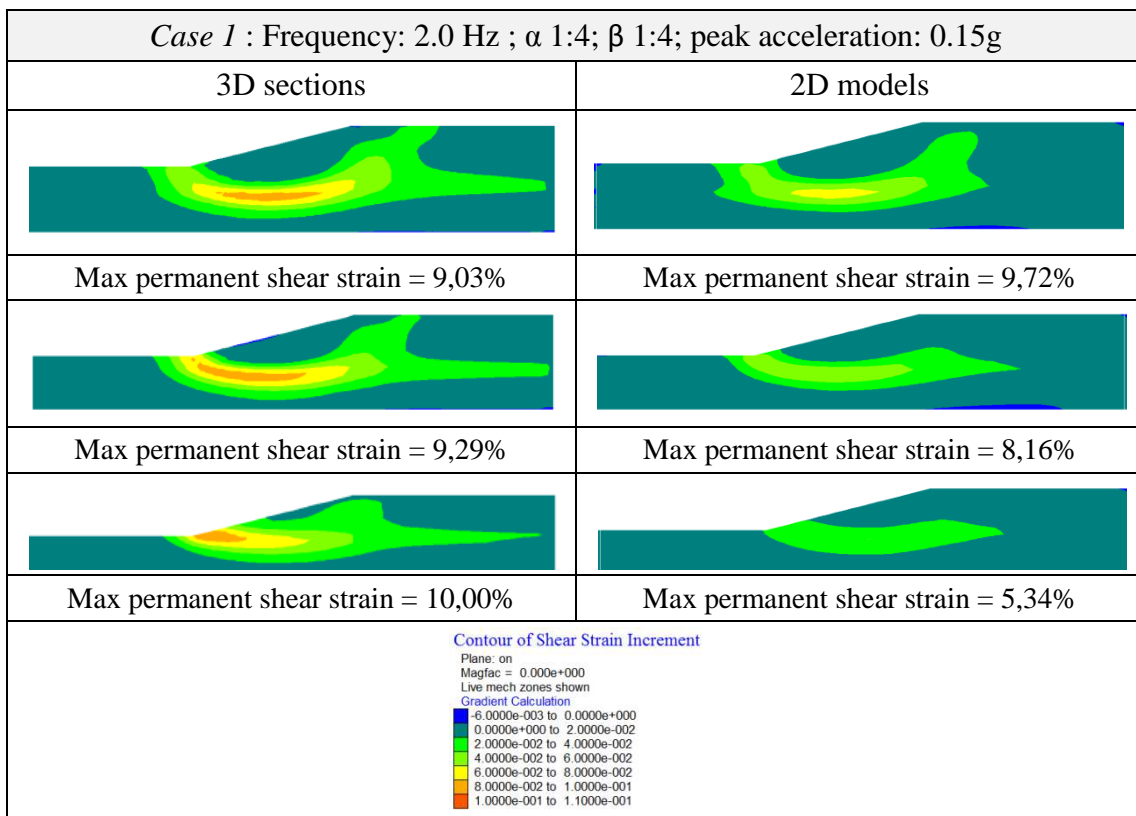
Figure 5.18 b) –*Permanent shear strain, case 1*

133

Case 2 : Frequency: 2.0 Hz ; α 1:5; β 1:5; peak acceleration 0.15g	
3D section	2D models
Max. displacement = 0,693 m	Max. displacement = 0,677 m
Max. displacement = 0,682 m	Max. displacement = 0,586
Max. displacement = 0,650 m	Max. displacement = 0,496
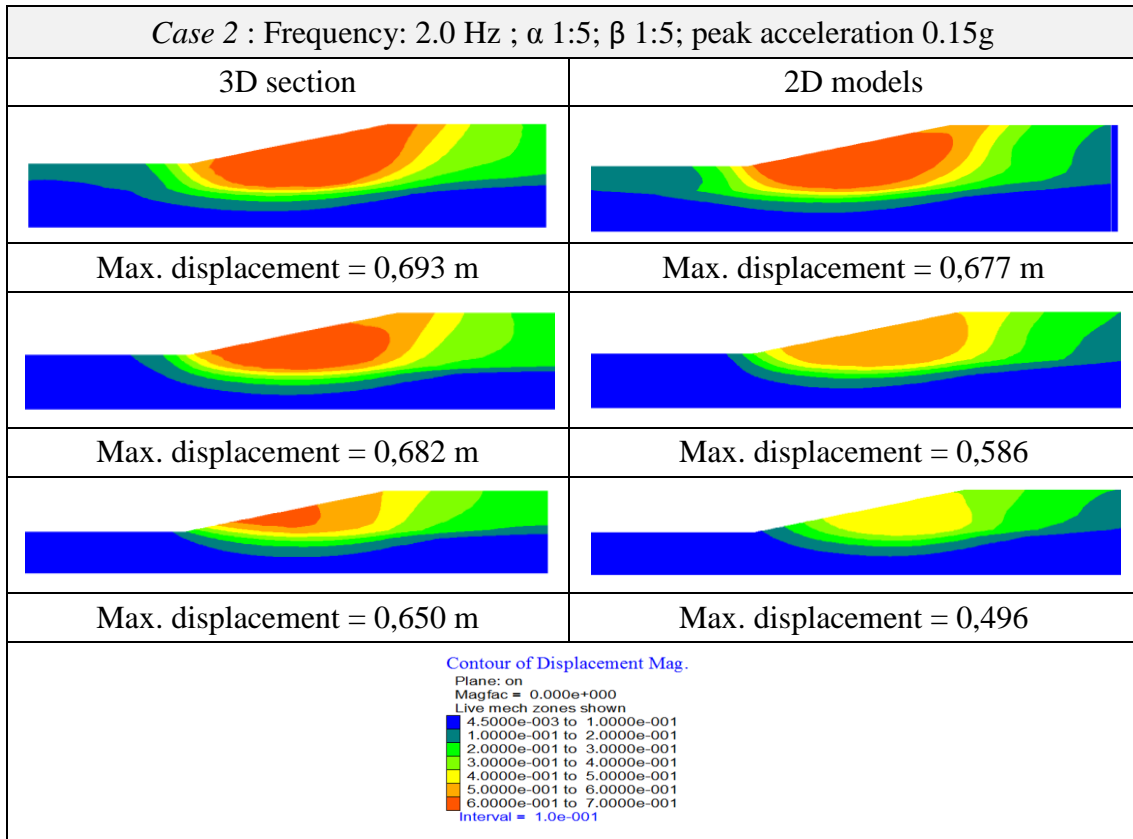
Figure 5.19a) – Permanent displacements, case 2

Case 2 : Frequency: 2.0 Hz ; α 1:5; β 1:5; peak acceleration 0.15g	
3D sections	2D models
Max permanent shear strain = 5,71%	Max permanent shear strain = 8,93%
Max permanent shear strain = 5,52%	Max permanent shear strain = 7,74%
Max permanent shear strain = 5,16%	Max permanent shear strain = 5,21%
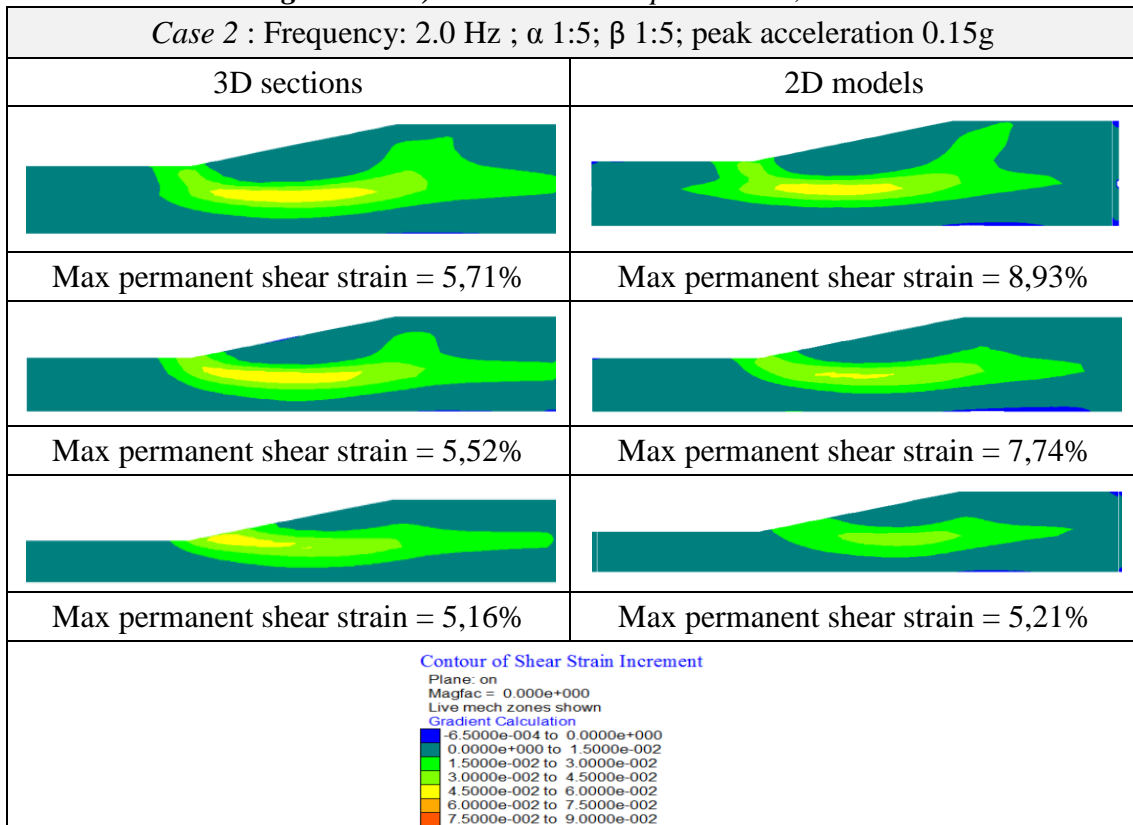
Figure 5.19 b) – Permanent shear strain, case 2

Case 3 : Frequency: 5.0 Hz ; α 1:5; β 1:5; peak acceleration 0.15g	
3D section	2D models
Max. displacement = 0,115 m	Max. displacement = 0,677 m
Max. displacement = 0,106 m	Max. displacement = 0,586
Max. displacement = 0,100 m	Max. displacement = 0,496
Contour of Displacement Mag. Plane: on Magfac = 0.000e+000 Live mech zones shown 4.0000e-005 to 2.0000e-002 2.0000e-002 to 4.0000e-002 4.0000e-002 to 6.0000e-002 6.0000e-002 to 8.0000e-002 8.0000e-002 to 1.0000e-001 1.0000e-001 to 1.2000e-001 Interval = 2.0e-002	

Figure 5.20 a) – *Permanent displacements, case 3*

Case 3 : Frequency: 5.0 Hz ; α 1:5; β 1:5; peak acceleration 0.15g	
3D sections	2D models
Max permanent shear strain = 0,91%	Max permanent shear strain = 1,62%
Max permanent shear strain = 0,87%	Max permanent shear strain = 0,99%
Max permanent shear strain = 0,86%	Max permanent shear strain = 1,53%
Contour of Shear Strain Increment Plane: on Magfac = 0.000e+000 Live mech zones shown Gradient Calculation -3.0000e-004 to 0.0000e+000 0.0000e+000 to 2.0000e-003 2.0000e-003 to 4.0000e-003 4.0000e-003 to 6.0000e-003 6.0000e-003 to 8.0000e-003 8.0000e-003 to 1.0000e-002 1.0000e-002 to 1.2000e-002	

Figure 5.20 b) – *Permanent shear strain, case 3*

From these results it is possible to conclude that three dimensional model gives largest values for displacements and strains. The presence of the secondary slope produces a condition that is more critical than a simple 2D model of the same size. Two-dimensional models obviously fail to capture this feature.

These observations and results indicate that the effects of the three-dimensionality are indeed important. In these case a simple two-dimensional anlaysis could underestimate the effects of the dynamic input. The results of this study can then be used to get an idea of the degree of unconservatism in the 2D results.

Conclusion

The main goal of this research is to understand the role played by the three dimensionality in the earthquake response of slopes and understand the influence of the boundary conditions and material parameters.

The research is performed by using of the software FLAC^{3D}, a three-dimensional explicit non linear finite-difference program for engineering mechanics computation. This software has been chosen because of the possibility to adopt the *free-field boundary condition*, which is a very powerful and effective tool for dynamic analysis of earthquake response.

The first part of this study deals with the principles of the program FLAC^{3D} and how it works. The objective is to master the basic commands and learn special tools to create complicated models, analyze their dynamic behaviour and to understand the differences in the responses by applying different boundary conditions, in particular to understand how the "*free field boundary conditions*" works. Indeed in the numerical analysis of the seismic response, the boundary conditions at the sides of the model must account for the free-field motion that would exist in the absence of the structure. In some cases, elementary lateral boundaries, may be sufficient but should be placed at sufficient distances to minimize wave reflections and achieve free-field conditions. When the material damping is low, the required distance may lead to an impractical model, so an alternative procedure, developed also for FLAC^{3D}, is to "enforce" the free-field motion in such a way that boundaries reproduce non-reflecting proprieties.

During the research, it was observed that this tool always operates in the right way, giving accurate results. An important observation about these boundary conditions is that when "*free field boundary condition*" are applied, the fixities applied on the model in the previous loading stage are deleted only at the boundary of the model. In fact inside the model all the fixities remain unchanged.

In the second chapter, the mono-dimensional dynamic ground response is calculated with analytical methods and with FLAC^{3D}, and the responses are compared. The comparisons are indeed very satisfactory. During this phase it has been noted that care

must be taken about the size of the elements of the mesh. In fact with a largest mesh the results of the numerical simulations are not precisely the same as those of the case with a fine mesh.

In the third chapter of the thesis, the focus has been on the influence of these *free field boundary conditions* in more general models. Considering a two-dimensional simple slope (modeled in FLAC^{3D} with the third-dimension equal to one) some numerical simulations are made by increasing the dimension of the geometry in the *x*-direction, that is, by increasing the distance of the boundary conditions from the slope. In this way it has been possible to find out that also these *free-field boundary conditions* needs some space in order not to influence the results of the dynamic analysis. So at the end of this first part a very good knowledge about use of FLAC^{3D} in this seismic slope stability has been acquired.

The second part of the work is the study of the role of three dimensionality on the dynamic response of slopes. The idea was to adopt as constitutive model for modeling the soil by the SANICLAY model. SANICLAY is a constitutive model based on the well-known isotropic modified Cam Clay model with two additional mechanisms to account for anisotropy and destructuration. SANICLAY is not implemented directly inside FLAC^{3D}, but a few years ago a user-defined subroutine has been written for it to suit FLAC^{3D}. Before applying this model to a three-dimensional geometry some simulations are made to test its performance and its stability. But as it has been described in *Chapter 4*, this model is not quite stable for all conditions. In fact it doesn't work well when the mesh is made very fine. This could be partly due to general problem of implementation of strain-softening models in FE/FD programs. Due to this and other practical issues, it was decided to switch to the Mohr Coulomb constitutive model for the rest of the research.

The last part of the thesis consisted of analyzing the effect of the three dimensionality in the dynamic response of slopes. A three-dimensional geometry is created with two different slopes: one in *x*-direction and the other in the *y*-direction. In order to better interpret the importance of excitation characteristics, the input is chosen as a sinuisodal simple wave, and it has been applied to the bottom of the model as a velocity in the *x*-

direction. In this way the displacements and the acceleration begin from zero, and it's easy to control the parameters useful for the sensitivity analyses. On this geometry it is performed an extensive sensitivity analysis on parameters like: earthquake frequency, peak acceleration, and the angles of the two slopes.

Considering the results of the sensitivity analyses, especially the displacements, it is found that the models work well, because, as expected, by increasing the peak acceleration or the inclination of the slope one obtains larger displacements. Considering the sensitivity analysis on the frequency, the large values of displacement occurs for a frequency of 2 Hz. This is explainable because this frequency is fairly close to the natural frequency of the soil model.

In the last section of the thesis, the results of some of the cases of three-dimensional simulations are compared with the results obtained with the corresponding two-dimensional model in order to quantify the effect of three-dimensionality. For the two-dimensional simulations, three different geometries are prepared; each one corresponding to a longitudinal section normal to the secondary slope of the three dimensional model. From these results it is possible to conclude that three dimensional models give largest values for displacements and strains. The presence of the secondary slope produces a condition that is more critical than a simple 2D model of the same size. Two-dimensional models obviously fail to capture this feature. These observations and results indicate that the effects of the three-dimensionality are indeed important. In these cases, simple two-dimensional anlayses could underestimate the effects of the dynamic input. The results of this study can then be used to get an idea of the degree of unconservatism in the 2D results.

Reccomandation for next studies are, about SANICLAY model, find a way to build up a more efficient script, more stable and easy to apply to every case.

About the issue of the three dimensionality it should be intersting to investigate the earthquake response of slopes with different dynamic input, for example changing the direction of the input and using a realistic seismic input.

References

Kramer, S. (1996) "Geotechnical Earthquake Engineering"

Itasca Consulting Group, Inc. (2006). *FLAC3D-Fast Lagrangian analysis of continua in three dimension*, *Ver. 3.1*, *User's manual*, Minneapolis.

Dafalias, Y.F., Manzari, M. T., Papadimitriou A. G. "SANICLAY: simple anisotropic clay plasticity model" *J. Geotech. Geoenviron. Eng.*

Taiebat, M., Kaynia, A. M., Dafalias, Y. F. (2011) "Application of an Anisotropic Constitutive Model for Structured Clay to Seismic Slope Stability." *J. Geotech. Geoenviron. Eng.*

Azizian, A., Popescu, R., (2005) "Three-dimensional seismic analysis of submarine slopes" *Soil Dynamics and Earthquake Engineering (2006)*

Arellano, D., Stark, T.D., "Importance of three-dimensional slope stability analyses in practice." *Slope stability 2000, ASCE Geotech Special Pub 2000;*